UNIVERSITY OF CALIFORNIA
RIVERSIDE

The Nature of Low-ionization Broad Absorption Line Quasi-stellar Objects

A Dissertation submitted in partial satisfaction
of the requirements for the degree of

Doctor of Philosophy

in

Physics

by

Mariana Spasova Lazarova

September 2012

Dissertation Committee:

Professor Gabriela Canalizo, Chairperson
Professor Bahram Mobasher
Professor Allen Zych

The Dissertation of Mariana Spasova Lazarova is approved:

Committee Chairperson

University of California, Riverside

Acknowledgments

I am grateful to all the people and circumstances that have been part of my journey in life until now. I know that everybody I have ever met has influenced me in my decisions, one way or another, and the opportunities given to me together with the chain of those decisions have ultimately let me to the point of completing this dissertation work. I am a bit apprehensive in writing this acknowledgment, out of fear of forgetting someone, so I will only try to thank the people who have been indispensable to me.

Most of all, I would like to thank my advisor, Gaby, for her friendliness and unfailing smile which tricked me into thinking that I can do this. Her bright insights and unconditional support of me, with my ever more complicated circumstances, were crucial in my growth into as an astronomer.

I would like to thank Kyle for putting up with random mindless conversations and, thus, making the years in graduate school seem short and full with laugher.

I would like to thank my mom and dad for their tremendous efforts and sacrifices in making my education in the USA possible. But mostly, I would like to thank my mother, Roza, for her unconditional love and hard work in helping me raise my children.

I would like to thank my ex-husband, Fernando, who surely dragged me through hell and back, but without whose continual support and deep love for our children, my life would have been very different in an unforeseen direction.

Last, but not least, I would like to thank two people who made their grand appearance into this world while I was in graduate school, my son Alexander and my daughter Diana, for making their emotional sacrifices in letting me work long hours and for their purest of love. To me, only they give a meaning to it all.

To my children,

Alexander and Diana

ABSTRACT OF THE DISSERTATION

The Nature of Low-ionization Broad Absorption Line Quasi-stellar Objects

by

Mariana Spasova Lazarova

Doctor of Philosophy, Graduate Program in Physics
University of California, Riverside, September 2012
Professor Gabriela Canalizo, Chairperson

The tight correlations between properties of galaxy bulges and their central supermassive black holes have been reproduced successfully in simulations of galaxy collisions if feedback processes are invoked. Mergers of gas-rich galaxies of comparable size have been shown to trigger starbursts, fuel the central black holes, and transform disks into ellipticals. Feedback from the black hole accretion in the form of extreme outflows has need suggested as the mechanism by which the black hole stop its own growth and quenches the star formation in the galaxy by expelling the gas supply. Such winds have been detected in Broad Absorption Line (BAL) QSOs. However, observational evidence that BAL QSOs may be an evolutionary link between mergers and QSO is missing.

In this thesis, we provide the first detailed study of the spectral energy distributions and host galaxy morphologies of a statistically significant volume-limited sample of 22 optically-selected low-ionization Broad Absorption Line QSOs (LoBALs) at $0.5 < z < 0.6$. By comparing their mid-IR spectral properties and far-IR SEDs with those of a control sample of 35 non-LoBALs (non-LoBALs) matched in M_i, we investigate the differences be-

tween the two populations in terms of their infrared emission and star formation activity. We model the SEDs and decouple the AGN and starburst contributions to the far-infrared luminosity in LoBALs and in non-LoBALs. We estimate star formation rates (SFRs) corrected for the AGN contribution to the FIR flux and find that LoBALs have comparable levels of star formation activity to non-LoBALs when considering the entire samples. Overall, our results show that there is no strong evidence from the mid- and far-IR properties that LoBALs are drawn from a different parent population than non-LoBALs.

We conducted the first high-resolution morphological analysis of LoBALs using observations obtained with the Hubble Space Telescope Wide Field Camera 3 in two channels. Signs of recent or ongoing tidal interaction are seen in 73% of the host galaxies, including interacting companions, tidal tails, bridges, asymmetries, plumes, and boxy isophotes. The presence of a second nucleus within $\sim 1''$ (6.4 kpc) is revealed in seven of the systems. A detailed two-dimensional surface brightness analysis with GALFIT indicates that the majority (73%) have prominent early-type (bulge, n>4) morphology and only four systems have exponential disk profiles (n<2). Two of the disks and one bulge are better described as pseudobulges (n<2.2). The dominance of bulges and unambiguous signs of tidal interaction strongly suggests that the population LoBALs are QSOs that result from major mergers. Nevertheless, most of the merger-induced start formation is already quenched. This sample of LoBALs represents merger systems at various stages of the interaction process, hence, either the outflows which characterize these systems persist for as long as the interaction signs are observable in the galaxy, or very short-lived outflows are triggered and die out during various stages of the merger process.

Overall, our results are consistent with LoBALs representing the last stages of the blowout phase when QSO winds have already quenched the star formation.

Contents

List of Figures

List of Tables

Chapter 1

Introducing LoBALs

Supermassive black holes are found to be ubiquitously present at the centers of galaxies with bulges and several relationships between the mass of the black hole and properties of the spheroid strongly suggest co-evolution of the two (e.g., Kormendy & Richstone, 1995; Magorrian et al., 1998; Laor, 1998; Gebhardt et al., 2000; Ferrarese & Merritt, 2000; Kormendy & Gebhardt, 2001; McLure & Dunlop, 2002; Tremaine et al., 2002). The mechanisms via which the galaxy and black hole regulate each other's growth are still unknown. Various types of outflows, such as supernova winds and AGN-driven winds, have been invoked as the plausible feedback processes responsible for quenching the star formation in the host and clearing the gas from the nuclear region, and, thus, halting the accretion onto the black hole and limiting its mass (e.g., Di Matteo et al., 2005). However, observational evidence of the extent of their influence is still sparse and uncertain (e.g., Moe et al. 2009; Bautista et al. 2010; Dunn et al. 2010).

Observations of young, recently fueled QSOs are the key to testing this evolutionary model. Particular attention has been paid to studying the properties of ultraluminous infrared galaxies (ULIRGs; $L_{IR} > 10^{12} L_{\odot}$) since they are believed to be powered by both AGN and starbursts, although starbursts are generally believed to be responsible for the bulk of the power output (Sanders et al. 1988; for review see Sanders & Mirabel 1996). The connection between AGN and ULIRGs is suspected by the fact that they are some of the most luminous sources in the universe with comparable luminosities of $L_{bol} > 10^{12} L_{\odot}$. In addition, they are both associated with strong infrared emission from dust (e.g., Haas et al., 2003). The morphologies and dynamics of ULIRGs indicate that these galaxies are associated with galaxy mergers (Armus et al., 1987; Sanders et al., 1988; Murphy et al., 1996; Veilleux et al., 2002; Dasyra et al., 2006). Similarly, many QSO hosts at $z < 0.4$ show signs of interaction, even some of those that had previously been classified as ellipticals (Canalizo & Stockton, 2001; Canalizo et al., 2007; Bennert et al., 2008). If starbursts, ULIRGs, and AGN are connected in an evolutionary sequence which was initiated by a galaxy interaction, observations of the transition stages of this process are necessary to better understand this connection (see e.g., Hopkins et al., 2007, 2008b,a).

BAL QSOs are promising candidates for newly emerging optical QSOs. BAL QSOs are a subclass of QSOs characterized by broad absorption troughs of UV resonance lines, blueshifted relative to the QSO's rest frame, which are indicative of gas outflows with speeds of up to $0.2c$ (Foltz et al., 1983). BALs were rigorously defined by Weymann et al. (1991) to include only objects with broad absorption lines wider than 2000 km s^{-1}, blueshifted past the first 3000 km s^{-1}; however, some studies more recently have been more inclusive

of the wide range of absorption observed and have relaxed that criterion to lower limits on the absorption width of 1000 km s^{-1} (e.g., Trump et al., 2006). Hydrodynamic models show that AGNs are capable of launching such high velocity winds (Murray et al., 1995; Proga et al., 2000; Gallagher et al., 2012). Based on the material producing BAL troughs, there are at least three subclasses of BAL QSOs. The high-ionization BAL QSOs (HiBALs) are identified via the broad absorption from C IV λ1549, but they might have absorption from other high-ionization species such as Lyα, N V λ1240, and Si IV λ1394 (Hall et al., 2002). The low-ionization BAL QSOs (LoBALs), in addition to the lines present in HiBALs, feature absorption lines from Mg II $\lambda\lambda$ 2796,2803, Al III, and Al II. A very small fraction of LoBALs, called FeLoBALs, show absorption in the rest-frame UV from metastable, excited states of Fe II (Hazard et al., 1987).

It is not well understood why only 10%−30% of the optically selected QSOs have BALs (Tolea et al., 2002; Hewett & Foltz, 2003; Trump et al., 2006; Gibson et al., 2009), and only about one tenth of these are LoBALs (Reichard et al., 2003a). Due to the highly obscured nature and much redder continua of these objects, optical identification omits a large fraction of BALs. Therefore, although LoBALs are observed in only 1-3% of all optically-selected QSOs, they comprise a much higher fraction of the QSOs selected at longer wavelengths (Urrutia et al., 2009; Dai et al., 2010). Allen et al. (2011) estimate that the intrinsic fraction of BAL QSOs can be as high as ∼40% when the spectroscopic incompleteness and bias against selecting BAL QSOs in the SDSS are taken into account. Hence, BAL QSOs may only be rare in optically-selected samples.

Models attempting to explain their occurrence need to account for their obscured nature. Currently there are two competing interpretations of the BAL phenomena: orientation and evolution. On one hand, BAL and non-BAL QSOs are thought to derive from the same parent population because of the remarkable similarity in their SEDs (Weymann et al., 1991; Gallagher et al., 2007). Nonetheless, QSO continua appear to be increasingly reddened in a sequence going from non-BALs to HiBALs to LoBALs (Reichard et al., 2003b; Richards et al., 2003). This finding inspired efforts to explain the low occurrence of BAL QSOs within the framework of the AGN unification model Antonucci (1993), suggesting that, due to orientation effects, BALs are seen in classical QSOs only when viewed along a narrow range of lines of sight passing through the accretion disk wind. In this picture, high column density accretion disk winds of ionized gas are driven via resonance line absorption (Murray et al., 1995; Murray & Chiang, 1998; Elvis, 2000). This model explains the low occurrence of BALs as a natural consequence of the fact that BALs are observed only at a small range of viewing angles. Although BALs are predominantly radio quiet sources (Stocke et al., 1984, 1992), radio observations of the few radio-detected BALs provide a test to the orientation of the BAL wind with respect to the radio jet. Radio-detected BALs are observed at a wide range of inclinations (Becker et al., 2000; Gregg et al., 2000; Brotherton et al., 2006; Montenegro-Montes et al., 2008; DiPompeo et al., 2010) suggesting that the occurrence of BALs is not a simple orientation effect (e.g., DiPompeo et al., 2012). Currently it is not clear whether or not radio-loud (RL) and radio-quiet (RQ) QSOs arise from the same parent population, so it is certainly possible that RL and RQ BAL QSOs are different classes.

An alternative model proposes that BAL QSOs are young QSOs caught during a short-lived phase in their evolution when powerful QSO-driven winds are blowing away a dusty obscuring cocoon (e.g., Hazard et al., 1984; Voit et al., 1993; Hall et al., 2002, and references therein). This model appears to be particularly applicable to LoBALs since these objects are suspected to be young or recently refueled QSOs (Boroson & Green, 1992; Lipari et al., 1994) and might be exclusively associated with mergers (Canalizo & Stockton, 2001). Observations by Canalizo & Stockton (2002) of the only four known LoBALs at $z < 0.4$ at the time showed that: (1) they are ULIRGs; (2) they have a small range of far-IR colors, intermediate between those characteristic of ULIRGs and QSOs; (3) their host galaxies show signs of strong tidal interactions, resulting from major mergers; (4) spectra of their hosts show unambiguous interaction-induced star formation with post-starburst ages ≤ 100 Myr. Similarly, studies of FeLoBALs, both at low (Farrah et al., 2005) and high redshifts (Farrah et al., 2007, 2010), suggest that they are associated with extremely star-forming ULIRGs.

Most recent hydrodynamic simulations of major galaxy mergers by Debuhr et al. (2011) show that an AGN-driven BAL wind with an initial velocity ~ 10000 km s^{-1} would lead to a galaxy-scale outflow with velocity ~ 1000 km s^{-1}, capable of unbinding $10-40\%$ of the initial gas of the two merging galaxies. Such AGN feedback could possibly explain the observed high-velocity outflows in post-starburst galaxies (Tremonti et al., 2007) and ULIRGs (e.g., Chung et al., 2011; Rupke & Veilleux, 2011; Sturm et al., 2011). Further, if the paradigm suggesting that AGN feedback is responsible for regulating the growth of

galaxies is correct, LoBALs may be at a unique stage where strong outflows are present, yet, star formation is still in the process of being quenched.

In this dissertation, we present the first detailed study of the star-forming and interaction histories of a statistically-significant volume-limited sample of LoBAL QSOs at low redshift. The investigation is focused on testing the idea that LoBALs are a transition phase in quasar evolution by studying properties of the host galaxies, such as infrared luminosities and morphology. In Chapter 2, we show results from *Spitzer* IRS spectroscopy and MIPS photometry at 24, 70, and 160 μm. We model the infrared SEDs of LoBALs and measure their far-infrared luminosities and star formation rates to investigate their star-forming history in comparison to a well-matched sample of unobscured non-LoBAL type-1 QSOs. In Chapter 3, we study the detailed morphologies of LoBAL host galaxies via $HST/WFC3$ imaging, with particular attention to tell-tale signs of recent or past tidal interaction. The conclusion is given in Chapter 4.

Chapter 2

SEDs and mid-infrared spectral properties

ABSTRACT

We have obtained *Spitzer* IRS spectra and MIPS 24, 70, and 160 μm photometry for a volume-limited sample of 22 SDSS-selected Low-ionization Broad Absorption Line QSOs (LoBALs) at $0.5 < z < 0.6$. By comparing their mid-IR spectral properties and far-IR SEDs with those of a control sample of 35 non-LoBALs (non-LoBALs) matched in M_i, we investigate the differences between the two populations in terms of their infrared emission and star formation activity. Twenty five percent of the LoBALs show PAH features and 45% have weak 9.7μm silicate dust emission. We model the SEDs and decouple the AGN and starburst contributions to the far-infrared luminosity in LoBALs and in non-LoBALs. Their median total, starburst, and AGN infrared luminosities are comparable.

Twenty percent (but no more than 60%) of the LoBALs and 26% of the non-LoBALs are ultra-luminous infrared galaxies (ULIRGs; $L_{IR} > 10^{12} L_{\odot}$). We estimate star formation rates (SFRs) corrected for the AGN contribution to the FIR flux and find that LoBALs have comparable levels of star formation activity to non-LoBALs when considering the entire samples. However, the SFRs of the IR-luminous LoBALs are 80% higher than those of their counterparts in the control sample. The median contribution of star formation to the total far-infrared flux in LoBALs and in non-LoBALs is estimated to be 40-50%, in agreement with previous results for PG QSOs. Overall, our results show that there is no strong evidence from the mid- and far-IR properties that LoBALs are drawn from a different parent population than non-LoBALs.

2.1 Introduction

Previous studies of large samples of BAL QSOs addressing their SEDs (Gallagher et al., 2007) and submillimeter properties (Willott et al., 2003) find that BAL and non-BAL QSOs are indistinguishable, consistent with the model that all QSOs contain BAL winds, and their detection depends on viewing angle. However, those samples mainly comprise HiBALs and refrain from drawing conclusions about LoBALs. Even if the detection of BAL troughs in QSO spectra depends on viewings angle, compelling evidence suggests that LoBALs are linked to IR-luminous galaxies, with dominant young stellar populations and disturbed morphologies. To test this possibility, we have undertaken the first multi-wavelength investigation of a volume-limited sample of LoBALs. We address the nature of low-redshift LoBALs and their relationship to the broader QSO population. In particular,

we test the idea that LoBALs might be a short, evolutionary stage when the AGN has been recently fueled by a merger and the ensuing winds are in the process of quenching the star formation.

In this chapter, we present *Spitzer* IRS spectroscopy and MIPS photometry at 24, 70, and 160 μm of a volume-limited, statistically-significant sample of low-redshift, optically-selected LoBALs. To study their star-forming histories, we model the infrared SEDs of LoBALs and measure their far-infrared luminosities and star formation rates. In the next chapter, we study the detailed morphologies of LoBAL host galaxies via *HST* imaging.

Our sample of LoBALs and a control sample are described in § 2. Details of the observations are explained in § 3. We present the analysis and results in § 4. Discussion and summary of results are given in § 5. The conclusion is presented in § 6. We assume a flat universe cosmology with $H_0 = 71$ km s^{-1} Mpc^{-1}, $\Omega_M = 0.27$, and $\Omega_\Lambda = 0.73$. All luminosities in units of the bolometric solar luminosity were calculated using $L_\odot = 3.839 \times 10^{33}$ erg s^{-1}.

2.2 Sample selection

2.2.1 LoBALs

We selected a volume-limited sample of 22 LoBALs from the Sloan Digital Sky Survey (SDSS: York et al., 2000) Third Data Release (DR3; Abazajian et al., 2005). One of the spectral lines which classifies QSOs as LoBALs is the blue-shifted broad absorption

of Mg II λ2800. Samples of optically-identified LoBALs are only available for $z > 0.48$, when this low-ionization broad absorption line is redshifted from rest-frame UV into the spectral range of the SDSS. While now there are available SDSS catalogues with LoBALs at $z > 0.48$ (e.g., Gibson et al., 2009), at the time the sample for this project was selected the most up-to-date catalog of BAL quasars was the one by Trump et al. (2006), which identified LoBALs for $z > 0.5$.

In addition to characterizing the FIR emission of LoBALs, we wanted to study their mid-infrared spectral properties, in particular, the PAH emission lines at rest-frame 6.2, 7.7, 8.6, 11.3, and 12.8 μm and the silicate emission at rest-frame 9.7 μm. Choosing objects at redshifts less than 0.6 ensures that these spectral lines are observable within the wavelength range $7-21$ μm, allowing us to use only two of the four channels of the *Spitzer* infrared spectrograph (i.e., SL1 + LL2; see Section 3.2 for details). An upper limit of $z < 0.6$ also makes it feasible to resolve the host galaxy morphologies on *HST* images despite the bright nuclear emission. An attempt to study the morphologies of LoBALs at $0.9 < z < 2.0$ showed that the host galaxies could not be resolved at those redshifts (i.e., Fan; *HST* PID 10237), which strongly motivated us to choose a lower redshift upper limit.

With these considerations in mind, our sample was selected to include all LoBALs within the redshift range $0.5 < z < 0.6$ from the Trump et al. (2006) catalog of BAL quasars, drawn from Data Release 3 of the Sloan Digital Sky Survey quasar catalog by Schneider et al. (2005). In the Trump et al. (2006) catalog, QSOs with regions of flux at least 10% below the continuum, spanning over a velocity range of at least 1000 km s^{-1} blue-ward of Mg II λ2800, were identified as LoBALs. They found 457 LoBALs in the redshift range

$0.5 < z < 2.15$. Of those, only 22 fall within $0.5 < z < 0.6$, when we exclude one object which is classified as a narrow-line LoBAL and one identified as an uncertain FeLoBAL. The volume-limited sample of 22 low-redshift LoBALs is listed in Table 2.1. Note that some of the objects in our sample are not identified as LoBALs in the catalog by Gibson et al. (2009) since the Gibson et al. introduce a new balnicity index, which is different from the absorption index of Trump et al. (2006). The SDSS spectra of the objects in our sample, showing the Mg II absorption trough, are included in the Appendix.

2.2.2 Control sample of non-LoBAL type-1 QSOs

In order to investigate the relationship between LoBALs and classical QSOs, we compiled a sample of type-1 QSOs with sufficient available archival data to be analyzed in the same way as the LoBAL sample. We selected objects whose spectra did not show Mg II BAL absorption. Since we do not have UV spectra to determine whether any of these objects are HiBALs, we shall refer to them as "non-LoBALs." We drew the control sample from the compilation of quasar SEDs by Richards et al. (2006), who published all available SDSS, *Spitzer* MIPS, and IRAC photometry, as well as x-ray and radio data, of the type-1 quasars in the SDSS-DR3 quasar catalog by Schneider et al. (2005). It is important to match the LoBALs to type-1 QSOs of comparable luminosity. Limiting the control sample to the same redshift range as the LoBALs, i.e., $0.5 < z < 0.6$, selected only 11 non-LoBALs whose absolute M_i magnitudes matched only the lower luminosity LoBALs. To avoid the problem of having an under-luminous control sample, we matched the control sample to the reddening-corrected optical luminosity of the LoBALs, not restricting the

redshift. Moreover, only few LoBALs have been found to have radio emission (e.g., Becker et al., 1997, 2000, 2001; Brotherton et al., 1998; Menou et al., 2001), which limits our selection to the radio-quiet sub-population.

In summary, we selected all radio-quiet non-LoBALs from Richards et al. (2006), which matched the absolute M_i magnitude range of our LoBAL sample, $-22.4 > M_i > -25.6$ (see Table 2.1). A total of 35 objects within $0.45 < z < 0.83$ satisfied these criteria: 16 from the Lockman hole, six from the ELAIS-N1, six from the ELAIS-N2 fields in the *Spitzer* Wide-Area Infrared Extragalactic Survey (SWIRE: Lonsdale et al., 2003), and seven from the *Spitzer* observations of the Extragalactic First Look Survey area (xFLS: Frayer et al., 2006). Tables 2.1, 2.2 and 2.3 list relevant optical and infrared photometry of the comparison sample of non-LoBALs.

2.3 Observations and Data Reduction

2.3.1 LoBALs

Spitzer IRS

Mid-infrared spectra of 20 of the 22 LoBALs were obtained with the *Spitzer* Infrared Spectrograph (IRS; Houck et al., 2004) as part of our Cycle 5 GO program (Program ID 50792). The IRS observations of the last two scheduled objects, SDSS J023102−083141 and SDSS J023153−093333, could not be completed due to the depletion of the cryogen and the early commencement of the *Warm Spitzer mission*. All 20 of the objects were observed in staring mode with the Short Low first-order module (SL1), which covers 7.4−14.5 μm, and

with the Long Low second-order module (LL2), which covers 14.0−21.3 μm. Observations in SL1 and LL2, respectively, consisted of a 6 or 14 s ramp for 2 cycles with two nod positions and a 120 or 30 s ramp for one to three cycles with two nod positions. The exact ramp durations and number of cycles for each object are listed in Table 2.4. The slit width was $3\farcs7$ and $10\farcs5$ (corresponding to 24 kpc and 67 kpc at z=0.55), for the SL1 and LL2 orders, respectively.

We used the pipeline coadded, non-subtracted post-BCD frames. The bad pixels in the images were removed with the interactive IDL procedure IRSCLEAN1.9 (version 1.7). Sky subtraction was achieved by subtracting the two-dimensional image at one nod position from the other nod position of the corresponding order. One-dimensional spectra were extracted with the Java-based *Spitzer* IRS Custom Extraction software (SPICE; version 2.3 Final) using the default parameters of the optimal extraction method for point sources. We used IDL to combine the two nod position in each order and then to combine the spectra from the two orders into a continuous spectrum spanning the wavelength range of 7.4−21.3 μm: first, the spectrum at each nod position was median-smoothed and interpolated on a uniform wavelength grid; then, the two nod positions for each order were averaged; and finally, the two orders (e.g., SL1 and LL2) were concatenated by averaging the spectra in the overlapping region. The combined mid-IR spectra of the 20 LoBALs observed with the IRS are shown in Fig. 2.1.

Spitzer MIPS

Far infrared photometry at 24, 70, and 160 μm was obtained with the Multiband Imaging Photometer for *Spitzer* (MIPS; Rieke et al., 2004) as part of our GO program (ID 50792). Although the entire sample of 22 LoBALs was scheduled for MIPS observations, only 17 targets could be observed prior to the cryogen depletion and the commencement of the *Warm Spitzer mission*. The 24 and 70 μm observations were obtained using the small-field default resolution photometry mode, while for the 160 μm observations we used the small-field enhanced resolution mode. Typical observing modes were one 3 s cycle at 24 μm (48 s integration time), one 10 s cycle at 70 μm (126 s integration time), and four 10 s cycles at 160 μm (179 s integration time). The standard tasks of cosmic-ray removal, image-coaddition, and dark subtraction were carried out by the automated MIPS data reduction pipeline at the *Spitzer* Science Center. Our data reduction started from the pipeline BCD files, which were assessed to be of sufficient quality. For the 24 μm observations, final mosaic images were constructed with the MOsaicker and Point source EXtractor software (MOPEX: Makovoz & Marleau, 2005) after flat-fielding and background correction. At 70 and 160 μm, we used the pipeline-filtered BCDs to construct mosaics for most of the sources. Aperture photometry at 24, 70, and 160 μm was performed with IDL, using an aperture radius of $13''$, $35''$, and $48''$, respectively. The MIPS fluxes are listed in Table 2.2. All of the 17 sources observed with MIPS were detected at 24 microns, but only four were detected at 70 μm and only three at 160 μm. Small field photometry with MIPS 160 μm, in particular, has the problem that the filtering step of the data reduction leads to a loss of flux (Sajina 2012, in preparation). The manual states this loss is 10% (see also Sajina

et al., 2008), but it can be as high as 30−50%. Three sigma upper limits at 70 μm and 160 μm were estimated from the standard deviation images associated with the mosaics. All fluxes have been corrected for the finite aperture size by multiplying by a correction factor of 1.16 at 24 μm, 1.22 at 70 μm, and 1.601 at 160 μm (aperture corrections from the MIPS Data handbook). The systematic uncertainties are 4% at 24 μm, 5% at 70 μm, and 12% at 160 μm. The uncertainties listed in Table 2.2 for the LoBAL sample are from the aperture photometry calculation.

Near-Infrared and Optical photometry: SDSS and 2MASS

All of the 22 LoBALs in the sample have available SDSS Data Release Seven (DR7) and Two Micron All Sky Survey (2MASS; Skrutskie et al., 2006) photometry published in the quasar catalog of Schneider et al. (2010). Table 2.1 lists the best SDSS PSF *ugriz* AB magnitudes (ugriz; Fukugita et al., 1996), corrected for Galactic extinction using the map of Schlegel et al. (1998). We impose more conservative limits on the near-infrared data than Schneider et al. (2010) by considered reliable only 2MASS magnitudes with Photometry Quality Flag (ph_qual) A, B, or C and Read Flag (rd_flg) 1, 2 or 3, which ensure measurements with signal-to-noise greater than five and measurement uncertainty less than 0.2. The meaning of the flags can be found in Cutri et al. (2003). Table 2.2 lists the 2MASS J (1.25 μm), H (1.65 μm), and K_s (2.16 μm) Vega magnitudes of the LoBALs.

2.3.2 Control sample

SDSS, 2MASS, *Spitzer* IRAC and MIPS photometry

We use the SDSS DR7 u, g, r, i, z and 2MASS J, H, K_s photometry published by Schneider et al. (2010) together with the IRAC 3.6, 4.5, 5.8, 8.0 μm, and the MIPS 24 μm data published by Richards et al. (2006). All the *Spitzer* data are taken from the xFLS and SWIRE ELAIS-N1, ELAIS-N2, and Lockman Hole areas. To obtain 70 and 160 μm fluxes, we performed aperture photometry with IDL on the processed mosaics provided online by Frayer et al. (2006) for the xFLS field[1] and by Lonsdale et al. (2003) for the three SWIRE fields[2]. The 3σ upper limits at 70 and 160 μm were estimated from the uncertainty images. Table 2.3 lists the fields from which the MIPS photometry for individual objects was extracted.

2.4 Analysis and Results

2.4.1 MIR spectral features of LoBALs

The combined SL1 and LL2 orders covers an observed wavelength range $\lambda_{obs} = 7.4 - 21.3$ μm, which at redshift 0.5−0.6 translates to rest-frame $\lambda_{rest} \approx 5 - 13$ μm, after removing the noisy region on the red side. LoBALs exhibit a wide range of mid-IR spectral properties (Fig. 2.1). About one third (40%) of the spectra are featureless low-signal-to-noise continua, nearly half (45%) of the objects show silicate emission near 10 μm and a

[1] xFLS data from $< http://data.spitzer.caltech.edu/popular/fls/extragalactic\_FLS/enhanced\_MIPS\_Ge/images/ >$

[2] SWIRE data from $< http://swire.ipac.caltech.edu/swire/astronomers/data\_access.html >$

quarter (25%) have at least one of the PAH emission lines, with concurrent PAH and silicate emission present in one tenth (10%) of the sample.

PAH emission features

The emission from polycyclic aromatic hydrocarbon molecules (PAHs), producing prominent lines in the mid-IR peaking at 3.3, 6.2, 7.7, 8.6, 11.3, and 12.8 μm (Gillett et al., 1973; Leger & Puget, 1984), is powered by moderate UV radiation. PAHs are observed in photo-dissociation regions (PDRs) where young bright stars are contiguous with dense molecular clouds, conditions found in star-forming regions and reflection nebulae (e.g., Duley et al., 1991; Verstraete et al., 1996). The correlation between PAH emission and star formation rates in star-forming galaxies (e.g., Genzel et al., 1998; Roussel et al., 2000; Dale & Helou, 2002) established PAHs as tracers of star formation (but see Haas et al. (2002) for a counter argument). On one hand, there is evidence that the PAH molecules are destroyed by the extreme UV and X-rays radiation (Puget & Leger, 1989; Voit, 1992; Allain et al., 1996; Genzel et al., 1998; Smith et al., 2007; O'Dowd et al., 2009; Hunt et al., 2010), so PAH-derived star formation may underestimate the actual activity. In AGN, PAH features are absent (e.g., Roche et al., 1991; E. Le Floc'h et al., 2001), weak (e.g., Laurent et al., 2000), or have low equivalent widths (e.g., Clavel et al., 2000), implying destruction or inability of the nuclear radiation to excite the aromatic feature. On the other hand, the AGN may enhance the PAH emission since the nuclear continuum contributes ample flux in the UV, which may modify the grain distribution and directly excite the PAH emission

(e.g., Smith et al., 2007). Thus, adopting PAH emission as a star formation tracer in AGN hosts should be done with caution.

Studies of the spatial distribution of the PAH emission in nearby AGN find that the aromatic emission arises in an extended circum-nuclear region (e.g., Cutri et al., 1984, $<$ 1 kpc) or in the galactic disk (Laurent et al., 2000), which together with the low equivalent widths of PAH features (e.g., Roche et al., 1991; Clavel et al., 2000) implies that PAHs in AGN are predominantly excited by star-formation (e.g., Shi et al., 2007, and references therein). This is also supported by Schweitzer et al. (2006) who find the same ratio between the 7.7 μm PAH and the 60 μm luminosity in a sample of 27 PG QSOs and in starburst-dominated ULIRGs, suggesting that the starburst is producing all of the QSO FIR emission.

In our sample of 20 LoBALs with available IRS spectra, we detect weak PAH features only in five of the objects. The PAH emission is strongest for the three objects shown at the top of the right column in Fig. 2.1. The entire complex of PAH lines is seen only in SDSS J170010+395545, while PAHs are concurrent with silicate emission only in two sources. We confirm the previously observed low incidence of PAH emission in AGN, in general, to be true also for LoBALs, in particular.

The average MIR spectrum of all LoBALs (Fig. 2.2), obtained by averaging the signal-to-noise-weighted individual spectra after normalization to the 6 μm continuum flux, shows very weak PAH emission at 6.2, 11.3 and 12.8 μm. Plotted in the same figure are the average spectra of LoBALs grouped according to shared MIR spectral characteristics, i.e., objects with PAH emission, those with silicate emission, and those showing neither silicate nor PAHs. PAH emission at 6.2 μm becomes more prominent in the average spectrum of

the LoBALs with PAHs. In the average spectrum of LoBALs which did not otherwise show individual PAH features, we detect the 12.8 μm line. We note that the feature at 12.8 μm might be a blend of the PAH at 12.7 μm and the low-excitation fine-structure emission line of [Ne II] 12.8 μm, which is dominant in H II regions and used as SF tracer. In QSOs, however, [Ne II] could also arise in the narrow line region of the AGN and Veilleux et al. (2009) show that the starburst contributes at most 50% to its flux. In addition, we subdivided the 15 LoBALs that had both IRS spectra and FIR constraints into those with AGN infrared luminosity greater than and less than their starburst luminosity (see section 2.4.3 for details on the measurement of these quantities). The two averages are shown in Fig. 2.2, denoted $L_{IR}^{SB} < L_{IR}^{AGN}$ and $L_{IR}^{SB} > L_{IR}^{AGN}$, respectively. We note that in the cases of FIR upper limits for objects with $L_{IR}^{SB} > L_{IR}^{AGN}$, it is not certain whether L_{IR}^{SB} is less than or greater than L_{IR}^{AGN}.

The PAH lines are stronger in the composite of objects with $L_{IR}^{SB} > L_{IR}^{AGN}$ than in the "PAH average," suggesting that the FIR emission, indeed, arises from star formation rather than from a very extended torus, for example. The average of all LoBALs is remarkably similar to the subgroups of those without PAHs and the one with silicate emission. For comparison, we also plot an average spectrum of the five type-1 QSOs in the Hiner et al. (2009) sample which fall within the redshift range $0.5 < z < 0.63$. The composite of all LoBALs is similar to that of their type-1 QSOs.

Silicate emission feature at 10 μm

Silicate compounds comprise the majority of the interstellar dust and manifest themselves in the MIR via two main features centered around 10 μm and 18 μm. The wavelength coverage of our IRS spectra allows us to investigate the silicates peaking at 9.7 μm which arise from the stretching of the Si−O bond (Knacke & Thomson, 1973). Due to low dust temperatures of order $T \sim 100$ K, this feature is also seen to peak at longer wavelengths, up to $\lambda_{Si} \sim 11$ μm (e.g., Zakamska et al., 2008). The exact peak of the feature is speculated to be sensitive to grain size and composition, with larger dust grains and crystalline dust (as opposed to amorphous dust) causing the feature to peak at longer wavelengths (e.g., Bouwman et al., 2001). However, Nikutta et al. (2009) show that the flat-topped silicate emission peaks observed in several type-1 sources can be explained by simple radiative transfer effects in standard Galactic dust in a clumpy torus model.

Most studies of silicate detections in AGN show that there is a notable dependence of the silicate strength on the optical classification of the AGN. In the framework of the unification model, silicate emission arising from the dust torus surrounding the accretion disk was predicted by the models of Pier & Krolik (1993). If we attribute the appearance of the silicate features in AGN to viewing angle, then type-1 AGN are expected to show silicate in emission and type-2 objects in absorption. In fact, most observations of AGN in which the feature is detected support this interpretation. Type 2 quasars (e.g., Zakamska et al., 2008; Lacy et al., 2007; Hiner et al., 2009) and Seyfert 2 galaxies (Hao et al., 2007) are almost exclusively characterized by silicate absorption, while both weak silicate emission and absorption are found in type-1 QSOs (e.g., Siebenmorgen et al., 2005; Hao et al., 2005b;

Schweitzer et al., 2008; Hiner et al., 2009; Landt et al., 2010) and Seyfert 1 galaxies (Hao et al., 2007).

However, silicate emission or absorption is not ubiquitously present in AGN. The occasional detection of silicate emission in type-2 AGN (e.g., Sturm et al., 2005; Hao et al., 2005b; Teplitz et al., 2006; Lacy et al., 2007; Hiner et al., 2009) and silicate absorption in type-1 objects (e.g., Weedman et al., 2005; Hao et al., 2007), as well as the absence of the silicate feature in many AGN, challenges the universality of the orientation model and suggests a more complicated scenario. For instance, with the exception of two objects, one mini-LoBAL and one red QSO, all of the type-1 and type-2 QSOs in the Hao et al. (2007) sample exclusively show weak silicatein emission which argues against orientation-dependent silicate emission in QSOs, at least. Models of clumpy torus geometries (Nenkova et al., 2002, 2008a,b) and/or larger dust grain sizes (e.g., Laor & Draine, 1993; Maiolino et al., 2001) offer a solution to these discrepancies, but can only reproduce weak silicate features. Nikutta et al. (2009), for instance, show that clumpy dust geometry of the obscuring region can explain both why the 10 μm feature is not seen in deep absorption in any AGN and why it has been detected in emission in type-2 sources.

In order to compare our LoBALs to other studies, we calculate the silicate strength at 9.7 μm, $S_{9.7}$, as:

$$S_{9.7} = \ln \frac{f_{peak}(9.7\mu m)}{f_{cont}(9.7\mu m)},$$

where $f_{peak}(9.7\mu m)$ is the observed flux density at the peak of the silicate feature and $f_{cont}(9.7\mu m)$ is the continuum flux density interpolated below the peak of the emission line. The common challenge of determining the underlying continuum is further exacerbated

by the limited wavelength range of our IRS spectra (i.e., rest-frame 5.0−14.0 μm). As is apparent in Fig. 2.1, some of the silicate features have a truncated red wing and are often redshifted. Fortunately, the MIPS photometry allows us to extend the range of the IRS spectra by modeling the SEDs, which includes the silicate emission amplitude as a free parameter in the fit (see Section 2.4.2). Using the overall SED model, we determine the continuum by following the fitting recipes of Spoon et al. (2007) for continuum-dominated sources and interpolate the local mid-IR continuum over the range 5.0−31.5 μm by fitting a cubic spline to the 5.0−7.5, 14.0−14.2, and 26.1−31.5 μm continuum regions.

In our sample of LoBALs, silicate is present exclusively in emission and is detected in nine of the 20 objects, ranging from $S_{9.7} = 0.34-0.81$. Hence, LoBALs exhibit the weak silicate emission typical of other type-1 QSOs (e.g., Siebenmorgen et al., 2005; Hao et al., 2005b; Haas et al., 2005; Cleary et al., 2007; Hiner et al., 2009). However, we note that the detection/non-detection of silicate dust emission might be a function of the signal-to noise ratio of the data (see Section 2.4.5). The strength of the feature is individually noted in the bottom right corner of each spectrum in Fig. 2.1. The interpolated continuum is over-plotted with a dashed green line. Although apparently present, the strength of the feature could not be estimated in two objects, SDSS J112822+482308 and SDSS J114043+532439, due to lack of MIPS photometry at long wavelengths and, consequently, an SED model which allows better determination of the continuum. We note that SDSS J085215+492040 shows possible broad, weak absorption, but the IRS spectrum for that object has very low signal-to-noise ratio and our inability to measure the feature precludes us from further speculation. Silicate absorption features is never observed to peak at wavelengths longer

than 9.8 μm (e.g., Nikutta et al., 2009), while the peak of this apparent dip is located at $\sim$11 μm.

2.4.2 SED modeling

In general, the infrared emission in galaxies hosting an AGN is a combination of (1) starburst emission from dust heated by the UV flux of O and B stars in active star-forming regions (Devereux & Young, 1990; Devereux & Hameed, 1997), (2) the AGN emission from the dusty torus reprocessing the accretion disk continuum and re-radiating it in the infrared (Pier & Krolik, 1993), (3) diffuse, ambient cold dust (cirrus) emission illuminated by the interstellar radiation field (e.g., Rowan-Robinson & Crawford, 1989), and (4) infrared emission from evolved stellar populations (Knapp et al., 1992; Mazzei & de Zotti, 1994).

We fit the optical-through-FIR SEDs of the LoBALs and the control sample of non-LoBALs with a multi-component empirical model, which allows us to disentangle the two major sources that power the FIR emission, i.e., starburst and AGN. In our phenomenological SED modeling approach, we assume that cirrus and evolved stellar populations have negligible contribution to the FIR power budget, and account only for the starburst and AGN contributions.

The available optical photometry of our LoBAL sample is listed in Table 2.1, the MIPS photometry in Table 2.2, and the IRS spectroscopy is plotted in Fig. 2.1. The photometry of the control sample is given in Tables 2.1 , 2.2, and 2.3. The fitting code is

described in detail by Sajina et al. (2006) and Hiner et al. (2009). Here we briefly outline the modeling procedure. The SEDs of LoBALs are fit by four components:

(1) a QSO component, constructed from the line-free continuum of the Richards et al. (2006) SED composite and the emission lines from the SDSS quasar composite of Vanden Berk et al. (2001) (this modification was necessary to reduce the host galaxy contribution at long wavelengths present in the Vanden Berk et al. (2001) composite);

(2) a hot mid-IR component, modeled as a power law with an exponential cutoff at short and long wavelengths, with a turndown at ~ 20 μm;

(3) a warm FIR component, accounting for the small grain dust emission spanning a wide range of temperatures is modeled as a power law with cutoffs at high and low frequencies;

(4) and a cold FIR component, modeled as a modified black body at a fixed temperature $T_{dust} \sim 45$ K. Constraining the dust temperature to 45 K is a conservative assumption for a typical ULIRG-level starburst in nuclear regions, which are probably the closest local analogues to starbursts in powerful quasars.

(5) The SEDs of the control sample require an additional near-infrared (NIR) component accounting for the emission from very hot dust, which was modeled as a modified black body at a temperature of T=1000 K. This very hot dust component, which is thought to be emission from the inner wall of the dust torus, is not necessary for fitting the SEDs of the LoBALs, with the possible exception of SDSS J105102+525049 and SDSS J170010+395554. Since we do not have NIR data for the majority of the LoBALs of reliable

quality (see section §2.3.1), most of their SEDs are not well constrained in that region and we cannot say for certain that the 3 μm bump is not present in LoBALs.

The model also includes the Small Magellanic Cloud (SMC) extinction law (Prevot et al., 1984; Bouchet et al., 1985) and a composite PAH template or 9.7 μm silicate emission, if applicable.

The FIR emission from cold and warm dust is attributed to star formation, while the mid-IR hot dust is assumed to be heated by the AGN. For the objects not detected in the FIR, 3σ fluxes were used to impose upper limits to the SEDs.

In Fig. 2.3 we show the SEDs of the 15 LoBALs for which both IRS spectra and MIPS photometry could be obtained. The SEDs of the control sample are plotted in Fig. 2.4. Overlaid are the best-fit SED model and the phenomenological break-up of the different components. Although we have observed 20 of the 22 LoBALs with the *Spitzer* IRS (see Fig. 2.1), five of those could not be observed with MIPS due to the early cryogen depletion.

2.4.3 Measured quantities

Our phenomenological SED modeling is used to break down the AGN and starburst contributions to the FIR emission. In order to quantify the infrared luminosities and the level of star formation activity in LoBALs and compare it to that in non-LoBALs, we estimate the following quantities, which we list in Table 2.5 and in Table 2.6 for the samples of LoBALs and non-LoBALs, respectively. In these tables, columns (1) and (2) list the object number in the sample and its name.

Column(3) gives the total infrared luminosity from 8 to 1000 μm, $L^{total}_{IR,8-1000\mu m}$, which is integrated from the best-fit SED model and includes the contribution of the starburst and the AGN to the infrared flux.

Column (4) lists the FIR luminosity contributed by the starburst, L^{SB}_{IR}. It is estimated by summing the warm and cold components of the model. In our SED model, those two components account for the emission from warm, small grain dust and cold dust at $T_{dust} \sim 45$ K, respectively. We tested the robustness of the choice of a 45 K dust by allowing T_{dust} to vary as a free parameter in the fit, and found that it introduces a variation in the estimate of L^{SB}_{IR} of less than 5%. Attributing the warm and cold FIR emission to star formation is empirically justified by Lacy et al. (2007) who find, for a sample for six type-2 AGN, that the sum of these components scales with PAH luminosity for a wide range of FIR luminosities. Additional evidence for the star formation origin of the FIR emission comes from Netzer et al. (2007) who find that to be the case for PG QSOs.

Column (5) lists the contribution of the AGN (hot dust + continuum) to the FIR luminosity, $L^{AGN}_{IR,8-1000\mu m}$. It was estimated by integrating the reddened hot dust component and the QSO continuum from 8 to 1000 μm.

Column (6) shows the relative percentage contribution of the starburst infrared luminosity to the total IR luminosity from 8 to 1000 μm, $\frac{L^{SB}_{IR}}{L^{total}_{IR,8-1000\mu m}} \times 100\%$, obtained as the ratio of the integrated QSO composite and hot dust from 8 to 1000 μm to the total integrated flux from 8 to 1000 μm.

In Column (7) we list the total infrared luminosity from 3$-$1000 μm, L^{MIPS}_{TIR}. While we note that this quantity is calibrated for galaxies, we estimate it solely for comparison with

other studies. It is calculated from its empirically calibrated relationship to the broad-band MIPS fluxes at 24, 70, and 160 μm derived by Dale & Helou (2002, eq. 4):

$$L_{TIR}^{MIPS} = \zeta_1 \nu L_\nu(24\mu m) + \zeta_2 \nu L_\nu(70\mu m) + \zeta_3 \nu L_\nu(160\mu m)$$

where $[\zeta_1, \zeta_2, \zeta_3]$ are redshift dependent coefficients (e.g., [3.91499, 0.48179, 1.0049] for $z = 0.55$). The authors state that this relationship reproduces the model bolometric infrared luminosities from 3 to 1000 μm to better than 1% for galaxies at z = 0, less than 4% for all other redshifts $z < 4$, and 7% for colder galaxies. The data used to constrain the Dale & Helou SED models ranges in L_{TIR} from less than 10^8 $L_\odot$ to 10^{12} $L_\odot$, hence, this method should be successful in estimating L_{TIR} for our sample of ULIRGs and LIRGs. Five of the LoBALs in our sample were not observed with MIPS. For three of those we used Scanpi 2[3] to extract IRAS photometry at 25, 60, and 100 μm from which we estimate their total IR luminosity, following Dale & Helou (2002, eq. 5). The upper limits of L_{TIR} are calculated using the detections and/or the 3σ flux values for the bands in which the source was not detected. We note that the IRAS fluxes may not be reliable due to the large beam size and possible contamination by neighboring infrared sources. For instance, we measure the IRAS flux at 25 μm of SDSS J161425+375210 with Scanpi 2 to be 130 mJy, while its MIPS flux at 24 μm is 20 mJy.

Column (8) gives the SFRs calculated from the starburst infrared luminosities listed in columns (4). The SFRs are estimated using the Kennicutt (1998) relationship:

$$SFR(M_\odot yr^{-1}) = 4.5 \times 10^{-44} L_{IR}$$

[3]Scanpi 2 is the scan processing and integration tool for extraction of IRAS photometry, developed at IPAC/Infrared Science Archive, which is operated by the Jet Propulsion Laboratory, California Institute of Technology, under contract with the National Aeronautics and Space Administration.

where L_{IR} is total infrared luminosity in erg/s, within the range 8−1000 μm.

Note that the Kennicutt (1998) SFR relationship uses a slightly different definition of L_{TIR} from the one derived with the Dale & Helou (2002) formulae, 8−1000 μm as opposed to 3−1000 μm. The starburst components of the SEDs do not extend blueward of 7 μm in any object, so this does not affect our SFR_{IR}^{SB}.

For the five objects with IRS spectra that do not have MIPS photometry, we fit the SDSS photometry and the IRS data with an AGN composite and mid-IR hot dust component only, and, thus, estimate only the AGN contribution to the FIR. Without FIR data, it is impossible to estimate the starburst contribution to the FIR flux in those cases. However, modeling allows us to estimate lower limits to $L_{IR,8-1000\mu m}^{total}$ from the AGN flux from 8−1000 μm. For all other quantities, upper limits indicate that 3σ MIPS fluxes were used to constrain the SED model in the FIR.

2.4.4 Infrared luminosities of LoBALs

Total IR luminosities from MIPS photometry

First we address the total infrared luminosities of LoBALs to see if their apparent association with ULIRGs found at $z < 0.4$ (Canalizo & Stockton, 2002) is typical for all LoBALs. We use the definition of a ULIRG by Sanders et al. (1988), i.e., $L_{IR} > 10^{12} L_{\odot}$.

For fair comparison with other studies which address the total infrared luminosities based on photometry measurements alone, we use the estimates of L_{IR} from MIPS, L_{TIR}^{MIPS}, calculated with the Dale & Helou (2002) relation (Column (7) in Table 2.5). Considering only the detections, we find that one (5%) LoBAL is a LIRG ($L_{TIR}^{MIPS} = 10^{11-12} L_{\odot}$) and that

7/20 (35%) have $L_{TIR}^{MIPS} > 10^{12} L_{\odot}$. Three of those seven ULIRGs are potential HyLIRGs ($L_{IR} > 10^{13} L_{\odot}$) based on $IRAS$ photometry, which is unreliable due to the large beam size and possible inclusion of neighboring sources. However, we note that more than half of the objects were not detected.

Only five LoBALs in the sample have detections in the FIR MIPS bands at 70 and 160 μm. Of those five, only four are ULIRGs. Regardless of the prevalence of upper limits, our results unambiguously show that low-redshift LoBALs are not exclusively associated with ULIRGs, with at least 40% of them being found in LIRGs.

Similar estimates of L_{IR} are derived by integrating the flux from 8 to 1000 μm of the best-fit SED models (Fig. 2.3). The values of $L_{IR,8-1000\mu m}^{total}$ are listed in Table 2.5, column (3). We find that 4/20 (20%) of the LoBALs are ULIRGs and 16/20 (80%) are LIRGs. For comparison, we estimate the total infrared luminosities, $L_{IR,8-1000\mu m}^{total}$, of the control sample of 35 non-LoBALs in the same way (see Table 2.6). Of the 17 control QSOs with FIR detections, nine (at least 26% of the total sample) are ULRIGs. We find that the fraction of LoBALs residing in ULIRGs is similar to that of non-LoBALs. The median total infrared luminosities, $L_{IR,8-1000\mu m}^{total}$, of the FIR-detected subsamples are $\sim$ 12.12 for the LoBALs and 11.92 for the non-LoBALs.

In order to compare the LoBAL and non-LoBAL samples in the presence of so many upper limits, we use the survival analysis statistical tests (Feigelson & Nelson, 1985). We test the hypothesis that LoBALs and non-LoBALs have the same distributions of infrared luminosities. Using the Gehan and the logrank tests, we find that there is about 59% and 24% chance of observing the difference in medians if the LoBAL and the non-LoBAL

samples were drawn from the same distribution. We conclude that LoBALs do not show statistically significant differences in infrared luminosity compared to non-LoBALs.

We also find that LoBALs do not harbor intrinsically more infrared luminous AGN. In Fig. 2.5, we show the distributions of the AGN infrared luminosities for LoBALs and non-LoBALs. The medians for the two types of objects are 11.61 and 11.48, respectively. This implies that the infrared-to-optical ratio in LoBALs and non-LoBALs is comparable. This suggests that the dusty material obscuring the nuclear source has similar covering fractions.

IR luminosity due to Star Formation

Although in normal galaxies the FIR emission is usually attributed to dust emission excited by star-formation, it is now known that in AGN the central nuclear source contributes significantly to the dust heating (e.g., Evans et al., 2006; Veilleux et al., 2009). Hence, removing the AGN contribution to the IR emission is important when quantifying the star formation activity in the galaxy and deriving star-formation rates from the total infrared luminosity using the Kennicutt (1998) relation.

We estimate the star formation contribution to the far-infrared luminosity, L_{IR}^{SF}, by integrating the warm and cold components of the best-fit SED model, thus, removing the AGN contribution. The median star formation luminosity of our LoBAL sample is $log(L_{IR}^{SF}/L_{\odot}) \approx 11.52$ and ≈ 11.35 for the control sample of non-LoBALs, when considering all objects, including those with MIPS upper limits. LoBALs have higher median star formation luminosities, $log(L_{IR,LoBAL}^{SF}/L_{\odot}) \approx 11.97$, than the non-LoBALs,

$log(L^{SF}_{IR,control}/L_{\odot}) \approx 11.72$, when we compare only the subset of objects with FIR detections for which the SEDs are well constrained.

The median contribution from star formation to the total IR luminosity from 8−1000 μm, $\frac{L^{SB}_{IR}}{L^{total}_{IR,8-1000\mu m}}$ (Table 2.5, column (6)), in LoBALs is 41% and in non-LoBALs 48% (70% and 62%, respectively, if only the FIR detections are considered). Although we do observe significant variations among individual objects, from as low as 25% to as high as 83% in LoBALs and between 3% and 84% in non-LoBALs, there is no significant difference between the samples. In the presence of mostly upper limits in the FIR MIPS bands, we use the Gehan and the logrank survival analysis statistical tests (Feigelson & Nelson, 1985) and find the the probability of observing the slight difference in the median values is 79% and 96%, respectively, if LoBALs and the control non-LoBALs were drawn from the sample parent population.

Our estimate of the star formation activity in LoBALs is much higher than that found for all types of BALs by Gallagher et al. (2007). They report that less than 20% of the total FIR flux in BALs arises due to star formation. Gallagher et al. (2007) model the radio to x-ray SEDs of a large sample of 38 BALs at z $>$ 1.4, consisting of 32 Hi-BALs and 6 LoBALs. Although they state that the quasar likely dominates the far-infrared emission in BALs, they note that the two most luminous starbursts in their sample are LoBALs, and the preponderance of upper limits at far-infrared wavelengths for the majority of the Lo- and Hi-BALs hampers their ability to draw definitive conclusions on the issue.

2.4.5 Trends with IR luminosity

In Fig. 2.6 we plot the IR luminosity from the starburst, L_{IR}^{SB}, versus the AGN contribution to the IR flux from 8−1000 μm, $L_{IR,8-1000\mu m}^{AGN}$. At a first glance, we see that the presence of silicate emission in LoBALs is correlated with the AGN IR luminosity, which may suggest that the weak silicate emission we see in LoBALs is directly excited by the central nuclear source. All LoBALs with $log(L_{IR,8-1000\mu m}^{AGN}/L_{\odot}) > 11.55$ show silicate emission. However, whether the silicate feature is detected is entirely dependent on the signal-to-noise ratio (S/N) of the IRS spectra. We tested this by introducing artificial noise to the spectra of the objects with detected silicate emission using the *IRAF* task *mknoise*, creating spectra with S/N equal to the median of the silicate non-detections, S/N $\sim$ 1.5. The silicate emission we observe in nine of the LoBALs would not have been detected if the IRS data had lower quality. We conclude that the non-detection of silicate in the majority of the LoBALs might be simply a low S/N effect.

PAH emission is favored among the LoBALs with starburst IR luminosities $\log(L_{IR}^{SB}/L_{\odot}) > 11.75$. Higher total IR luminosities for objects with PAH detections are also seen by Schweitzer et al. (2006) in PG QSOs. Four of the five LoBALs with MIPS detections at 70 and 160 μm are ULIRGs (i.e., $L_{IR,8-1000\mu m}^{total} > 10^{12} L_{\odot}$). Three of those objects show the strongest PAH features: SDSS J101151+542942, SDSS J161425+375210, and SDSS J170010+395545. There is one exception: SDSS J025026+000903 is a ULIRG and shows no PAHs, but has the strongest silicate emission feature of the entire sample.

2.4.6 Star formation rates in LoBALs

It has been shown that the total IR luminosity is a plausible star formation rate indicator (e.g., Kennicutt 1998 ($L_{IR} \sim 8{-}1000$ μm); Kewley et al. 2002; Mann et al. 2002 ($L_{IR} \sim 3{-}1000$ μm)). However, in AGN, much of the accretion disk UV and optical continuum is reprocessed by dust near the active nucleus and re-radiated in the infrared. By breaking down the different components that contribute to the overall SED (i.e., AGN, hot, warm, and cold dust), we partially alleviate the problem of AGN contamination to the FIR flux. With the explicit assumption that the starburst component of the IR luminosity is dominated by warm and cold dust re-processed light from O and B stars, we calculate SFRs from the total starburst infrared luminosity, L_{IR}^{SB}, using the Kennicutt (1998) relationship (Table 2.5, column (8)). Rieke et al. (2009) show that the choice of initial mass function (IMF) is crucial in calibrating the SFR and, by adopting a Salpeter-like slope with more shallow slope at low masses, estimate a correction to the Kennicutt (1998) SFR of $\mathrm{SFR}_{Rieke09} = 0.66 \times \mathrm{SFR}_{Kennicutt98}$. Although such an IMF fits better extragalactic star forming regions (Rieke et al., 2009), the SFRs given here are estimated with the Kennicutt (1998) relationship and are not to be interpreted literally but comparatively.

Even removing the AGN contribution to the FIR flux, there is possibly still contribution from older stellar populations (e.g., Devereux & Eales, 1989; Popescu et al., 2000) and from the AGN itself. Hiner et al. (2009) find evidence for non-starburst contribution to what we call the starburst IR flux. They model the SEDs of a sample of type-1 and type-2 QSOs in the same way we do, and they estimate SFRs with the Kennicutt (1998) relationship using the total model IR luminosity corrected for the AGN contribution and

the total integrated PAH luminosity. They find slightly lower SFRs derived from the PAH luminosity than from the starburst IR luminosity. This discrepancy is interpreted as the presence of an additional AGN contribution to the FIR flux, which has not been accounted for in the modeling. However, we also note that PAH emission can be affected by the presence of dust because the silicate opacity curve peaks in close proximity to some of the PAH features (Kemper et al., 2004). And although mounting evidence supports the prediction that PAH carriers are destroyed by the AGN radiation (e.g., Voit, 1992), it is still not clear whether or not the presence of an AGN enhances the PAH emission because the AGN emits UV radiation, which, in principle, can excite PAH emission (e.g., Smith et al., 2007).

We find that the host galaxies of LoBALs have a range of star formation rates. With the caveat that most of our results are upper limits due to non-detections in the MIPS 70 and 160 μm bands, we find that the median SFR in LoBALs is on the order of ~ 52 $M_{\odot}$ yr^{-1} and in non-LoBALs ~ 38 $M_{\odot}$ yr^{-1}. Four LoBALs have particularly high star formation rates of ~ 150 $M_{\odot}$ yr^{-1}, for SDSS J101151+542942 and SDSS J170010+395545, and $\sim$300 $M_{\odot}$ yr^{-1}, for SDSS J161425+375210 and SDSS J025026+000903. Similar fraction of the non-LoBALs have SFRs $\sim$100$-$300 $M_{\odot}$ yr^{-1}. We note that two of those four LoBALs (SDSS J161425+375210 and SDSS J170010+395545) and all, but one, of the highly star-forming non-LoBALs, do not have strong constrains on the FIR emission from cold dust since we only have upper limits at 160 μm. If we consider only the five LoBALs and 17 non-LoBALs with well constrained far-infrared luminosities, we find higher median star formation rate in LoBALs, $\sim$160 $M_{\odot}$ yr^{-1}, than in non-LoBALs, ~ 90 $M_{\odot}$ yr^{-1}.

2.5 Discussion

Mid-IR spectral properties

The low-resolution mid-IR spectra of LoBALs show a wide range of properties. We find that about 45% of the LoBALs show weak 9.7 μm silicate emission ($S_{9.7} = 0.34-0.81$), which is typical of other type-1 QSOs. Weak PAH emission is observed in 25% of the LoBALs, testifying to the presence of current star-formation in their hosts. Although about 40% of the LoBALs have featureless, low S/N spectra, we determined that the low quality of the mid-infrared data affects the detection of silicate.

The 9.7 μm silicate feature is exclusively seen in weak emission in about half of the LoBALs. This supports the previously observed dichotomy between type-1 and type-2 QSOs, that is, the silicate feature appears in weak emission in the former and in weak absorption in the latter. Even the ULIRGs among LoBALs exhibit silicate emission rather than the typical deep silicate absorption seen in the majority of ULIRGs (e.g., Spoon et al. 2007; see also Hao et al. 2005a). Hence, in terms of their silicate feature, LoBALs resemble type-1 QSOs with their typical weak silicate emission. In the context of the orientation model in which BALs are present in all type-1 QSOs, but observed only at limited viewing angles, the similarity of the silicate dust emission in LoBALs and in non-LoBALs indicates that the viewing angle for LoBALs is, not surprisingly, closer to those of type-1 QSOs than to those of type-2 QSOs. On the other hand, in the context of an evolution model in which deeply embedded AGN evolve to become unobscured type-1 QSOs, our results would imply that LoBALs mark one of the last stages of the transition. At this stage, the nuclear region

has been cleared up of the thick dust envelope responsible for the deep absorption seen in other dust-obscured objects such as ULIRGs.

Yet, the optical spectra of our LoBALs suffer from high levels of obscuration. We estimate the AGN extinction in the optical from the SED fit, which includes SMC extinction law, and find a median value of $A_V = 0.43$ and a range $A_V = 0 - 1$ (Table 2.7), indicating significant levels of obscuration in some LoBALs. LoBALs are known to have intrinsically bluer optical-UV continua than normal QSOs (i.e., Richards et al., 2002), and so the derived A_V values are likely underestimated. The non-LoBALs of the control sample suffer significantly less extinction at a median level of $A_V = 0.06$ (Table 2.7). We estimate the median color excess, $E(B-V)$ in LoBALs, using the SMC extinction law and $R_V = 2.72$, to be $E(B-V) \approx 0.14$, a value comparable to previous studies of LoBALs by Sprayberry & Foltz (1992) and Gibson et al. (2009), who find SMC-type color excess of 0.12 and 0.14, respectively, but somewhat higher than the value of 0.077 reported by Reichard et al. (2003b).

Infrared luminosities

LoBALs span a range of infrared luminosities. Nevertheless, they have median total and starburst infrared luminosities comparable to those of non-LoBALs. The majority of the objects were not detected in the FIR MIPS bands at 70 and 160 μm. For those, roughly three-fourths of each sample, we have only upper limit estimates of their infrared luminosities. Using the Gehan and the logrank survival statistical tests, we find that the probabilities that the LoBAL and the non-LoBAL samples are drawn from the same distri-

bution are 59% and 24%, respectively, considering the slight difference in the median total infrared luminosity, and 79% and 96%, respectively, considering the differences in the median starburst infrared luminosity. We conclude that the infrared luminosities of LoBALs are not statistically different from those of non-LoBALs.

We find a possible correlation between the extinction-corrected absolute M_i magnitude and the starburst luminosity of the objects with FIR detections (see Fig. 2.7a). This implies that the star formation rates are higher in the more optically luminous sources. However, since the majority of the measurements are upper limits (22 detections vs. 28 upper limits), we are not able to properly quantify the slope or the scatter in the correlation. Similarly, evidence for a correlation between the optical 5100 $\mathring{A}$ luminosity and the 60 μm IRAS flux was found in low-redshift PG QSOs by Netzer et al. (2007), who proposed the correlation was mostly due to star formation. We note that the control sample of non-LoBALs is well matched to the absolute M_i magnitudes of the LoBALs (Figure 2.7) . The range of M_i, corrected for Galactic extinction, for the LoBALs is $-22.41 > M_i > -25.55$, with a median of $M_i = -24.10$ (median of the FIR-detections is -23.68). For the control non-LoBALs, the range is $-22.17 > M_i > -25.53$, with a median of $M_i = -23.96$ (median of the FIR-detections is -23.85).

We also find a correlation between the AGN infrared luminosity and the optical i-band luminosity (Fig. 2.7b), $L_{IR}^{AGN} \sim L_i^{\alpha}$ with a slope $\alpha \simeq 0.29 \pm 0.05$. This relationship holds for both LoBALs and non-LoBALs and covers over three orders of optical magnitude. If the AGN infrared luminosity arises mostly from dusty obscuring material close to the

central source, then this correlation implies that LoBALs and non-LoBALs have comparable covering fractions.

Star formation

Star formation contributes a median of 41% and 48% of the FIR power in LoBALs and non-LoBALs, respectively, with large variations among individual objects, in agreement with the value found by Schweitzer et al. (2006) for PG QSOs at $z < 0.3$ who claim that star formation contributes at least 30% of their FIR luminosity.

We estimate SFRs from the FIR luminosity solely contributed by the starburst. With the exception of four LoBALs with SFRs $\sim 150 - 300$ $M_\odot$ yr^{-1}, and with the caveat that we only have upper limits for most of the other objects, we find that LoBALs have SFRs ~ 52 $M_\odot$ yr^{-1}, slightly higher but comparable to the value we find for non-LoBALs, 38 $M_\odot$ yr^{-1} . However, we note that for the most star-forming galaxies, those with FIR MIPS detections, the median SFR in LoBALs (~ 161 $M_\odot$ yr^{-1}) is higher than the median SFR in non-LoBAL type-1 hosts (~ 90 $M_\odot$ yr^{-1}).

LoBALs hitherto and future work

Overall, our results suggest that LoBALs are very similar to non-LoBALs in terms of their mid-infrared spectral properties and far-infrared luminosities. This fits the orientation scenario, which would predict comparable levels of star formation for LoBALs and non-LoBALs if both are drawn from the same parent population. Our results, however,

cannot rule out an evolutionary paradigm, where LoBALs are rapidly transitioning from a dusty phase marked by high SFRs to a more quiescent phase with SFRs typical of non-BALs.

The majority of the LoBALs in our sample have SFRs comparable to non-LoBALs, which in the framework of the evolutionary model implies that most of the LoBALs have already passed through the event that quenched the star formation in the galaxy to the levels seen in normal QSO hosts. Our results show that there are large variations among individual LoBALs. Finding that only 20% of the LoBALs have SFRs 80% higher than those found in the IR-luminous non-LoBAL implies that the period during which the star formation was quenched was very brief during the short LoBAL transition phase. If the SFRs in both samples were found to be much higher, but still comparable, a stronger claim could be made that BAL outflows alone are not responsible for quenching the star formation on galactic scale, but that was not observed.

While the *Spitzer* observations explore the relation between LoBALs and star formation, they are not sufficient to test whether the LoBAL phenomenon is indeed related to the early stages of QSO activity. Moreover, due to the preponderance of upper limits, our *Spitzer* results do not allow us to draw strong conclusions about the nature of LoBALs. This study will be complemented by *HST* imaging and Keck spectroscopy programs of this sample, which will help us study the host galaxy morphologies and the ages of the dominant stellar populations. On one hand, correlating the merger stage with spectral characteristics will give us a deeper insight into the dynamics involved and help us constrain an evolutionary connection between unobscured QSOs and LoBALs. On the other hand, the stellar ages

will help us constrain the time scales involved in fueling of the nucleus and the onset (and perhaps quenching) of star formation.

2.6 Conclusion

We investigate the mid- and far-IR properties of a volume-limited sample of 22 low-ionization broad absorption line QSOs within the redshift range $0.5 < z < 0.6$. We model their SEDs from the optical to the far-infrared in an effort to estimate total infrared luminosities, the relative contributions from the starburst and the AGN, starburst luminosities, and star formation rates corrected for the AGN contamination of the FIR emission. We compare this LoBAL sample to a control sample of non-LoBALs, matched by M_i within the redshift $0.45 < z < 0.83$, to examine the possible connection between these two classes of QSOs. We find that LoBALs are indistinguishable from non-LoBAL type-1 QSO in terms of their MIR spectral properties and FIR luminosities.

Table 2.1: SDSS DR7 PSF magnitudes corrected for the given here Galactic extinction.

#	SDSS Object ID	Redshift	M_i [AB mag]	E($B-V$) [AB mag]	u [AB mag]	g [AB mag]	r [AB mag]	i [AB mag]	z [AB mag]
				LoBAL sample					
1	J023102.49−083141.2	0.596	-23.54	0.04	19.54 ± 0.04	19.17 ± 0.01	19.16 ± 0.02	18.96 ± 0.02	18.93 ± 0.06
2	J023153.63−093333.5	0.587	-23.39	0.03	19.95 ± 0.05	19.37 ± 0.01	19.24 ± 0.01	18.96 ± 0.02	18.96 ± 0.05
3	J025026.66+000903.4	0.554	-24.05	0.07	20.90 ± 0.13	19.84 ± 0.02	19.10 ± 0.01	18.57 ± 0.01	18.46 ± 0.04
4	J083525.98+435211.2	0.568	-25.14	0.03	18.31 ± 0.02	17.48 ± 0.01	17.47 ± 0.01	17.27 ± 0.01	17.32 ± 0.01
5	J085053.12+445122.5	0.541	-25.11	0.03	17.84 ± 0.01	17.44 ± 0.01	17.33 ± 0.01	17.19 ± 0.01	17.27 ± 0.01
6	J085215.66+492040.8	0.566	-23.82	0.02	19.37 ± 0.03	18.94 ± 0.01	18.77 ± 0.01	18.57 ± 0.01	18.57 ± 0.03
7	J085357.87+463350.6	0.550	-24.43	0.02	18.67 ± 0.02	18.18 ± 0.01	18.19 ± 0.01	17.89 ± 0.01	17.83 ± 0.02
8	J101151.95+542942.7	0.536	-23.32	0.01	20.08 ± 0.04	19.60 ± 0.02	19.34 ± 0.01	18.91 ± 0.01	19.04 ± 0.04
9	J102802.32+592906.6	0.535	-23.47	0.01	18.94 ± 0.02	18.76 ± 0.01	18.89 ± 0.01	18.75 ± 0.01	18.82 ± 0.06
10	J105102.77+525049.8	0.543	-23.40	0.01	19.88 ± 0.05	19.31 ± 0.01	19.24 ± 0.01	18.87 ± 0.01	18.85 ± 0.04
11	J105404.73+042939.3	0.578	-23.47	0.04	20.20 ± 0.05	19.55 ± 0.01	19.43 ± 0.01	19.00 ± 0.01	19.05 ± 0.04
12	J112822.41+482309.9	0.543	-25.05	0.02	18.51 ± 0.02	17.83 ± 0.01	17.56 ± 0.01	17.23 ± 0.01	17.17 ± 0.01
13	J114043.62+532439.0	0.530	-24.07	0.01	18.73 ± 0.02	18.32 ± 0.01	18.32 ± 0.01	18.14 ± 0.01	18.13 ± 0.02
14	J130952.89+011950.6	0.547	-25.12	0.04	17.79 ± 0.01	17.47 ± 0.01	17.41 ± 0.01	17.21 ± 0.01	17.20 ± 0.01
15	J140025.53−012957.0	0.584	-24.43	0.05	19.49 ± 0.04	18.49 ± 0.01	18.30 ± 0.01	18.09 ± 0.01	18.10 ± 0.03
16	J141946.36+463424.3	0.546	-22.41	0.01	20.89 ± 0.07	20.44 ± 0.02	20.33 ± 0.02	19.87 ± 0.02	19.48 ± 0.05
17	J142649.24+032517.7	0.530	-24.18	0.04	18.80 ± 0.03	18.37 ± 0.01	18.33 ± 0.01	18.08 ± 0.01	18.01 ± 0.02
18	J142927.28+523849.5	0.594	-25.29	0.01	18.03 ± 0.01	17.56 ± 0.01	17.48 ± 0.01	17.19 ± 0.01	17.30 ± 0.01
19	J161425.17+375210.7	0.553	-25.55	0.02	17.24 ± 0.01	16.92 ± 0.00	16.92 ± 0.00	16.77 ± 0.01	16.89 ± 0.01
20	J170010.83+395545.8	0.577	-23.40	0.02	19.80 ± 0.04	19.45 ± 0.01	19.26 ± 0.01	19.03 ± 0.01	18.91 ± 0.05
21	J170341.82+383944.7	0.554	-24.14	0.04	19.95 ± 0.04	19.08 ± 0.01	18.65 ± 0.01	18.23 ± 0.01	18.17 ± 0.03
22	J204333.20−001104.2	0.545	-24.82	0.06	18.43 ± 0.02	18.01 ± 0.01	17.79 ± 0.01	17.56 ± 0.01	17.64 ± 0.02
				Control sample of non-LoBALs					
1	J103236.22+580033.9	0.687	-23.20	0.006	20.23 ± 0.05	19.85 ± 0.03	19.82 ± 0.03	19.63 ± 0.03	19.79 ± 0.08
2	J103333.92+582818.8	0.574	-22.17	0.007	20.78 ± 0.07	20.29 ± 0.03	20.40 ± 0.04	20.22 ± 0.05	20.06 ± 0.14
3	J103651.94+575950.9	0.500	-23.45	0.006	19.48 ± 0.03	19.05 ± 0.02	18.79 ± 0.02	18.60 ± 0.02	18.50 ± 0.04
4	J103721.15+590755.7	0.603	-23.03	0.008	20.04 ± 0.15	19.43 ± 0.03	19.59 ± 0.02	19.49 ± 0.02	19.67 ± 0.10
5	J104210.25+594253.5	0.675	-23.17	0.012	19.85 ± 0.09	19.66 ± 0.04	19.65 ± 0.02	19.63 ± 0.04	19.70 ± 0.12
6	J104526.73+595422.6	0.646	-23.85	0.011	19.44 ± 0.05	19.06 ± 0.03	19.14 ± 0.02	18.83 ± 0.03	18.84 ± 0.05
7	J104556.84+570747.0	0.541	-23.24	0.007	19.21 ± 0.03	18.95 ± 0.02	19.06 ± 0.02	19.00 ± 0.03	18.99 ± 0.04
8	J104625.02+584839.1	0.577	-23.70	0.010	19.06 ± 0.02	18.76 ± 0.03	18.84 ± 0.03	18.70 ± 0.02	18.78 ± 0.04
9	J104633.70+571530.4	0.712	-24.16	0.008	19.03 ± 0.02	18.72 ± 0.01	18.77 ± 0.02	18.75 ± 0.01	18.76 ± 0.03
10	J104840.28+563635.6	0.714	-23.86	0.007	19.67 ± 0.04	19.25 ± 0.03	19.20 ± 0.02	19.06 ± 0.02	18.90 ± 0.05
11	J104857.92+560112.3	0.800	-24.25	0.009	19.15 ± 0.02	18.81 ± 0.04	18.82 ± 0.01	18.95 ± 0.02	18.77 ± 0.04
12	J105000.21+581904.2	0.833	-25.53	0.008	17.87 ± 0.01	17.67 ± 0.02	17.64 ± 0.02	17.77 ± 0.01	17.68 ± 0.03
13	J105106.12+591625.1	0.768	-24.78	0.009	18.60 ± 0.03	18.22 ± 0.03	18.27 ± 0.02	18.33 ± 0.02	18.19 ± 0.03
14	J105518.08+570423.5	0.696	-24.13	0.007	18.87 ± 0.02	18.59 ± 0.02	18.71 ± 0.01	18.73 ± 0.02	18.68 ± 0.03
15	J105604.00+581523.4	0.832	-24.36	0.007	19.02 ± 0.03	18.89 ± 0.02	18.81 ± 0.03	18.93 ± 0.02	18.81 ± 0.03
16	J105959.93+574848.1	0.453	-23.76	0.006	18.86 ± 0.03	18.36 ± 0.03	18.25 ± 0.02	18.05 ± 0.02	17.81 ± 0.02
17	J160015.68+552259.9	0.673	-24.36	0.007	18.90 ± 0.03	18.54 ± 0.02	18.54 ± 0.01	18.42 ± 0.02	18.36 ± 0.04
18	J160128.54+544521.3	0.728	-24.93	0.010	18.37 ± 0.02	18.12 ± 0.02	18.06 ± 0.02	18.05 ± 0.02	18.00 ± 0.03
19	J160341.44+541501.5	0.580	-23.23	0.008	19.61 ± 0.05	19.26 ± 0.02	19.30 ± 0.03	19.19 ± 0.03	19.14 ± 0.05
20	J160523.10+545613.3	0.572	-23.63	0.009	19.12 ± 0.04	18.84 ± 0.04	18.91 ± 0.03	18.76 ± 0.02	18.81 ± 0.05
21	J160630.60+542007.5	0.820	-24.43	0.008	18.97 ± 0.03	18.75 ± 0.03	18.72 ± 0.02	18.83 ± 0.03	18.61 ± 0.04
22	J160908.95+533153.2	0.816	-24.57	0.010	19.01 ± 0.03	18.48 ± 0.03	18.48 ± 0.04	18.68 ± 0.02	18.50 ± 0.03
23	J163031.46+410145.6	0.531	-23.48	0.008	18.90 ± 0.02	18.69 ± 0.02	18.87 ± 0.01	18.72 ± 0.02	18.66 ± 0.03
24	J163135.46+405756.4	0.750	-24.19	0.009	19.48 ± 0.03	19.00 ± 0.01	18.85 ± 0.02	18.86 ± 0.02	18.67 ± 0.04
25	J163143.76+404735.6	0.538	-23.55	0.008	19.57 ± 0.03	19.11 ± 0.02	18.95 ± 0.02	18.68 ± 0.02	18.65 ± 0.03
26	J163352.34+402115.5	0.782	-24.05	0.007	19.21 ± 0.03	18.86 ± 0.02	18.95 ± 0.02	19.10 ± 0.02	18.88 ± 0.05
27	J163502.80+412952.9	0.472	-23.97	0.006	18.15 ± 0.02	17.94 ± 0.02	17.97 ± 0.01	17.94 ± 0.02	17.91 ± 0.02
28	J163854.62+415419.5	0.711	-24.30	0.009	19.05 ± 0.05	18.78 ± 0.02	18.68 ± 0.02	18.62 ± 0.02	18.60 ± 0.03
29	J171126.94+585544.2	0.537	-23.49	0.024	19.16 ± 0.03	18.80 ± 0.02	18.90 ± 0.02	18.77 ± 0.02	18.72 ± 0.05
30	J171334.02+595028.3	0.615	-24.62	0.021	18.16 ± 0.02	17.88 ± 0.01	18.00 ± 0.02	17.96 ± 0.02	18.13 ± 0.03
31	J171736.90+593011.4	0.600	-23.78	0.021	19.21 ± 0.03	18.81 ± 0.02	18.90 ± 0.02	18.75 ± 0.02	18.83 ± 0.05
32	J171748.43+594820.6	0.763	-25.02	0.022	18.27 ± 0.03	17.99 ± 0.02	18.02 ± 0.02	18.10 ± 0.02	18.05 ± 0.03
33	J171818.14+584905.2	0.634	-24.18	0.028	19.00 ± 0.03	18.59 ± 0.02	18.60 ± 0.02	18.50 ± 0.02	18.64 ± 0.04
34	J172104.75+592451.4	0.786	-23.85	0.028	19.62 ± 0.04	19.39 ± 0.02	19.32 ± 0.02	19.35 ± 0.03	19.13 ± 0.06
35	J172414.05+593644.0	0.745	-24.29	0.025	19.33 ± 0.03	18.90 ± 0.02	18.80 ± 0.01	18.77 ± 0.02	18.55 ± 0.03

Table 2.2: 2MASS and *Spitzer* MIPS infrared photometry.

#	SDSS Object ID	J [Vega mag]	H [Vega mag]	K_s [Vega mag]	f_{24} [mJy]	f_{70} [mJy]	f_{160} [mJy]
				LoBAL sample			
1	J023102.49−083141.2	···	···	15.71 ± 0.23	5.04 ± 0.20	< 19.63	< 29.30
2	J023153.63−093333.5	···	···	15.92 ± 0.25	1.17 ± 0.17	< 20.55	< 22.21
3	J025026.66+000903.4	17.10 ± 0.18	···	15.42 ± 0.15	10.18 ± 0.20	86.66 ± 6.68	86.64 ± 15.02
4	J083525.98+435211.2	16.43 ± 0.13	15.98 ± 0.20	15.14 ± 0.12	···	···	···
5	J085053.12+445122.5	16.24 ± 0.11	15.98 ± 0.20	14.92 ± 0.12	5.68 ± 0.16	< 17.56	< 23.17
6	J085215.66+492040.8	···	···	···	1.30 ± 0.16	< 17.07	< 21.88
7	J085357.87+463350.6	16.78 ± 0.17	···	15.29 ± 0.15	1.90 ± 0.16	< 16.08	< 20.78
8	J101151.95+542942.7	···	···	···	4.52 ± 0.16	49.81 ± 7.18	37.44 ± 7.98
9	J102802.32+592906.6	···	···	···	···	···	···
10	J105102.77+525049.8	17.31 ± 0.23	···	15.19 ± 0.12	3.28 ± 0.15	< 18.41	< 17.80
11	J105404.73+042939.3	···	···	···	···	···	···
12	J112822.41+482309.9	16.07 ± 0.12	15.39 ± 0.14	14.45 ± 0.09	···	···	···
13	J114043.62+532439.0	16.95 ± 0.20	···	15.31 ± 0.17	···	···	···
14	J130952.89+011950.6	15.93 ± 0.09	15.34 ± 0.11	14.61 ± 0.10	10.21 ± 0.24	< 20.93	< 27.58
15	J140025.53−012957.0	···	···	···	1.79 ± 0.20	< 28.43	< 30.49
16	J141946.36+463424.3	···	···	···	2.02 ± 0.14	< 17.10	54.75 ± 7.75
17	J142649.24+032517.7	16.75 ± 0.19	16.03 ± 0.17	15.19 ± 0.17	5.85 ± 0.20	< 20.50	···
18	J142927.28+523849.5	16.27 ± 0.10	15.59 ± 0.12	14.85 ± 0.09	8.84 ± 0.17	< 14.17	< 25.28
19	J161425.17+375210.7	16.10 ± 0.08	15.44 ± 0.12	14.38 ± 0.08	20.06 ± 0.21	110.26 ± 6.63	···
20	J170010.83+395545.8	···	···	15.65 ± 0.21	4.91 ± 0.16	45.32 ± 6.43	···
21	J170341.82+383944.7	16.82 ± 0.17	16.02 ± 0.20	15.44 ± 0.17	8.83 ± 0.17	< 17.54	···
22	J204333.20−001104.2	16.84 ± 0.15	15.80 ± 0.15	15.24 ± 0.15	5.31 ± 0.18	< 15.23	···
				Control sample of non-LoBALs			
1	103236.22+580033.9	18.46 0.26	17.59 0.28	··· 0.00	1.16 ± 0.02	< 4.41 ± 1.47	< 12.46 ± 4.15
2	103333.92+582818.8	···	···	16.57 ± 0.15	0.74 ± 0.02	< 4.52 ± 1.51	< 13.12 ± 4.37
3	103651.94+575950.9	16.96 ± 0.19	16.05 ± 0.20	15.40 ± 0.18	4.59 ± 0.02	27.97 ± 2.14	< 12.19 ± 4.06
4	103721.15+590755.7	18.70 ± 0.23	···	16.90 ± 0.20	2.13 ± 0.02	< 4.36 ± 1.45	< 14.41 ± 4.80
5	104210.25+594253.5	18.45 ± 0.24	···	···	1.08 ± 0.02	< 3.92 ± 1.31	< 17.06 ± 5.69
6	104526.73+595422.6	17.78 ± 0.17	16.64 ± 0.14	16.11 ± 0.15	4.38 ± 0.02	8.20 ± 2.53	< 12.48 ± 4.16
7	104556.84+570747.0	17.86 ± 0.14	16.94 ± 0.18	16.28 ± 0.15	2.72 ± 0.02	< 4.46 ± 1.49	< 11.76 ± 3.92
8	104625.02+584839.1	17.97 ± 0.17	16.87 ± 0.19	16.05 ± 0.13	3.88 ± 0.02	< 3.35 ± 1.12	< 7.79 ± 2.60
9	104633.70+571530.4	17.57 ± 0.12	···	16.10 ± 0.13	1.84 ± 0.02	< 4.75 ± 1.58	< 9.52 ± 3.17
10	104840.28+563635.6	17.80 ± 0.14	16.85 ± 0.15	16.42 ± 0.19	2.66 ± 0.02	< 5.78 ± 1.93	< 11.93 ± 3.98
11	104857.92+560112.3	17.55 ± 0.13	···	16.54 ± 0.23	1.37 ± 0.02	27.09 ± 2.05	< 12.11 ± 4.04
12	105000.21+581904.2	16.80 ± 0.16	16.20 ± 0.24	15.46 ± 0.18	4.62 ± 0.02	< 4.62 ± 1.54	< 12.93 ± 4.31
13	105106.12+591625.1	17.17 ± 0.11	16.62 ± 0.13	15.34 ± 0.15	5.39 ± 0.02	23.33 ± 2.15	< 10.41 ± 3.47
14	105518.08+570423.5	17.61 ± 0.16	···	16.36 ± 0.17	3.55 ± 0.02	< 5.49 ± 1.83	< 9.51 ± 3.17
15	105604.00+581523.4	17.28 ± 0.13	16.87 ± 0.21	16.23 ± 0.22	4.09 ± 0.02	< 3.70 ± 1.23	< 11.50 ± 3.83
16	105959.93+574848.1	16.65 ± 0.16	16.08 ± 0.22	15.48 ± 0.16	9.04 ± 0.03	17.31 ± 2.45	< 11.23 ± 3.74
17	160015.68+552259.9	···	···	15.70 ± 0.22	4.48 ± 0.02	17.3733 ± 2.54	< 11.66 ± 3.89
18	160128.54+544521.3	16.78 ± 0.24	···	16.13 ± 0.30	12.93 ± 0.02	38.14 ± 2.57	< 11.68 ± 3.89
19	160341.44+541501.5	17.22 ± 0.33	···	···	1.18 ± 0.02	< 6.78 ± 2.26	< 11.01 ± 3.67
20	160523.10+545613.3	···	···	16.07 ± 0.27	4.74 ± 0.02	7.88 ± 1.81	< 10.78 ± 3.59
21	160630.60+542007.5	···	···	···	5.56 ± 0.02	< 4.77 ± 1.59	< 10.17 ± 3.39
22	160908.95+533153.2	···	16.22 ± 0.20	···	3.03 ± 0.02	< 4.92 ± 1.64	< 11.28 ± 3.76
23	163031.46+410145.6	···	···	15.69 ± 0.24	2.17 ± 0.02	12.03 ± 1.69	< 4.47 ± 1.49
24	163135.46+405756.4	17.33 ± 0.32	16.21 ± 0.24	···	4.3 ± 0.02	10.98 ± 1.99	< 4.57 ± 1.52
25	163143.76+404735.6	17.13 ± 0.28	···	15.96 ± 0.27	3.9 ± 0.02	13.91 ± 1.88	< 4.71 ± 1.57
26	163352.34+402115.5	17.16 ± 0.27	···	···	2.86 ± 0.02	13.88 ± 2.23	< 4.56 ± 1.52
27	163502.80+412952.9	17.08 ± 0.22	16.30 ± 0.21	15.22 ± 0.16	3.92 ± 0.02	< 5.13 ± 1.71	< 5.30 ± 1.77
28	163854.62+415419.5	17.41 ± 0.33	···	···	2.91 ± 0.02	< 4.21 ± 1.40	< 4.54 ± 1.51
29	171126.94+585544.2	···	···	···	3.45 ± 0.07	29.10 ± 2.24	98.32 ± 11.27
30	171334.02+595028.3	17.12 ± 0.27	16.50 ± 0.24	15.47 ± 0.20	5.38 ± 0.07	< 1.99 ± 0.66	< 20.21 ± 6.74
31	171736.90+593011.4	17.63 ± 0.35	···	···	6.38 ± 0.05	19.81 ± 1.46	< 12.33 ± 4.11
32	171748.43+594820.6	17.20 ± 0.33	···	···	3.04 ± 0.04	10.34 ± 1.30	< 7.72 ± 2.57
33	171818.14+584905.2	···	···	···	4.06 ± 0.06	30.43 ± 2.26	< 7.05 ± 2.35
34	172104.75+592451.4	17.39 ± 0.32	···	16.19 ± 0.29	4.44 ± 0.06	12.56 ± 2.10	< 18.29 ± 6.10
35	172414.05+593644.0	···	···	15.75 ± 0.24	1.81 ± 0.06	< 3.58 ± 1.19	< 16.80 ± 5.60

Table 2.3: Control sample of non-LoBALs: MIPS data fields and archival IRAC photometry.

#	SDSS Object ID	MIPS field	$f_{3.6}$ (μJy)	$f_{4.5}$ (μJy)	$f_{5.8}$ (μJy)	$f_{8.0}$ (μJy)
1	103236.22+580033.9	SWIRE−Lockman Hole	168.4 ± 1.0	245.0 ± 1.3	342.8 ± 4.7	492.8 ± 4.7
2	103333.92+582818.8	SWIRE−Lockman Hole	170.2 ± 1.4	188.0 ± 2.0	233.4 ± 5.4	247.0 ± 5.7
3	103651.94+575950.9	SWIRE−Lockman Hole	694.2 ± 3.6	864.5 ± 4.2	1079.7 ± 11.0	1368.0 ± 8.3
4	103721.15+590755.7	SWIRE−Lockman Hole	249.7 ± 1.6	353.6 ± 2.7	520.3 ± 7.7	764.4 ± 7.0
5	104210.25+594253.5	SWIRE−Lockman Hole	250.3 ± 2.1	308.6 ± 1.8	375.1 ± 7.0	479.9 ± 4.6
6	104526.73+595422.6	SWIRE−Lockman Hole	646.2 ± 1.6	873.8 ± 2.8	1137.2 ± 5.9	1519.1 ± 6.0
7	104556.84+570747.0	SWIRE−Lockman Hole	440.0 ± 2.5	537.7 ± 2.9	676.6 ± 8.2	902.7 ± 6.7
8	104625.02+584839.1	SWIRE−Lockman Hole	634.7 ± 2.6	908.1 ± 3.5	1285.2 ± 10.0	1688.9 ± 7.0
9	104633.70+571530.4	SWIRE−Lockman Hole	553.6 ± 2.8	672.1 ± 3.5	792.0 ± 9.1	905.2 ± 6.6
10	104840.28+563635.6	SWIRE−Lockman Hole	383.3 ± 2.3	561.0 ± 3.0	812.9 ± 9.7	1054.0 ± 6.9
11	104857.92+560112.3	SWIRE−Lockman Hole	231.6 ± 2.1	291.2 ± 2.0	370.1 ± 7.7	595.5 ± 6.3
12	105000.21+581904.2	SWIRE−Lockman Hole	921.3 ± 4.2	1229.6 ± 5.0	1731.7 ± 13.7	2337.9 ± 10.0
13	105106.12+591625.1	SWIRE−Lockman Hole	971.1 ± 4.0	1210.5 ± 4.0	1641.8 ± 12.8	2068.6 ± 7.9
14	105518.08+570423.5	SWIRE−Lockman Hole	408.0 ± 2.8	543.4 ± 3.5	791.5 ± 10.4	1174.7 ± 8.6
15	105604.00+581523.4	SWIRE−Lockman Hole	437.1 ± 2.9	612.5 ± 3.0	924.1 ± 10.9	1326.3 ± 7.4
16	105959.93+574848.1	SWIRE−Lockman Hole	1189.6 ± 4.6	1526.6 ± 5.7	1993.4 ± 15.5	2708.3 ± 11.5
17	160015.68+552259.9	SWIRE−ELAIS N1	841.3 ± 2.7	1163.9 ± 4.8	1621.5 ± 9.4	2040.1 ± 9.5
18	160128.54+544521.3	SWIRE−ELAIS N1	1133.8 ± 4.3	1854.3 ± 5.3	2751.8 ± 16.4	3983.0 ± 11.2
19	160341.44+541501.5	SWIRE−ELAIS N1	328.9 ± 2.0	391.1 ± 2.8	489.3 ± 7.8	589.4 ± 6.3
20	160523.10+545613.3	SWIRE−ELAIS N1	682.4 ± 3.6	982.4 ± 4.7	1411.2 ± 12.8	1787.4 ± 9.6
21	160630.60+542007.5	SWIRE−ELAIS N1	735.7 ± 2.7	1077.8 ± 3.5	1599.1 ± 10.5	2302.4 ± 7.5
22	160908.95+533153.2	SWIRE−ELAIS N1	634.1 ± 2.5	831.9 ± 3.1	1136.3 ± 8.3	1451.7 ± 6.4
23	163031.46+410145.6	SWIRE−ELAIS N2	625.3 ± 3.3	713.3 ± 3.7	874.3 ± 9.9	1036.0 ± 7.1
24	163135.46+405756.4	SWIRE−ELAIS N2	582.9 ± 2.6	789.0 ± 3.1	1090.2 ± 9.7	1457.1 ± 6.5
25	163143.76+404735.6	SWIRE−ELAIS N2	682.6 ± 3.4	808.4 ± 3.9	1001.6 ± 9.4	1320.2 ± 7.7
26	163352.34+402115.5	SWIRE−ELAIS N2	460.8 ± 2.9	578.2 ± 3.4	797.3 ± 9.7	1083.8 ± 7.3
27	163502.80+412952.9	SWIRE−ELAIS N2	901.4 ± 3.2	1186.5 ± 4.9	1521.2 ± 10.6	1961.0 ± 9.2
28	163854.62+415419.5	SWIRE−ELAIS N2	532.0 ± 2.3	673.3 ± 3.2	850.5 ± 7.9	1131.0 ± 6.7
29	171126.94+585544.2	xFLS	641.4 ± 65.1	813.2 ± 82.4	951.0 ± 101.2	1216.0 ± 124.6
30	171334.02+595028.3	xFLS	763.2 ± 76.8	1015.4 ± 102.3	1456.1 ± 148.7	1732.3 ± 175.2
31	171736.90+593011.4	xFLS	457.5 ± 46.7	613.3 ± 62.0	771.2 ± 84.2	1366.4 ± 138.8
32	171748.43+594820.6	xFLS	647.8 ± 65.3	898.1 ± 90.9	1198.5 ± 124.3	1570.8 ± 160.1
33	171818.14+584905.2	xFLS	675.0 ± 68.3	869.1 ± 88.1	1152.5 ± 122.7	1493.2 ± 152.2
34	172104.75+592451.4	xFLS	362.1 ± 36.9	453.4 ± 46.6	642.1 ± 70.0	853.8 ± 89.2
35	172414.05+593644.0	xFLS	591.2 ± 59.5	751.8 ± 76.0	853.0 ± 89.0	1124.8 ± 114.8

Table 2.4: LoBALs: *Sptizer* MIPS and IRS observing log.

#	SDSS Object ID	z	MIPS	IRS						
					SL1			LL2		
			AORKEY	AORKEY	ramp duration (s)	# of cycles	integration time (s)	ramp duration (s)	# of cycles	integration time (s)
1	J023102.49−083141.2	0.596	26914048	···	···	···	···	···	···	···
2	J023153.63−093333.5	0.587	26912256	···	···	···	···	···	···	···
3	J025026.66+000903.4	0.554	26914560	26920192	14	1	29	30	3	189
4	J083525.98+435211.2	0.568	···	26918656	6	1	13	14	1	29
5	J085053.12+445122.5	0.541	26910208	26915840	14	1	29	30	3	189
6	J085215.66+492040.8	0.566	26912768	26918400	14	1	29	120	1	244
7	J085357.87+463350.6	0.550	26911744	26917376	14	1	29	30	3	189
8	J101151.95+542942.7	0.536	26909952	26915584	6	2	25	30	2	126
9	J102802.32+592906.6	0.535	···	26915328	14	1	29	120	1	244
10	J105102.77+525049.8	0.543	26910464	26916096	14	1	29	30	3	189
11	J105404.73+042939.3	0.578	···	26919168	14	2	59	120	1	244
12	J112822.41+482309.9	0.543	···	26916352	6	1	13	6	1	13
13	J114043.62+532439.0	0.530	···	26914816	14	1	29	30	3	189
14	J130952.89+011950.6	0.547	26911488	26917120	6	1	13	6	1	13
15	J140025.53−012957.0	0.584	26913792	26919424	6	2	25	120	1	244
16	J141946.36+463424.3	0.546	26911232	26916864	14	1	29	120	1	244
17	J142649.24+032517.7	0.530	28968448	26915072	14	2	59	120	2	488
18	J142927.28+523849.5	0.594	26914304	26919936	14	2	59	120	2	488
19	J161425.17+375210.7	0.553	26912000	26917632	14	2	59	120	2	488
20	J170010.83+395545.8	0.577	26913280	26918912	14	1	29	120	1	244
21	J170341.82+383944.7	0.554	26912512	26918144	14	1	29	120	1	244
22	J204333.20−001104.2	0.545	26910976	26916608	6	1	13	30	1	63

Table 2.5: LoBALs: Infrared luminosities and SFRs.

#	SDSS Object ID	$Log(L^{total}_{IR,8-1000\mu m})$	$Log(L^{SB}_{IR})$	$Log(L^{AGN}_{IR,8-1000\mu m})$	$\frac{L^{SB}_{IR}}{L^{total}_{IR,8-1000\mu m}}$	$Log(L^{MIPS}_{TIR})$	SFR^{SB}_{IR}
		$[Log(L_\odot)]$	$[Log(L_\odot)]$	$[Log(L_\odot)]$	[%]	$[Log(L_\odot)]$	$[M_\odot\ \mathrm{yr}^{-1}]$
(1)	(2)	(3)	(4)	(5)	(6)	(7)	(8)
1	J023102.49−083141.2	···	···	···	···	< 12.08	···
2	J023153.63−093333.5	···	···	···	···	< 11.63	···
3	J025026.66+000903.4	**12.39**	12.25	11.81	73	**12.49**	$310\ ^{+25}_{-30}$
4	J083525.98+435211.2	> 11.61	···	···	···	13.47 ⋆	···
5	J085053.12+445122.5	< 11.87	< 11.46	11.65	38	< 12.01	< 49
6	J085215.66+492040.8	< 11.64	< 11.52	11.03	75	< 11.65	< 56
7	J085357.87+463350.6	< 11.64	< 11.45	11.20	63	< 11.69	< 48
8	J101151.95+542942.7	**12.01**	11.93	11.23	83	**12.04**	$148\ ^{+16}_{-23}$
9	J102802.32+592906.6	> 11.04	···	···	···	···	···
10	J105102.77+525049.8	< 11.72	< 11.49	11.32	59	< 11.83	< 53
11	J105404.73+042939.3	> 11.28	···	···	···	···	···
12	J112822.41+482309.9	> 11.98	···	···	···	13.39 ⋆	···
13	J114043.62+532439.0	> 11.77	···	···	···	13.47 ⋆	···
14	J130952.89+011950.6	< 12.03	< 11.56	11.85	33	< 12.24	< 62
15	J140025.53−012957.0	< 11.86	< 11.76	11.17	79	< 11.85	< 98
16	J141946.36+463424.3	11.71	11.56	11.18	70	11.84	63
17	J142649.24+032517.7	< 11.85	< 11.49	11.60	43	< 11.95	< 52
18	J142927.28+523849.5	< 12.07	< 11.48	11.94	25	< 12.27	< 52
19	J161425.17+375210.7	**12.52**	12.28	12.15	57	**12.56**	$326\ ^{+20}_{-19}$
20	J170010.83+395545.8	**12.12**	11.97	11.59	70	**12.06**	$161\ ^{+20}_{-18}$
21	J170341.82+383944.7	< 11.90	< 11.42	11.72	33	< 12.15	< 45
22	J204333.20−001104.2	< 11.84	< 11.40	11.64	36	< 11.92	< 43

Notes: Bold face denotes a **ULIRG**, i.e., $L_{IR} > 10^{12} L_\odot$

⋆ Indicates L_{TIR} estimated from IRAS rather than MIPS fluxes.

Table 2.6: Control sample of non-LoBALs: Infrared luminosities and SFRs.

#	SDSS Object ID	$Log(L_{IR}^{8-1000\mu m})$	$Log(L_{IR}^{SB})$	$Log(L_{IR,8-1000\mu m}^{AGN})$	$\frac{L_{IR}^{SB}}{L_{IR}^{8-1000\mu m}}$	$Log(L_{TIR}^{MIPS})$	SFR_{IR}^{SB}
		$[Log(L_\odot)]$	$[Log(L_\odot)]$	$[Log(L_\odot)]$	[%]	$[Log(L_\odot)]$	$[M_\odot\ \mathrm{yr}^{-1}]$
(1)	(2)	(3)	(4)	(5)	(6)	(7)	(8)
1	J103236.22+580033.9	< 11.47	< 11.20	11.14	53	< 11.69	< 27
2	J103333.92+582818.8	< 11.12	< 11.00	10.49	76	< 11.39	< 17
3	J103651.94+575950.9	11.72	11.55	11.22	68	11.86	61
4	J103721.15+590755.7	< 11.44	< 11.08	11.19	43	< 11.75	< 20
5	J104210.25+594253.5	< 11.39	< 11.10	11.08	50	< 11.68	< 21
6	J104526.73+595422.6	11.81	11.50	11.51	49	12.08	54
7	J104556.84+570747.0	< 11.32	< 10.97	11.06	44	< 11.69	< 16
8	J104625.02+584839.1	< 11.50	< 10.54	11.44	11	< 11.87	< 6
9	J104633.70+571530.4	< 11.67	< 11.25	11.47	37	< 11.85	< 30
10	J104840.28+563635.6	< 11.77	< 11.37	11.55	39	< 12.00	< 40
11	J104857.92+560112.3	**12.01**	11.93	11.20	84	12.07	148
12	J105000.21+581904.2	< 12.09	< 11.36	12.00	18	< 12.36	< 39
13	J105106.12+591625.1	**12.19**	11.96	11.81	58	12.38	158
14	J105518.08+570423.5	< 11.80	< 11.22	11.66	26	< 12.06	< 28
15	J105604.00+581523.4	< 11.98	< 11.26	11.89	19	< 12.31	< 31
16	J105959.93+574848.1	11.72	11.23	11.55	32	11.97	29
17	J160015.68+552259.9	**11.99**	11.70	11.68	51	12.16	86
18	J160128.54+544521.3	**12.54**	12.33	12.13	61	12.67	367
19	J160341.44+541501.5	< 11.37	< 11.18	10.93	63	< 11.53	< 25
20	J160523.10+545613.3	11.69	11.18	11.53	30	11.97	26
21	J160630.60+542007.5	< 12.11	< 11.35	12.02	17	< 12.41	< 38
22	J160908.95+533153.2	< 11.92	< 11.50	11.70	38	< 12.18	< 55
23	J163031.46+410145.6	11.45	11.27	10.98	66	11.60	32
24	J163135.46+405756.4	**11.99**	11.65	11.72	46	12.22	77
25	J163143.76+404735.6	11.65	11.33	11.36	48	11.83	37
26	J163352.34+402115.5	**11.96**	11.75	11.53	62	12.13	98
27	J163502.80+412952.9	< 11.40	< 10.72	11.29	20	< 11.64	< 9
28	J163854.62+415419.5	< 11.70	< 11.12	11.56	26	< 11.98	< 23
29	J171126.94+585544.2	11.85	11.68	11.34	68	12.10	82
30	J171334.02+595028.3	< 11.69	< 10.29	11.67	3	< 12.11	< 3
31	J171736.90+593011.4	11.93	11.61	11.64	48	12.17	71
32	J171748.43+594820.6	**11.97**	11.62	11.71	44	12.12	72
33	J171818.14+584905.2	**11.96**	11.80	11.45	69	12.10	109
34	J172104.75+592451.4	**12.06**	11.92	11.51	71	12.33	144
35	J172414.05+593644.0	< 11.65	< 11.16	11.48	32	< 11.93	< 25

Notes: Bold face denotes a **ULIRG**. Objects with $L_{IR} > 10^{11.95} L_\odot$ were considered.

Table 2.7: SMC-type AGN extinction in V band and silicate strengths.

#	SDSS Object ID	A(V)	$S_{9.7}$
	LoBALs		
1	J023102.49−083141.2	···	···
2	J023153.63−093333.5	···	···
3	J025026.66+000903.4	1.03	0.81
4	J083525.98+435211.2	0.00	···
5	J085053.12+445122.5	0.14	0.34
6	J085215.66+492040.8	0.41	···
7	J085357.87+463350.6	0.53	···
8	J101151.95+542942.7	0.52	···
9	J102802.32+592906.6	0.00	···
10	J105102.77+525049.8	0.50	···
11	J105404.73+042939.3	0.51	···
12	J112822.41+482309.9	0.61	···
13	J114043.62+532439.0	0.00	···
14	J130952.89+011950.6	0.14	0.56
15	J140025.53−012957.0	0.69	···
16	J141946.36+463424.3	0.48	···
17	J142649.24+032517.7	0.44	0.64
18	J142927.28+523849.5	0.28	0.43
19	J161425.17+375210.7	0.10	0.34
20	J170010.83+395545.8	0.42	···
21	J170341.82+383944.7	0.83	0.75
22	J204333.20−001104.2	0.28	···
	Control sample of non-LoBALs		
1	J103236.22+580033.9	0.12	···
2	J103333.92+582818.8	0.21	···
3	J103651.94+575950.9	0.52	···
4	J103721.15+590755.7	0.06	···
5	J104210.25+594253.5	0.00	···
6	J104526.73+595422.6	0.20	···
7	J104556.84+570747.0	0.01	···
8	J104625.02+584839.1	0.03	···
9	J104633.70+571530.4	0.03	···
10	J104840.28+563635.6	0.24	···
11	J104857.92+560112.3	0.05	···
12	J105000.21+581904.2	0.01	···
13	J105106.12+591625.1	0.07	···
14	J105518.08+570423.5	0.00	···
15	J105604.00+581523.4	0.02	···
16	J105959.93+574848.1	0.31	···
17	J160015.68+552259.9	0.14	···
18	J160128.54+544521.3	0.01	···
19	J160341.44+541501.5	0.11	···
20	J160523.10+545613.3	0.05	···
21	J160630.60+542007.5	0.10	···
22	J160908.95+533153.2	0.01	···
23	J163031.46+410145.6	0.03	···
24	J163135.46+405756.4	0.24	···
25	J163143.76+404735.6	0.41	···
26	J163352.34+402115.5	0.00	···
27	J163502.80+412952.9	0.04	···
28	J163854.62+415419.5	0.11	···
29	J171126.94+585544.2	0.15	···
30	J171334.02+595028.3	0.00	···
31	J171736.90+593011.4	0.06	···
32	J171748.43+594820.6	0.00	···
33	J171818.14+584905.2	0.10	···
34	J172104.75+592451.4	0.06	···
35	J172414.05+593644.0	0.23	···

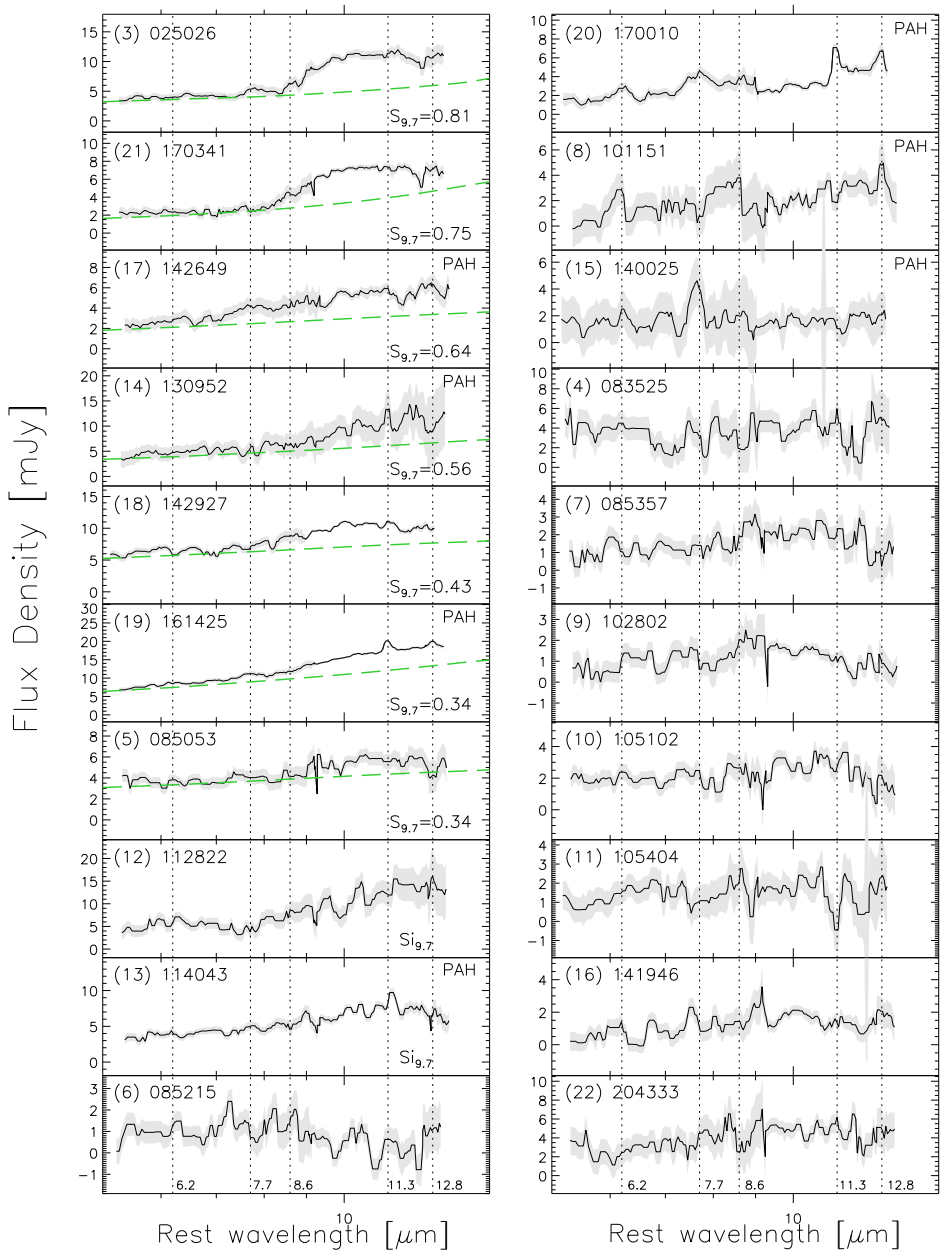

Figure 2.1: Low-resolution IRS spectra of the LoBALs, plotted as flux density in units of mJy vs. rest-frame wavelength in μm. The spectra are in solid black, with 1σ errors in gray. Plotted with a long-dash green line is the spline-interpolated continuum used to estimate the silicate strength. Vertical dotted lines at 6.2, 7.7, 8.6, 11.3, and 12.8 μm indicate the fiducial peaks of prominent PAH features. The objects in the left column show silicate emission at 9.7 μm, listed in order of decreasing strength from top to bottom. Note that 114043 and 085053 show apparent redshifted silicate emission, the strength of which could not be measure because the line is truncated and MIPS photometry was not available to constrain the SED in the FIR. Also note that 085215 shows possible silicate absorption. The top three objects in the right columns show the strongest PAH features. All objects labeled 'PAH' in the top right corner show at least one of the PAH lines. The displayed spectra have been median smoothed with a boxcar of five.

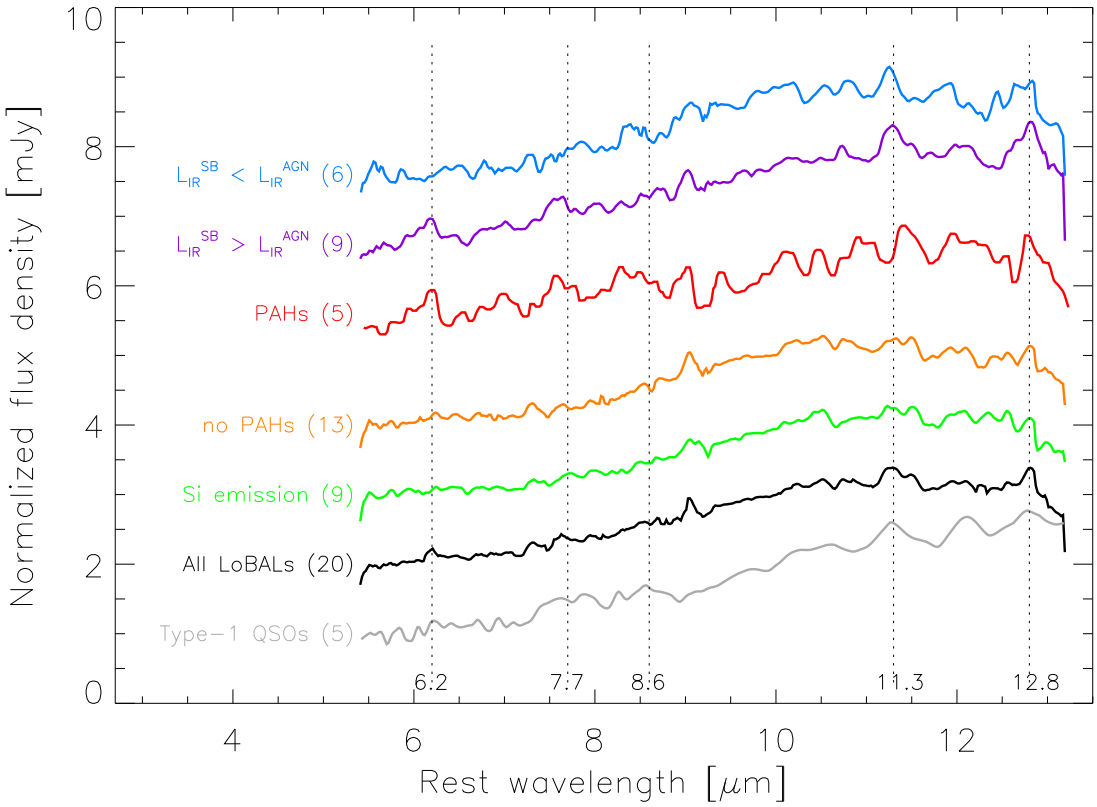

Figure 2.2: Signal-to-noise-weighted average spectra of the LoBALs in our sample, grouped according to shared characteristics. The average spectrum of all LoBALs (**solid black line**) was obtained by averaging the individual spectra after normalizing their flux density by the average flux density from 5−6 μm. With a solid orange line is the average spectrum of the objects which show no or very weak PAH features. In solid red is the average of the LoBALs with PAH features. In solid green we plot the average of the LoBALs with silicate emission at 10 μm. In solid purple is the average of the LoBALs with starburst luminosity higher than the AGN luminosity from 8−1000 μm, while in solid blue with starburst luminosity less than the AGN luminosity. For comparison, in solid gray at the bottom we also plot the average spectrum of the five type-1 QSOs in the Hiner et al. (2009) sample which fall within the redshift range $0.5 < z < 0.63$. Vertical dotted lines at 6.2, 7.7, 8.6, 11.3, and 12.8 μm indicate the position of prominent PAH features. The PAH lines are stronger in the composite of objects with $L_{IR}^{SB} > L_{IR}^{AGN}$ than in the "PAH average," suggesting that the FIR emission, indeed, arises from star formation rather than from a very extended torus, for example.

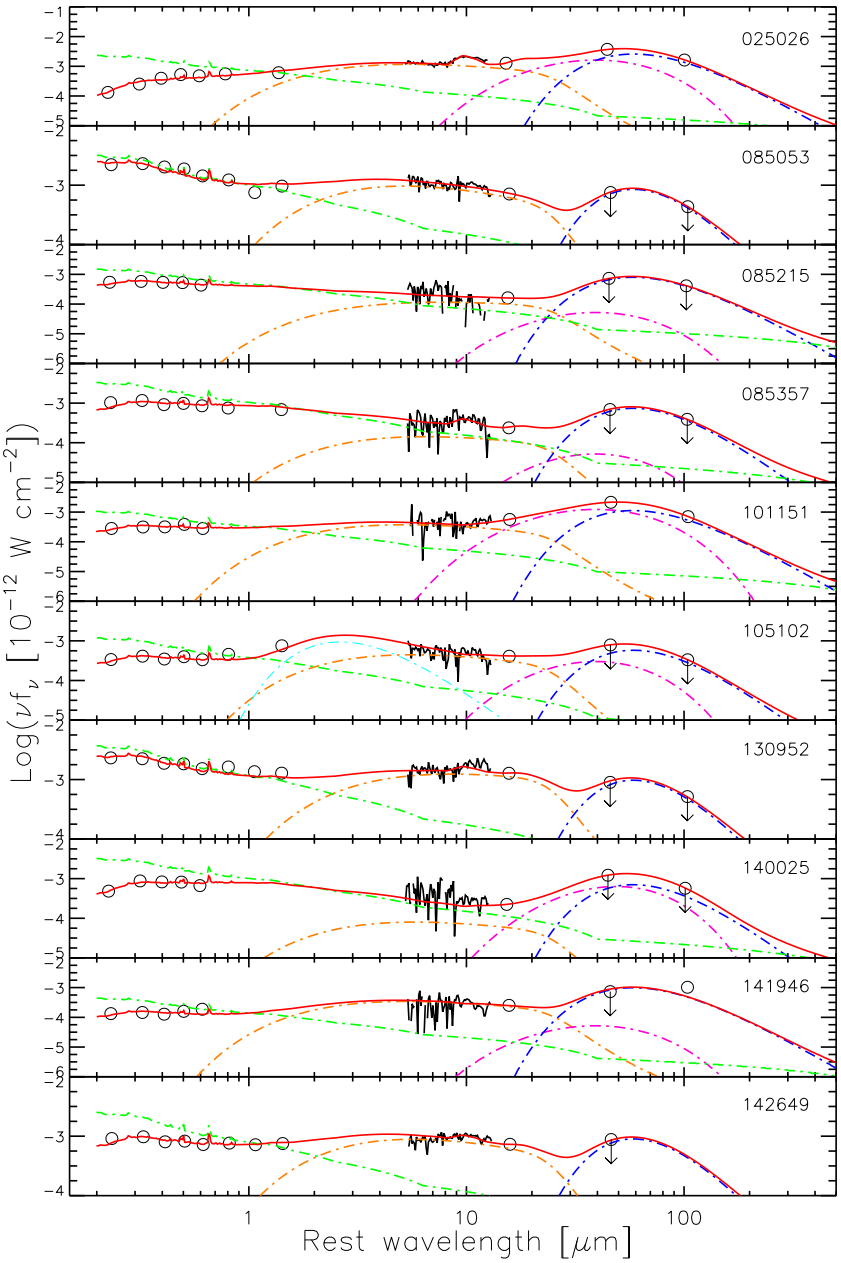

Figure 2.3: Model fits to the SEDs of the 15 LoBALs in the sample with available *Spitzer* IRS and MIPS observations. The solid black lines are the *Spitzer* IRS spectra and the open black circles are SDSS *ugriz* and *Spitzer* MIPS photometry at 24, 70, and 160 μm. The SED model is described in detail in §2.4.2. The overall fit to the SED is plotted with a solid red line. The individual components to the fit are plotted with dot-dash lines, color-coded as follows: unreddened SDSS quasar composite in green; near-IR modified black body at temperature T=1,000 K in cyan; modified mid-IR power-law component in orange; warm small grain dust in magenta; and 45K modified black body component in blue. Down arrows indicate 3σ upper limits. Partial object names are indicated in the upper right corner of each plot.

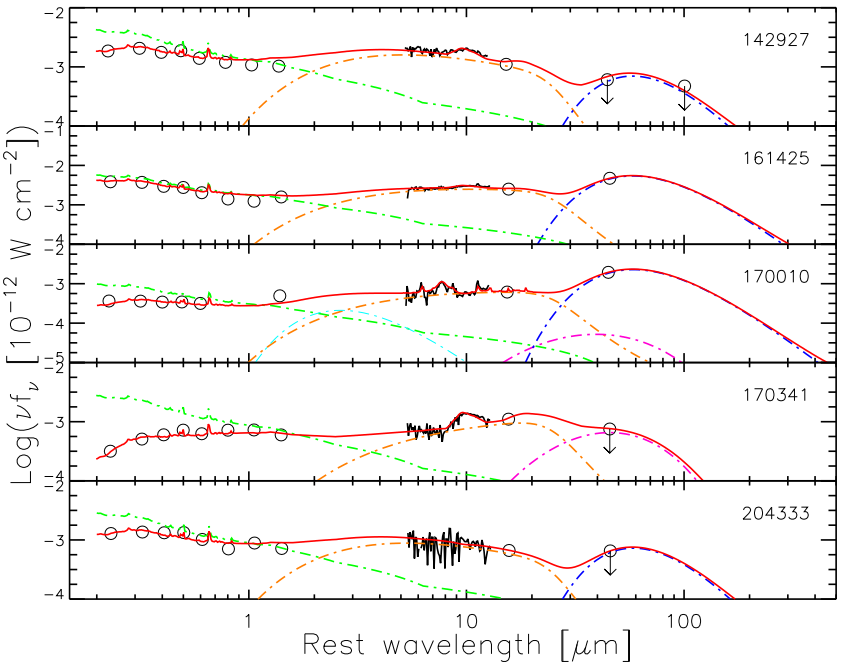

Figure 2.3: Continued.

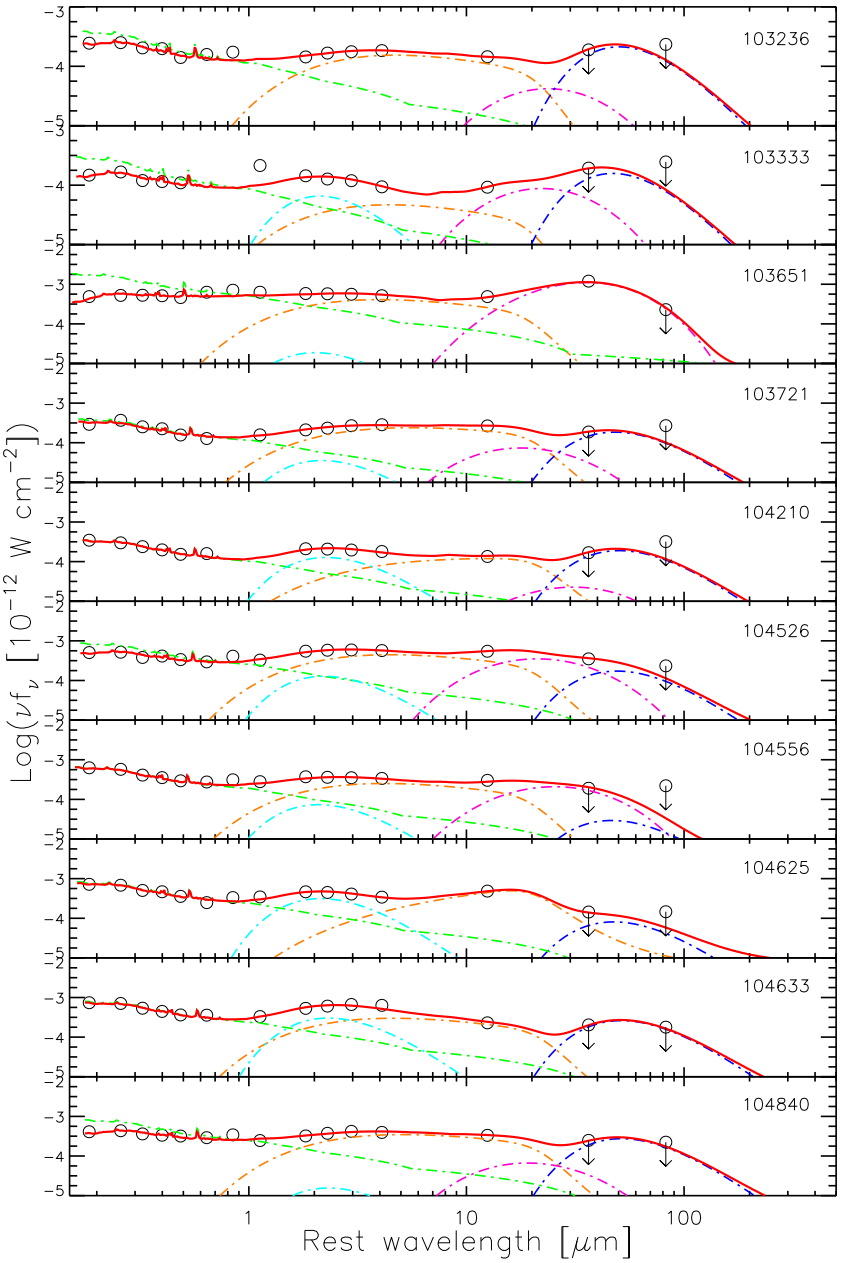

Figure 2.4: SED models of the control sample of 35 non-LoBALs. The solid black lines are the *Spitzer* IRS spectra and the open black circles are SDSS *ugriz*, *Spitzer* IRAC 3.6, 4.5, 5.8, 8.0 μm, and MIPS photometry at 24, 70, and 160 μm. The overall fit to the SED is plotted with a solid red line. The individual components to the fit are plotted with dot-dash lines, color-coded as follows: unreddened SDSS quasar composite in green; near-IR modified black body at temperature T=1,000 K in cyan; modified mid-IR power-law component in orange; warm small grain dust in magenta; and 45K modified black body component in blue. Down arrows indicate 3σ upper limits. Partial object names are indicated in the upper right corner of each plot. with the exception of the additional very hot dust component, plotted as dot-dashed cyan line. The

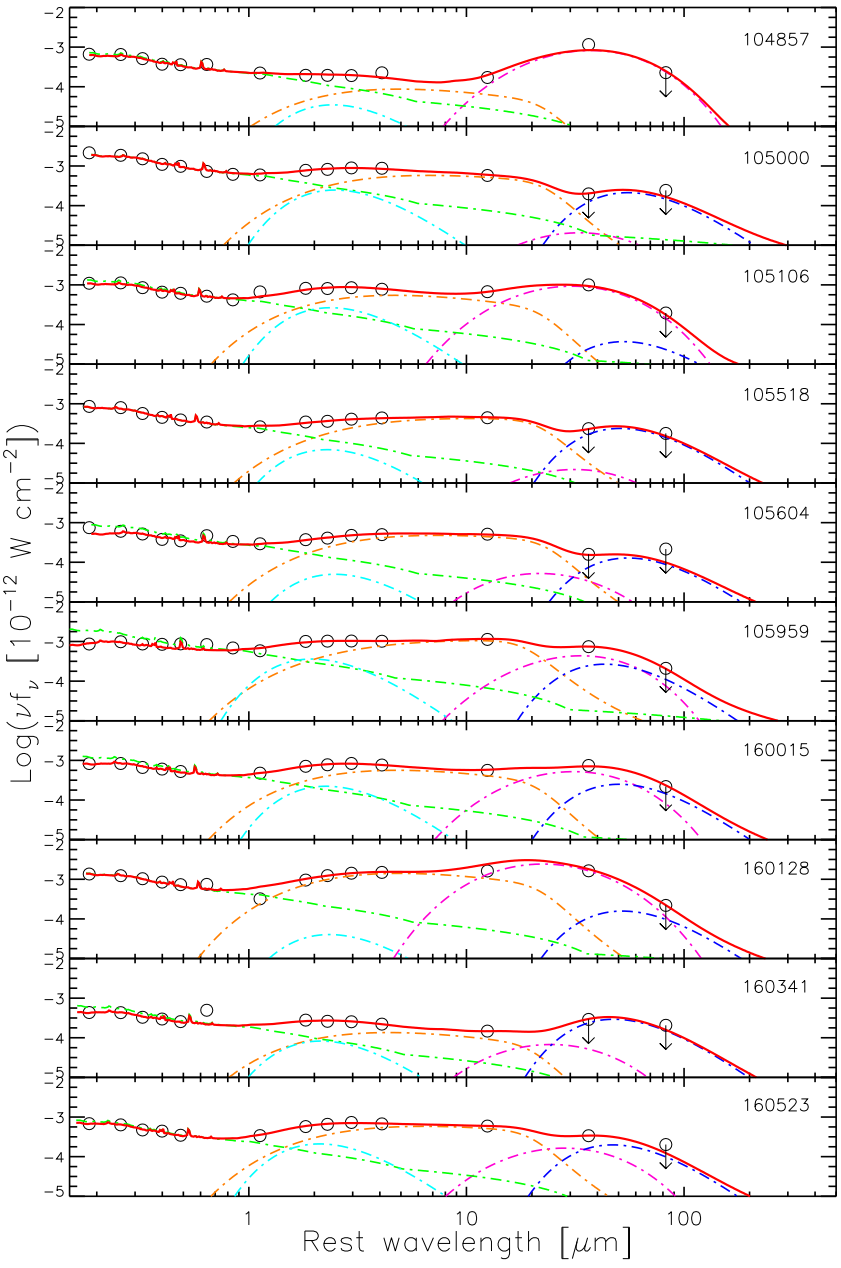

Figure 2.4: Continued.

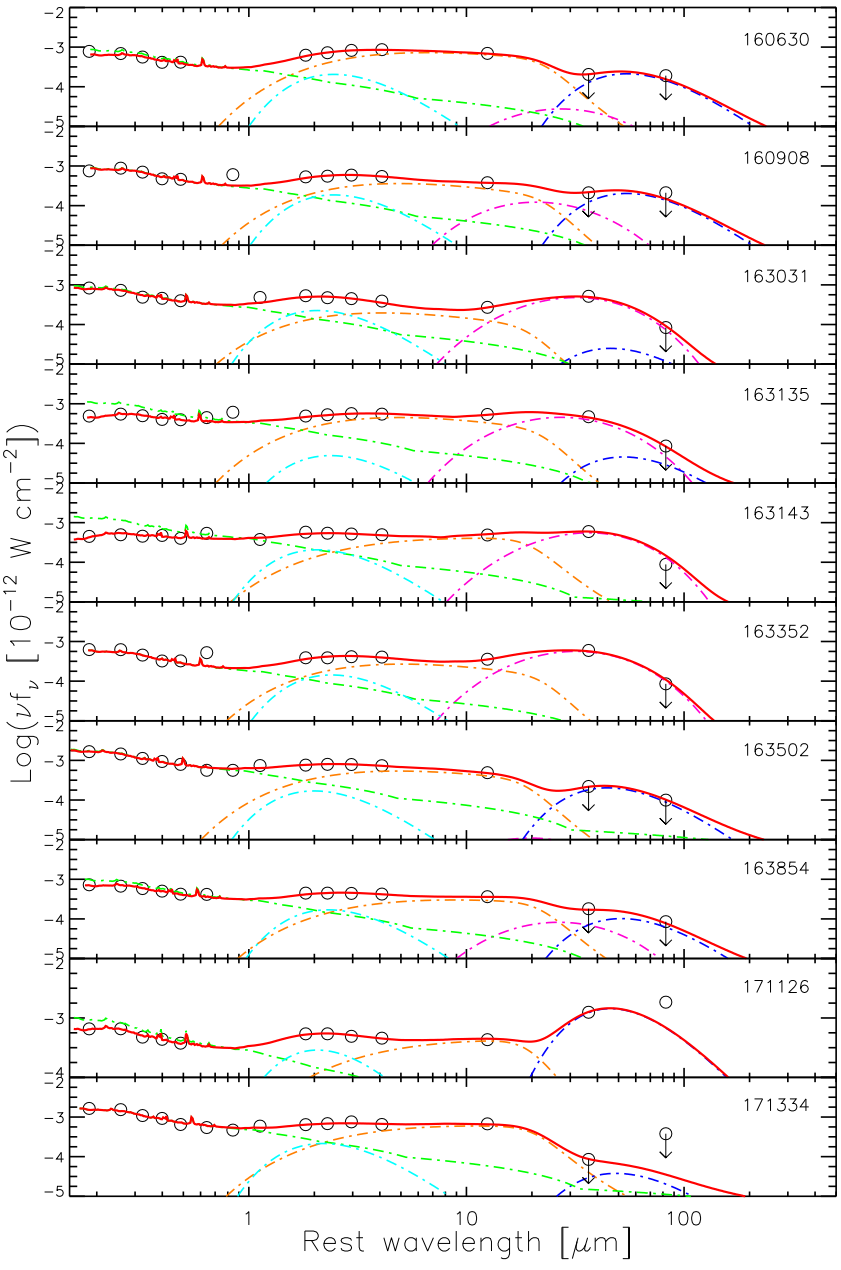

Figure 2.4: Continued.

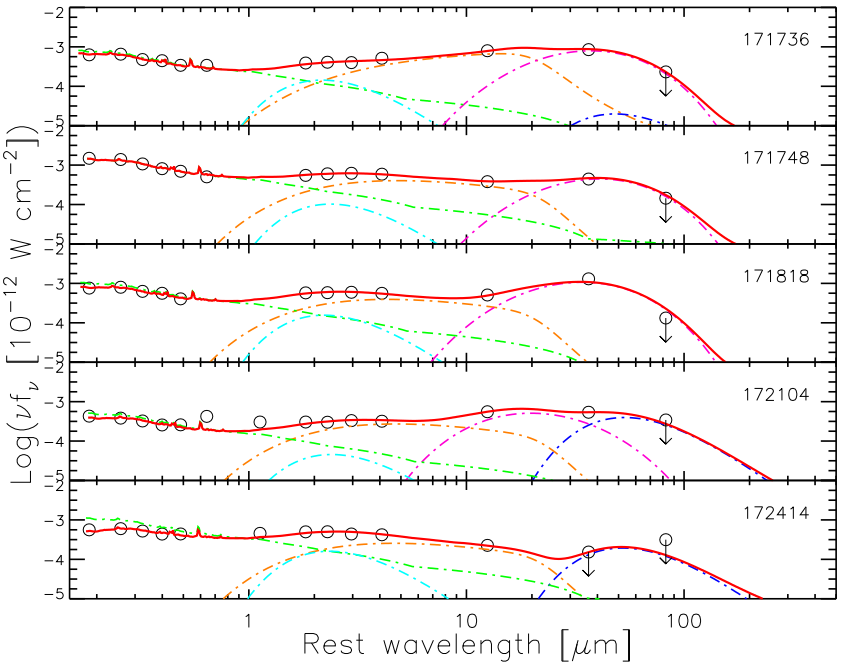

Figure 2.4: Continued.

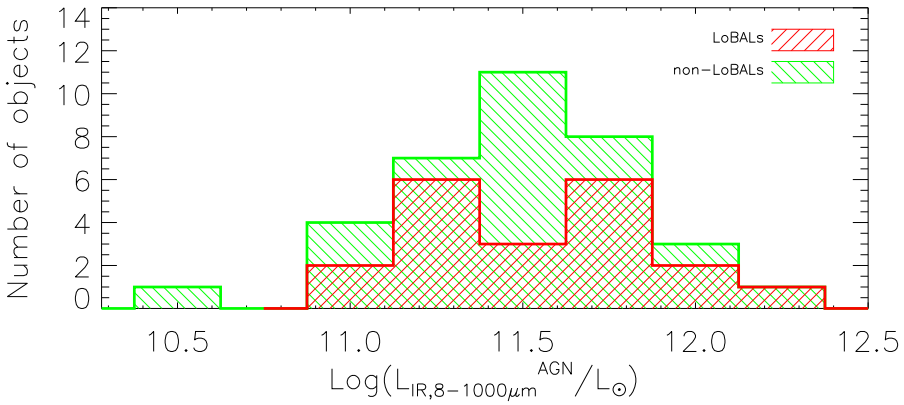

Figure 2.5: LoBALs and non-LoBALs: Distribution of the AGN infrared luminosity integrated from the best-fit SED model between 8− 1000 μm, plotted in bins of 0.25 dex. The medians of 11.61 for the LoBALs and 11.48 for the non-LoBALs show that LoBALs do not harbor intrinsically more infrared-luminous AGN than those in non-LoBALs.

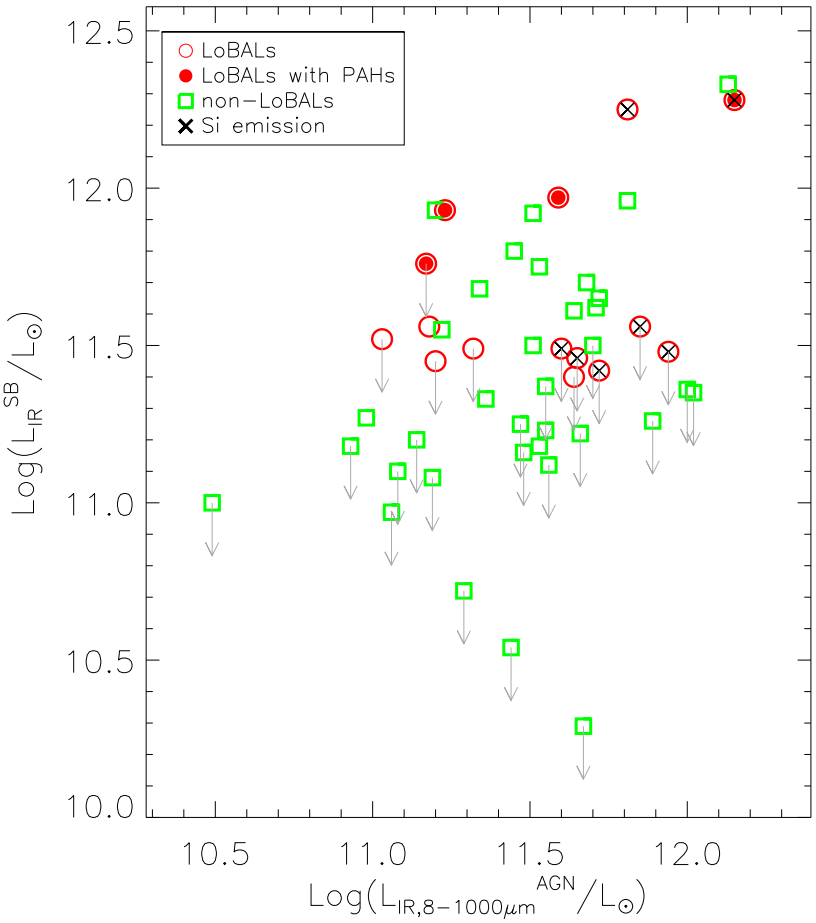

Figure 2.6: Starburst luminosity vs. AGN contribution to the FIR luminosity in LoBALs and in non-LoBAL QSOs, as estimated from the SED models. The data are listed in Table 2.5 and 2.6. LoBALs are plotted with red circles; non-LoBALs are plotted with green squares. Black × denotes a LoBAL with detectable 10 μm silicate emission. Filled red circles indicate the present of PAH emission, while the red open circles are LoBALs without PAH features. The presence, or absence, of silicate emission in LoBALs is correlated with the total AGN FIR luminosity, suggesting that the weak silicate emission we see in LoBALs is directly excited by the central AGN. All LoBALs with $Log(L^{AGN}_{IR,8-1000\mu m}/L_{\odot}) > 11.55$, show silicate emission. Although the more IR-luminous AGN appear to preferentially have silicate emission, this is likely an artifact of the systematically higher S/N of their IRS spectra. PAH emission is favored among LoBALs with starburst luminosities $Log(L^{SB}_{IR}/L_{\odot}) > 11.75$. One exception is SDSS J025053+000903, which has the strongest silicate emission feature in our sample.

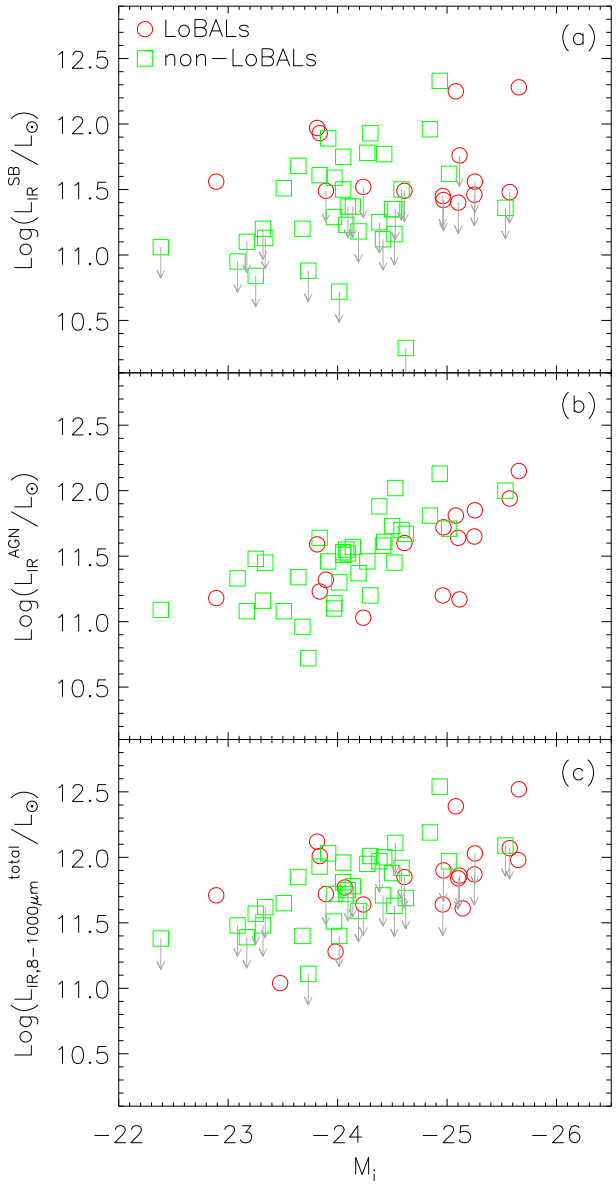

Figure 2.7: Infrared luminosity vs. absolute M_i magnitude corrected for AGN reddening with the extinction estimated from the SED fitting. The LoBALs are plotted with open red circles; the non-LoBALs are shown with open green squares. Down arrows indicate upper limits. The FIR limits for the non-LoBAL QSOs are better constrained due to the lower uncertainties in their MIPS images (i.e., non-LoBALs: $\sigma_{70\mu m} \sim$ 1.6 mJy and $\sigma_{160\mu m} \sim 3.7$ mJy; LoBALs: $\sigma_{70\mu m} \sim 6.2$ mJy and $\sigma_{160\mu m} \sim 8.1$ mJy). (a) Starburst infrared luminosity vs. M_i. (b) AGN infrared luminosity from 8−1000 μm vs. M_i. The apparent correlation implies comparable IR-to-optical ratios, hence, similar cover fractions in LoBALs and in non-LoBALs. (c) Total infrared luminosity from 8−1000 μm vs. M_i.

Chapter 3

Host Galaxy Morphologies with HST/WFC3

ABSTRACT

We present the first high-resolution (FWHM$\lesssim$0.″16) morphological analysis of a volume-limited sample of 22 SDSS-selected Low-ionization Broad Absorption Line QSOs (LoBALs) at $0.5 < z < 0.6$ using observations obtained with the Hubble Space Telescope Wide Field Camera 3 in the IR F125W (observed J) and UVIS F475W (observed SDSS g') channels. The host galaxy is detected in all systems in F125W, which at these redshifts samples the rest-frame optical i-band and is sensitive to old stellar populations. Only 27% of the hosts we detected in F475W, which samples the rest-frame optical u-band and is sensitive to young stellar populations. Signs of recent or ongoing tidal interaction are seen in 59% (possibly 73%) of the host galaxies, including interacting companions, tidal tails, bridges,

asymmetries, plumes, and boxy isophotes. The presence of a second nucleus within $\sim 1''$ (6.4 kpc) is revealed in seven of the systems. A detailed two-dimensional surface brightness analysis with GALFIT indicates that the majority (73%) have prominent early-type (bulge, n>4) morphology and only four systems have exponential disk profiles (n<2). Most of the targets (55%) were best fit by Sersic index $n \gg 4$, indicating presence of extended low-surface brightness emission or PSF mismatch. Two of the disks and one bulge are better described as pseudobulges (n<2.2). A second Sersic component did not provide physically meaningful results for any of the objects and we conclude that is not necessary to describe the light distribution. We divide the LoBALs into subsamples based on interaction stage and morphology. We find that the binary systems (pre-mergers) have smaller Sersic indices, larger effective radii, less luminous QSOs, lower infrared luminosities, lower star formation rates (SFRs), but higher star formation contribution to the total infrared flux than the mergers. SFRs anti-correlate with the maximum Mg II outflow velocity between the mergers and the more advanced mergers suggesting an active role of the outflow in quenching the SFR in the host . The dominance of bulges and unambiguous signs of tidal interaction strongly suggests that the population LoBALs are QSOs that result from major mergers. Nevertheless, this sample of LoBALs represents merger systems at various stages of the interaction process, hence, either the outflows which characterize these systems persist for as long as the interaction signs are observable in the galaxy, or very short-lived outflows are triggered and die out during various stages of the merger process.

3.1 Introduction

Establishing the morphologies of Quasi Stellar Objects (QSO) host galaxies may be key to providing observational justification for a popular model of galaxy formation, which suggests that elliptical galaxies are formed vie mergers of gas-rich disk galaxies (Toomre & Toomre, 1972). The strong merger-induced morphological disturbances in Ultra-luminous Infrared Galaxies (ULIRGs; $L_{IR} > 10^{12} L_{\odot}$) and the intense infrared luminosities of those systems, comparable to the bolometric luminosities of QSOs, suggest that ULIRGs may be dust-enshrouded QSOs triggered by the merger of two gas-rich spiral galaxies (e.g., Sanders et al., 1988).

The morphologies and dynamics of ULIRGs indicate that these galaxies are associated with galaxy mergers (Armus et al., 1987; Sanders et al., 1988; Murphy et al., 1996; Veilleux et al., 2002; Dasyra et al., 2006). Similarly, the host galaxies of QSOs, once thought to be mostly normal, quiescent ellipticals (e.g., Floyd et al., 2004), have recently been shown to have unambiguous relics of past tidal interaction through the presence of faint tidal features in deep HST images (Canalizo2007; Bennert2008). If starbursts, ULIRGs, and QSOs are connected in an evolutionary sequence which was initiated by a galaxy interaction, observations of the transition stages of this process are necessary to better understand this connection (see e.g., Hopkins et al., 2008b). The radiatively-driven winds observed in Broad Absorption Line (BAL) QSOs make them one of the most promising candidates of observing AGN feedback. The kinetic power of the winds is sufficient to unbind large mass of gas on galactic scales (see for review Fabian, 2012). Particularly, low-ionization BALs (LoB-

ALs) are suspected to be young, recently fueled QSOs with disturbed host morphologies (Canalizo & Stockton, 2002).

While at higher redshift the host of AGN seem to show only a small fraction of major mergers and mostly disk morphologies (e.g., Kocevski et al., 2012), suggesting that secular processes, such as bars and disk instabilities, drive the black hole growth at those epochs, at least at the highest AGN luminosities, those of QSOs, major mergers dominate (e.g., Schawinski et al., 2012). The morphologies of QSO hosts at lower redshifts (<0.5) are dominated by bulges and significant fraction of them show complex structure (e.g., McLeod & McLeod, 2001; Hamilton et al., 2002; Dunlop et al., 2003; Veilleux et al., 2009).

In this chapter we present results from the *HST* WFC3/IR and UVIS imaging campaign of the 22 optically selected LoBAL QSOs introduced in Chapter 1. A detailed high-resolution study of their morphologies should reveal unambiguous signs of tidal interaction if LoBALs are indeed transition objects.

Details on the observations and data reduction are explained in § 2. We present the analysis in § 3 and results in § 4. Discussion and conclusions are given in § 5 and § 6. We assume a flat universe cosmology with $H_0 = 71$ km s^{-1} Mpc^{-1}, $\Omega_M = 0.27$, and $\Omega_\Lambda = 0.73$. All luminosities in units of the bolometric solar luminosity were calculated using $L_\odot = 3.839 \times 10^{33}$ erg s^{-1}.

3.2 Observations and Data Reduction

Imaging data were obtained with the Hubble Space telescope using the infrared (IR) and the ultraviolet-visible (UVIS) channels of the Wide Field Camera 3 (WFC3)

between August 6, 2009, and April 29, 2011, as part of our Cycle 17 program GO-11557 (PI: Canalizo). This program was granted 23 orbits to observe the entire sample of 22 LoBALs and a PSF star in the IR channel using the wide J-band F125W filter (λ_{pivot} = 1249 nm; $\Delta\lambda$=302 nm; detector pixel scale $\sim 0\farcs13$ pixel^{-1}) and the UVIS channel using the SDSS-g'-band F475W filter (λ_{pivot} = 478 nm; $\Delta\lambda$=149 nm; detector pixel scale $\sim 0\farcs04$ pixel^{-1}). One full orbit was used to acquire both the IR and UVIS observations for each target. An additional orbit was granted to repeat and replace the observations for one of the targets, as guide-star acquisition failure caused drift and inaccurate pointing in the initial F475W observations for that one object. The WFC3/IR observations were obtained in the MULTIACCUM mode, with sampling sequence SPARS50 and NSAMP of 10, 11, or 12. The WFC3/UVIS observations were obtained in the ACCUM mode, and whenever time allocation allowed, we used a CR-SPLIT. A two-point dither pattern, with a spacing of $0\farcs636$ for the IR and $0\farcs145$ for the UVIS, was used to ensure better sampling of the PSF and to help with the removal of data artifacts, such as cosmic rays and hot and dead pixels. The resulting total exposure times for each object ranged within 806-1006 s for the IR and 1436-1748 s for the UVIS exposures; the exposure times for each object are listed in Table 1.

Starting with the bias-subtracted and flat-field corrected data products from the HST pipeline (i.e., the flt.fits files), the data were further processed with the Multidrizzle software package (Koekemoer et al. 2002) to clean the cosmic rays, apply the geometric corrections using the latest calibration files, and combine the individual dithered exposures. The images were drizzled to pixel scale of $0\farcs035$ pixel^{-1} for the UVIS/F475W and $0\farcs07$

pixel^{-1} for the IR/F125W using a pixel droplet fraction (pixfrac) of 1.0. The sky pedestal was not subtracted for the images to be analyzed with GALFIT.

The final spatial resolution of the images in F125W is PSF FWHM = $0\farcs16$ (1.0 kpc for median z = 0.55 at 6.4 kpc/$''$) and in F475W PSF FWHM = $0\farcs12$ (0.77 kpc for z=0.55).

3.3 Analysis

The two-dimensional image-fitting program GALFIT (Peng et al., 2002, 2010) was used for each object to model the central point source and the surface brightness profile of the host galaxy. GALFIT is a least-squares, χ^2, minimization algorithm which fits any number of light profiles to an input image, allowing for decomposition of the different contributions. In our investigation of LoBALs, we are interested in determining whether these galaxies have been involved in tidal interaction. Hence, we are not aiming in deriving models that fit every surface brightness feature, producing residuals close to the noise level. But rather, our goal is to fit classical physically meaningful galaxy components, such as a disk and/or a bulge, and use the residuals as a telltale for the past interaction history of the host galaxy.

Hence, we fit the LoBALs with a PSF component, to account for the bright QSO point source, and one or two Sersic profiles convolved with the PSF. The radial surface brightness Sersic profile, one of the the most used functions to study galaxy morphology, has the form:

$$\Sigma(r) = \Sigma_e \exp\left[-\kappa\left(\left(\frac{r}{r_e}\right)^{1/n} - 1 \right)\right],$$

where Σ_e is the pixel surface brightness at the effective radius r_e, r_e is the radius such that half of the total flux is within r_e, n is the concentration parameter, more commonly knows as the Sersic index, and κ is a variable coupled to n. When n is large, the central profile is steeper and the wings are extended. When n is small, the central peak is flatter and the profile is truncated sharply at smaller radii. A special case of the Sersic profile when n = 4 is the de Vaucouleurs profile, which describes galaxy bulges. Another special case when n = 1 is the exponential profile, which describes galaxy disks.

We proceeded to fit the surface brightness distribution of each object with three one-Sersic component models and two two-Sersic component models. Bright sources and faint extended structure within the image frames were masked out. The sky level was estimated separately using *IRAF* and was held fixed in the GALFIT modeling as it is known that the sky anti-correlates with the Sersic index (Peng et al., 2010). The PSF and Sersic component centroids were allowed to vary.

3.3.1 One-Sersic Component Models

First, we fit the surface brightness distribution of each LoBAL with single Sersic component and a PSF component to simulate the host galaxy and the unresolved QSO emission. The Sersic component is convolved with the PSF.

Three one-Sersic component models were fit to the data: a Sersic profile with unconstrained Sersic index (n = free), a de Vaucouleurs profile (fixed n = 4), and an

exponential disk profile (fixed n = 1). In all cases, the centroids, the effective radius (r_e), the axis ratio (b/a), the position angle (PA), and the magnitude were left unconstrained. Our initial visual assessment of the images determined that most of the systems have couple morphology that would not be well fit by classical bulge or disk models. However, this simple one galaxy model analysis allows us to determine whether the system is bulge- or disk-dominated. It also allows us to get an insight of the morphological disturbance, if any, from the residual maps produced by subtracting the model from the data.

3.3.2 Two-Sersic Component Models

Any significant remaining residuals from the one-Sersic component models may be merger-induced morphological anomalies, or may, in principle, indicate the presence of a second low-surface brightness galaxy component. To account for the possibility of a second component, in addition to the one -Sersic models, we fit each object with two two-Sersic component models and a PSF: one that included the classical disk and bulge profile (n=1 + n=4), and another one in which both Sersic indices were left unconstrained (n-free + n-free). The centroids, r_e, b/a, PA, and magnitude were left unconstrained. In many of the cases, the χ^2 statistics indicated a better fit, which is not surprising given the large number of free parameters. However, a close examination of the models revealed that at least one of the fitted components was not physically meaningful. Whenever the model parameter converged to extreme value, the models were considered unphysical. For instance, a very large Sersic index, producing a profile with very steep core and extended wings, compensates for a mismatch between the PSF model and the nucleus emission, extended faint surface

brightness, or sky mismatch. Very large effective radius attempts to fit extended low-brightness structure or indicates a mismatch with the sky value. Upon close inspection, none of the second Sersic components we deemed physical and we conclude that the quality of the data does not allow us to determine whether a second very low surface brightness or very compact component is present. The results of the surface brightness modeling discussion only the one-Sersic component model.

3.3.3 Binary Systems

Six of the LoBALs are binary systems. Although we do not present spectroscopy that confirms that the companion galaxy are at the same redshift, signs of tidal interaction suggest that these may be interacting companions. The companions to J1011+5429, J1054+0429, and J1419+4634 were apparently present in the images even before the surface brightness fitting. The faint companions to J0231-08,31, J0852+4920, and J1426+0325 became apparent only after subtracting the GALFIT models. These companions we modeled with a separate Sersic componenent added to the one-Sersic component models only for J1011+5429 and J1054+0429 because no reliable solutions were derived for the other four binary systems. For J1011+5429, the Sersic index was fixed at n = 4 and two of the solutions show unrealistic parameters. For J1054+0429 the companion Sersic index was allowed to vary and all of the three cases (i.e., n=1, n=4, and n=free) converged to effective radii below the spatial resolution. Nevertheless, subtracting those companions allow us to show better some of the faint residual structure.

3.4 Results

The model parameters from the GALFIT analysis of the F475W and F125W images are listed in Tables 3.2 and 3.3, respectively, and presented visually in Figures 3.2 through 3.23, one figure for each individual object. In the Figures, we show the data F475W and F125W images (top row), the residuals after subtracting the GALFIT models (middle row), and radial surface brightness profiles of the data and of each component in the model, constructed with the *IRAF* task *ellipse* (bottom row). The task *ellipse* performs ellipse fitting in 2D and averages the profiles to 1D. The residual images show how well the light profiles are fit by classical disk and bulge galaxy profiles.The radial intensity profiles give an idea of the relative contribution of each component as a function of radius from the center.

The high spatial resolution of *HST* images (FWHM$\lesssim$0.16) reveals the presence of a previously unknown close source ($\lesssim 1''$) to the cores of six of the LoBALs in our sample: (1) J0231-0831, (6) J0852+4920, (08) J1011+5429, (11) J1054+0429, (16) J1419+4634, and (17) J1426+0325. In this work we do not present spectroscopic data to establish whether or not these companions are associated with the QSOs, however, we have obtained Keck/LRIS and ESI spectroscopy of these targets, which will be analyzed in the near future. The disturbed morphologies of these systems rule out the possibility of these companion sources being a chance alignment foreground or background objects and suggest that they are part of a tidally interacting binary system. In addition, the F475W image of (20) J1700+3955 reveals a possible companion, or a large clump, located $\lesssim 1''$E from the core. Although appearing as a large spiral galaxy, this system is not very well fit by a disk profile. A very faint extension of one the spiral arms to the West resembles a tidal tail. In the previous

Section 3.3.3 we explained how we dealt with the companion source in the fitting. Only two of the companions were modeled with an n = free Sersic component and the model parameters are listed in Table 3.3.

The best-fitting model for each object was determined based on the reduced χ^2 values and by inspecting the residuals. Although most of the reduced χ^2 values are close to unity in most case, which indicates a good fit, the significant residuals in some case warn us that these χ^2 values are not to be trusted as an absolute measure of the goodness of the fit. A small value of χ^2 can be due to underestimating the errors, for instance. GALFIT estimate a sigma image based on Poison statistics and, if the sigmas at each pixel are not dominated by shot noise, then the derived reduced χ^2 should not be used as an absolute measure. However, comparing χ^2 value can be useful in discriminating the quality of different models for the same object. We also note that some of the χ^2 values for the F475W models are extremely high, but we note that some of the images for which oily two separate exposures were obtained could not be cleaned of cosmic rays very well; Nevertheless, the residuals for those cases are minimal, so conclude that the models fit the image region of our target object well regardless of the χ^2 values.

The F475W images were modeled only with a combination of a PSF and one Sersic component, with an unconstrained Sersic index (n = free). For 16 of the targets, this approach resulted in unphysical parameters for the host component of the model (i.e., extremely small or large r_e, and/or high n), which was an indication that a Sersic component was not needed. These 16 (73%) targets we modeled solely with a PSF + sky components. The minimal resulting residuals from the PSF subtractions show that a host was

not detected. Either the host emission at these bluer wavelengths is very compact or longer exposure times are necessary to detect the host light. Six (27%) of the targets were fit with a PSF + host component. Five of the six were best fit by a disk profile (n<2) and one by a bulge (object (8), n=3.85). Since the majority of the host galaxies were not detected in F475W, any further discussion of the hosts in this section refers to the F125W results.

3.4.1 Morphological Class

The morphological classification is based on the WFC3/IR F125W images, results for which are listed in Table 3.3. Postage stamp image of the targets are show in Figure 3.1 and the classification is summarized in Table 3.4. For each object, we make a bimodal choice between early-type (i.e., exponential disk, n = 1) and late-type (i.e., bulge, n = 4) morphology based on the Sersic index of the best-fitting model. For all objects, the best-fitting model was the n = free model. We adopt a limiting Sersic index of n = 2, hence, systems with n $<$ 2 were considered disk-dominated and systems with n $>$ 2 were considered bulge-dominated. We note that 12 (55%) of the LoBALs have best-fitting models with n $\gg$ 4. This indicates a very strong core emission and a possible PSF mismatch or low surface brightness structure attempted to be fit by the extended wings of the high-n profiles. Any model with n $\gg$ 4 was considered a bulge.

Object (14) J1309+0119 present one exception to this classification scheme in that the lowest reduced χ^2 is for the n = 1.8 model, which would classify it as a disk; however, the residuals of the n = 4 model are significantly less, so we consider it a bulge. In fact, studies have shown that the population of objects called "bulges" consist of two types of

objects (i.e., Fisher & Drory, 2008): classical bulges found in red sequence galaxies and pseudobulges found in blue sequence galaxies. Pseudobulges share characteristics with the disk component of the galaxy, such as near-IR colors, and their radii are coupled to the size of the disks, while classical bulges do not show that. Pseudobulges are easily distinguished from classical bulges (n = 4) by their lower Sersic indices (n < 2.2). If we have adopted a morphological classification that distinguishes between bulges and pseudobulges, objects (3) J0250+0009, (9) J1028+5929, and (14) J1309+0119 would be classified as pseudobulges.

In Table 3.4 we summarize the morphologies. A dominant bulge component was found in the majority of the LoBALs (16/22; 73%). An exponential disk profile provided the best fit to the surface brightness of four (18%) objects: (3) J0250+0009, (6) J0852+4920, (15) J1400-0129, and (20) J1700+3955. Two object, (4) and (5), have unresolved hosts (r_e < 2.27 pixels, the FWHM of the PSF). We conclude that LoBALs are dominated by early-type morphologies. Of the four late-type systems, only one, object (15), shows the typical residuals of disk galaxies, i.e., spiral arms. The other three are atypical disks in that: object (3) shows the most extended tidal tails and its Sersic index would classify it as a pseudobulge; object (6) has a close, possibly interacting, companion and the χ^2 values of the n = free, n = 4, and n = 1 model fits are identical; object (20) shows a large clump close to its central source, which may be a second faint nucleus. We also note that 55% (12/22) of the objects have n>4, which may indicate merger-induced disturbances because the high-n profiles may attempt to fit low surface brightness extended emission. This suggestion if further validated by the presence of unambiguous signs of tidal interaction in most of the systems.

3.4.2 Interaction Class

Unambiguous signs of tidal interaction, such as double nuclei, tidal tails, bridges, shell-like structure, boxy and asymmetric isophotes are visible in 59% (13/22) of the LoBALs. Two of the systems have unresolved hosts and the other seven of the LoBALs show no unmistakable signs of interaction. Much deeper images of the latter nine objects may be able to detect very faint tidal features relic of an old merger event, but such were not detected in the observations presented here. We note that three of the systems not showing clear tidal features have boxy or irregularly-shaped isophotes, show significant residuals, and/or are best described by pseudobulge light distribution. If we consider those characteristics as signs of old interaction, then the fraction of objects that have experienced or are currently undergoing a merger is as high as 73% (16/22).

Qualitatively, we classify the observed interaction stages based on more rigorous classification used by Veilleux et al. (2002) to characterize interactions in ULIRGs. The interaction class noted in Table 3.4 was determined using the following rubric:

- *Mergers* are systems which show signs of tidal interaction.
- *Non-mergers* are considered systems that show no unmistakable signs of tidal interaction. However, the irregularly-shaped isophotes or peculiar morphologies (i.e., significant residuals) may be due to past interaction. With the exception of one disk, those objects are best fit with bulge-like surface brightness profiles. It is certainly possible that those are much older merger remnants. Also, all but one of the non-mergers have sources within a projected distance of 80 kpc, which may, in principle,

be interacting companions. The one exception is object (15). None of the possible companions are spectroscopically confirmed.

According to this classification, the sample of LoBALs consist of 13 (59%) mergers and nine (41%) non-mergers (see Figure 3.24(a)). Interestingly, although the majority of the objects show signs of interaction, the sample as whole represent objects at different stages of the merger process.

3.4.3 Nuclear emission

Ideally, the sample of LoBALs presented here would be compared to a well-matched sample of unobscured type-1 QSO of comparable luminosities and redshift, with available data of similar quality. However, at the present time, we have not carried out the analysis of such a control sample. Instead, we subdivide the LoBAL sample into subsample based in morphology (disks vs. bulges) and interaction stages (mergers vs. non-mergers), and look for trends in the parameters derived from this study and the investigation of their infrared luminosities, star formation rates, and mid-infrared spectral properties. Average and median quantities of various parameters are shown in Figures 3.24 and 3.25.

The QSO emission is modeled with the inclusion of a PSF component to the model. To quantify the strength of the unresolved point source emission, we calculate the flux ratio of the PSF to the host component, I_{QSO}/I_{HOST} (Table 3.5). We find a range of I_{QSO}/I_{HOST} ratios, from 0.15-5.0, with 59% (13/22) of the targets have host galaxies brighter than their QSO (i.e., $I_{QSO}/I_{HOST} < 1$). One target, object (18), has unusually high $I_{QSO}/I_{HOST} = 167$ and was excluded from the plots and the statistics in consideration

of reasonable scale and describing the majority of the population. In Figure 3.24(f) we show I_{QSO}/I_{HOST} as a function interaction class and in Figure 3.26 as function of the MIPS 24 to 70 μm flux ratio. Most of the objects have $f_{24}/f_{70} < 0.3$ and $I_{QSO}/I_{HOST} < 1.5$, but the FIR fluxes are dominated by upper limits, indicated by arrows. Veilleux et al. (2006) notes that the ratio I_{QSO}/I_{HOST} increases as the various AGN in their sample become more AGN-like (i.e., as the f_{24}/f_{70} increases because the AGN contributes more flux to the mid-infrared 24 μm band). Similar trend is present in our sample, as well, however, we note that the the four disks (objects (3), (6), (15), and (20)) have some the of the lowest FIR color, f_{24}/f_{70} <0.15 and nevertheless also have some of the the strongest nuclear emission normalized to the host light. In Figure 3.27, the PSF to host intensity ratio is show as a function of the total infrared luminosity, star formation rate, and maximum velocity of the Mg II broad absorption line. While there is no notable trend with outflow velocity, we note that the FIR-detected objects have I_{QSO}/I_{HOST} close to unity or less, and that ratio increases with increasing L_{IR} and SFRs. There is no significant difference among the objects grouped according to interaction class while the disks show higher I_{QSO}/I_{HOST} than the bulges (Figure 3.24(f)).

3.4.4 Host Sizes and Magnitudes

Figure 3.24(c), (d), and (e) shows the effective radius, QSO, and host absolute F125W magnitudes (listed in Table 3.5), grouped according to interaction stage and morphology. While the luminosities of the hosts and the QSO are comparable, the bulges and the non-mergers show more compact surface brightness profiles. Disks have much larger

effective radii of 5.5 (5.8) kpc versus the 4.0 (3.5) kpc found in bulges, which may be a due the steeper core of the higher Sersic index profiles.

In Figure 3.30 we plot the LoBAL bulges on one of the projections of the fundamental plane obeyed by elliptical galaxies. We find that the elliptical hosts of LoBALs following the same Kormendy relation as the gas-rich merger hosts of PG QSOs and ULIRGs from the QUEST survey (Veilleux et al., 2006, 2009), which is steeper, but in agreement with, the relation for local elliptical galaxies (Pahre, 1999). The radio-quiet (RQ) subsample (LoBALs are mostly RQ, so, to avoid biases, we only compare them to other RQ QSOs) of massive elliptical QSO hosts from the Dunlop et al. (2003) study are also in agreement with the range of galaxy scalelengths we find in LoBALs, although their entire sample dominates the larger ellipticals region, $r_e \sim 10$ kpc.

3.5 Discussion

3.5.1 The Hosts Not Seen in F475W

It is important to keep in mind what are the observations in each band sensitive to. The observations in F475W cover rest-frame ∼2700 Åto ∼3600 Å. This region is very sensitive to the age of the stellar populations, with young populations being significantly brighter than old populations. Balmer emission lines and [O II] λ3727 will be excluded from this region even for the highest z objects in our sample. Normally, one would have to worry about Mg II λ2800 being included in this region. However, since these objects are LoBALs, the nuclear Mg II emission is much less intense than in normal QSOs since much of the

emission his absorbed. Not detecting the majority (73%) of the host galaxies in F475W indicates that there are not many O and B star (lifetimes 1-200 Myr), i.e., no current star formation. Alternatively, any current star formation may be occurring in a very compact region close to the nucleus and appear as part of the unresolved central source. With the spatial resolution at F475W of $0\farcs12$, for nuclear star formation to remain unresolved, it needs to be within the central 0.77 kpc. For three of the six detected host galaxies we have estimate SFR from Spitzer of 150-300 M yr^{-1}. Exception to this is object (19) which show no host galaxy but has an estimated SFR $\sim$ 300 M yr^{-1}. It is also possible that the nuclear emission at these much shorter wavelengths swamps a much fainter host galaxy emission. Alternatively, it is possible that the host galaxies suffer from extreme dust extinction.

3.5.2 F125W and Tidal Tails

The observations in F125W cover rest-frame $\sim$6900 to $\sim$9300Å, a region dominated by the continuum from older stellar populations. This region excludes Hα from even our highest z targets. Since the QSO power-law emission contributes significantly less to this bandpass, these observations were able to detect tidal features. Particularly interesting are the long low surface brightness tidal tails seen in nine of the objects (summary in Table 3.4) because those can be used as a timer for the merger event. In six of the cases, the tails extend for more than $6''$ ($\sim$38 kpc). Tidal tails form from the spiral arms of disk galaxies. Assuming that the tail material travel at the typical rotation speed of 240 km s^{-1}, the dynamical time for the formation of such tails would be on the order of 150 Myr.

The tails can also be used to predict some characteristics of the progenitor galaxies. In most of the cases only one extended tidal tail is visible, which is either a projection effect (when our line of sight is along one of the tails), or it can be a result of a spiral-elliptical merger, or a merger of counterrotating disk galaxies during which one of the disks can remain fairly undisturbed (i.e., Hibbard & Yun, 1999). Object (3) J0250+0009 is the most spectacular merger with two long filamentary tidal tail extending in opposite directions. Its north-west tail bifurcates closer to the central galaxy. The extended tail geometry suggest that this is a prograde major merger of two disk galaxies, i.e., the disk spin axis were aligned with the orbital axis of the merger system. The nearly-circular arches we see in object (1) J0231-0831 resemble an object with bipolarly extending tidal tails viewed in projection close to an axis defined by stretch of the tails. The spiral arm-like structures seem in object (20) are most likely very large and bright tidal tails. This becomes more apparent in the residual images and supported by the presence of possible second nucleus.

3.5.3 Trends with Infrared luminosities, SFR, Outflow Velocities

The apparent signs of tidal interaction and early-type morphologies suggest that the majority of these LoBALs have experienced a recent merger. Simulation between gas-rich galaxies predict that major mergers (mass ratios >3:1) trigger intense bursts of star formation in the host galaxy due to the increased density of cold gas, supply gas to the central regions that can fuel the black hole accretion, and transform the galaxy morphologies from disks to bulges (e.g., Hopkins et al., 2006).

If the relics of the merger events we see in these LoBALs have triggered a starburst, something has already quenched the star formation in these systems to levels we found typical of unobscured type-1 QSOs of comparable optical luminosities. We see a marginal trend with SF activity among the interaction and morphology classes.

The average SFR in the non-mergers (63 $M_{\odot}$) is less than that in mergers (125 $M_{\odot}$), a trend which anti-correlated with the increase of the average maximum velocity of the Mg II broad absorption line (V_{max}^{merger} ~4800 km s^{-1}; $V_{max}^{non-merger}$ ~9100 km s^{-1}; Figures 3.25(d) and (a)). At the same time, the average SFR and maximum outflow velocity in the disks (156 $M_{\odot}$; 10100 km s^{-1}) are higher than in the bulges (89 $M_{\odot}$; 4400 km s^{-1}).

We also find that the average extinction of the QSO, estimated from the SED fitting assuming SMC-like extinction law, and the strength of the silicate dust emission feature at 9.7 μm (Figures 3.25(e) and (f)) follow the trend with SFR: mergers (A_V^{QSO} ~0.5 mag; $S_{9.7} \sim 0.6$) and disks (A_V^{QSO} ~0.6 mag; $S_{9.7} \sim 0.8$) have higher QSO extinction and stronger silicate emission than the the non-mergers (A_V^{QSO} ~0.2 mag; $S_{9.7} \sim 0.4$) and bulges (A_V^{QSO} ~0.4 mag; $S_{9.7} \sim 0.5$). This suggest that quenching of the star formation may be link to decrease in obscuration, which would be the case if the reservoir of cold gas was cleared by outflows that also cleared up the material providing the obscuration.

3.5.4 Black Hole Activity

The black hole accretion is predicted to experience a 1 Gyr delay from the initial encounter of the merging galaxies. The peak of black hole growth, i.e., when the QSO emits at close to its Eddington limit, is reached at the coalescence of the two merging nuclei. A

short-lived blowout phase characterized by extreme velocity outflows, such as those observed in LoBAL and other BAL QSOs, is predicted to occur after the coalescence. If LoBALs represent QSOs caught in this transient outflow stage, then finding 32% (seven) systems with double nuclei questions that prediction of the models. We proceed to check if LoBALs are QSO emitting at the Eddington limit.

Figure 3.28 (b) show the average and median black hole masses of the LoBALs grouped by interaction and morphology. We estimate the black hole masses from the SDSS spectra using the latest calibration of the single epoch virial black hole mass relation by Park et al. (2012). Assuming that the broad line region (BLR) clouds are virialized, the black hole mass can be estimated as $M_{BH} = R_{BLR}v^2G^{-1}$. The 5100Å continuum luminosity is calibrated via the reverberations mapping technique to give an estimate of the size of the broad line region, R_{BLR}, and the FWHM of the broad H_β line gives an estimate of the velocity of the clouds, v, around the black hole. We note that this single epoch black hole estimate is calibrated with the reverberation mapping technique for lower-luminosity AGN, i.e. Seyfert galaxies with black holes $<10^8$ $M_\odot$, and it is not clear it this relationship holds for higher luminosity AGN, such as QSOs. In addition, the presence of extreme outflows in LoBALs questions whether the virial assumption is applicable to LoBALs since the location of the outflow is not known and, if outflows are present in the broad line region, that would broaden the lines (if seen in emission and M_{BH} will be an overestimate) or absorb the line wing (if seen in absorption and M_{BH} will be an underestimate). In fact, broad blueshifted absorption lines have been observed in BAL QSOs (e.g., Hall, 2007; Ji et al., 2012). Yet another concern is that in many of the systems here the host galaxy contributes significant

fraction of the flux in the optical, so the 5100Å continuum needs to be corrected for host galaxy light. Hence, these masses are not to be used in absolute sense and compared to other studies until these concerns are addresses. Nevertheless, they can be used for comparison among the interaction classes since the average I_{QSO}/I_{HOST} in F125W for mergers and non-mergers are comparable (Figure 3.24(f)). We find that the (average/median) central black holes of the mergers (M_{BH} $\sim$2.7/1.9 $\times 10^8$ $M_\odot$) are about half as massive as those of the non-mergers (M_{BH} $\sim$3.8/4.0 $\times 10^8$ $M_\odot$).

We obtain the QSO bolometric luminosities by integrating the optical through FIR SEDs (Figures 3.29, Table 3.7) and express the in terms of the Eddington luminosity for these systems, $L_{Edd} = 1.25 \times 10^{38} M_{BH}(M_\odot)$ erg s^{-1} Figures 3.28(c)). The LoBALs span less than an order of magnitude in L_{bol} and show no difference among the interaction and morphology classes. All LoBALs show sub-Eddington accretion, with an average (median) Eddington ratio of 25% (20%) and range from 6-92%. Similar or lower ratios, for instance, are found for lower redshifts QSOs (e.g., McLeod & McLeod, 2001; Floyd et al., 2004; Veilleux et al., 2006, 2009).

If the non-mergers are assumed to be more advanced merger remnants, then there is a time delay in the driving of the outflows because the QSO luminosity reaches its peak in the merger stage but the outflows are higher among the no mergers.

If the outflows observed in LoBALs are responsible for quenching the merger-induced star formation, which peaks during the merger stage of our systems, then an estimate of the time between the merger and the no merger stages would constrain the time scales of the quenching process. On the other hand, we note that only four of the LoBALs

have high SFRs measured from their FIR emission: two with SFR $\sim$ 150 M$\odot$ yr^{-1} and two with SFR $\sim$ 300 M$\odot$ yr^{-1}. These objects make up only 31% of the mergers. Hence, the majority of the mergers already have low levels of SFR measured only as upper limits $<$50 M$\odot$ yr^{-1}. It is not very clear at which stage of the merger process the quenching of the star formation occurs. If the outflow phase is indeed short, then outflows must be triggered during the various stages of the merger process since we observe LoBALs from binary nuclei at separation 6 kpc to fully relaxed host with no signs of tidal interaction. Since QSO activity, i.e., black hole accretion, is triggered with increasing intensity during each subsequence pericenter passage (e.g., Van Wassenhove et al., 2012), then it is possible that LoBALs are short outflow phases observed at various times.

3.6 Conclusions

Our two-dimensional GALFIT analysis of HST WFC3 IR/F125W and UVIS/F475W images of volume-limited sample of 22 optically-selected LoBAL QSOs at $0.5 < z < 0.6$ indicates that the majority of them (73%) represent early-type (i.e., bulge) morphology. However, most of them are not well fit by the classical de Vaucouleurs surface brightness distribution (n = 4) but converge to Sersic profile with larger Sersic indices. Four (18%) of the LoBALs represent late-type (i.e., disk) morphology. Unambiguous signs of tidal interaction, such as interacting companions, extended tidal tails, plumes, and debris, are seen in 59%. If more subtle signs of old interaction are considered, such as boxy isophotes, asymmetries, or pseudobulge profiles seen in three additional systems, then the fraction of merger systems is possibly as high as 73%. The morphologically disturbed systems repre-

sent various stages of the merger process: from two separate nuclei to relaxed bulges with extremely low surface brightness tidal tails.

The host sizes of the more advanced mergers are smaller than the systems with companions, while the QSO magnitudes increase from binary to single nucleus merger systems, which is consistent with increasing the fuel supply for black hole accretion. The decrease in SFR is anti-correlated with the increase of the maximum velocity of the Mg II broad absorption line, which may indicate that the outflows observed in LoBALs may by responsible for quenching the merger-induced star formation. The length of the tidal tails indicate a dynamical time since the start of the merger of $\sim$ 150 Myr. If the AGN was triggered at that same time, then finding that most of the hosts have star formation at the level of unobscured type-1 QSO suggests average time scale for quenching of less than 150 Myr, consistent with simulations .

The disturbed morphologies and the dominance of bulges strongly suggests that LoBALs are low redshift are a population of QSOs which are a product of a galaxy merger or have experienced a merger event in the recent past. Our results are consistent with LoBALs being a key link between mergers and QSOs, a short phase marked by high velocity outflow which possibly quenched the star formation in the host galaxy. If LoBALs represent the blowout phase predicted by simulations of major mergers, then the sub-Eddington ratios and the observance of a large fraction of binary systems with apparently interacting companions questions that model. The imaging observation presented here strongly suggest that outflows occur at various stages of the merger process. We find that LoBALs emit at

sub-Eddington luminosities, in contrast to predictions of simulations that the blowout phase is marked by near-Eddington emission.

These LoBALs were drawn from a sample of optically selected QSOs. It is possible that the optically selected LoBALs represent the last stage of the blowout phase when the central QSO is already cleared the gas and dust enshrouding it. More dust-obscured LoBALs may represent the early outflow stage, however, those would normally be missed in optical-selections because their luminosities would not classify them as QSOs.

Table 3.1: Details of the HST WFC3 Observations

#	SDSS Object ID	RA (J2000)	DEC (J2000)	z	Total exposure time (s)		Number of frames		Scale (kpc arcsec^{-1})
					F125W	F475W	F125W	F475W	
(1)	(2)	(3)	(4)	(5)	(6)	(7)	(8)	(9)	(10)
1	J023102.49−083141.2	02 31 02.500	−08 31 41.28	0.596	1006	1536	2	2	6.652
2	J023153.63−093333.5	02 31 53.643	−09 33 33.57	0.587	1006	1536	2	2	6.603
3	J025026.66+000903.4	02 50 26.660	+00 09 03.40	0.554	1006	1530	2	2	6.417
4	J083525.98+435211.2	08 35 25.980	+43 52 11.30	0.568	906	1486	2	4	6.498
5	J085053.12+445122.5	08 50 53.120	+44 51 22.50	0.541	906	1486	2	4	6.340
6	J085215.66+492040.8	08 52 15.663	+49 20 40.88	0.566	1006	1692	2	2	6.487
7	J085357.87+463350.6	08 53 57.880	+46 33 50.60	0.550	1006	1436	2	4	6.394
8	J101151.95+542942.7	10 11 51.950	+54 29 42.70	0.536	1006	1748	2	2	6.310
9	J102802.32+592906.6	10 28 02.320	+59 29 06.70	0.535	1006	1556	2	4	6.304
10	J105102.77+525049.8	10 51 02.770	+52 50 49.90	0.543	1006	1748	2	2	6.352
11	J105404.73+042939.3	10 54 04.730	+04 29 39.30	0.578	1006	1530	2	2	6.554
12	J112822.41+482309.9	11 28 22.410	+48 23 10.00	0.543	906	1536	2	4	6.304
13	J114043.62+532439.0	11 40 43.620	+53 24 39.00	0.530	1006	1492	2	4	6.273
14	J130952.89+011950.6	13 09 52.890	+01 19 50.60	0.547	806	1472	2	4	6.376
15	J140025.53−012957.0	14 00 25.540	−01 29 57.00	0.584	1006	1530	2	2	6.587
16	J141946.36+463424.3	14 19 46.370	+46 34 24.30	0.546	1006	1692	2	2	6.370
17	J142649.24+032517.7	14 26 49.243	+03 25 17.71	0.530	1006	1530	2	2	6.273
18	J142927.28+523849.5	14 29 27.280	+52 38 49.50	0.594	1006	1492	2	4	6.641
19	J161425.17+375210.7	16 14 25.170	+37 52 10.70	0.553	906	1448	2	4	6.412
20	J170010.83+395545.8	17 00 10.828	+39 55 45.82	0.577	1006	1604	2	2	6.549
21	J170341.82+383944.7	17 03 41.821	+38 39 44.77	0.554	1006	1604	2	2	6.417
22	J204333.20−001104.2	20 43 33.200	−00 11 04.30	0.545	806	1472	2	4	6.364

Notes.−Col. (1): Object number in the sample. Col. (2): Official SDSS designation. Cols. (3) and (4): Optical positions taken from NED, where units of right ascension are hours, minutes, and seconds, and units of declination are degrees, arcminutes, and arcseconds. Col. (5): Redshift as listed in NED. Col. (6) and (7): Total integration time, in seconds, of the WFC3/IR-F125W and WFC3/UVIS-F475W observations. Col. (8) and (9): Number of frames combined with multidrizzle. Col. (10): Physical scale in kpc arcsec^{-1}.

Table 3.2: WFC3/F475W: GALFIT results

#	SDSS Object ID	Model	n	r_e		b/a	PA	m_n	m_{PSF}	χ^2
				(pixels)	(kpc)		(deg)	(AB mag)	(AB mag)	
(1)	(2)	(3)	(4)	(5)	(6)	(7)	(8)	(9)	(10)	(11)
01	J023102.49−083141.2	PSF	···	···	···	···	···	···	18.33	2.1
02	J023153.64−093333.6	PSF	···	···	···	···	···	···	18.82	1.8
03	J025026.66+000903.3	Sersic	0.71	30.95	6.95	0.48	45.08	21.19	19.82	1.7
04	J083525.98+435211.3	PSF	···	···	···	···	···	···	16.35	2.9
05	J085053.12+445122.4	PSF	···	···	···	···	···	···	16.52	*662
06	J085215.65+492040.8	PSF	···	···	···	···	···	···	18.27	*177
	Companion	Sersic	[1.05]	[3.13]	0.71	[0.18]	[70.54]	[23.20]		
07	J085357.88+463350.6	PSF	···	···	···	···	···	···	16.71	3.5
08	J101151.95+542942.6	Sersic	3.85	8.57	1.89	0.66	-28.99	20.94	19.18	*560
09	J102802.33+592906.7	PSF	···	···	···	···	···	···	17.53	2.2
10	J105102.78+525049.8	PSF	···	···	···	···	···	···	18.34	*160
11	J105404.72+042939.3	PSF	···	···	···	···	···	···	19.22	1.7
	Companion	Sersic	[1.77]	[2.78]	0.64	[0.84]	[-18.45]	[23.78]		
12	J112822.42+482310.1	PSF	···	···	···	···	···	···	16.35	*554
13	J114043.62+532438.9	PSF	···	···	···	···	···	···	16.65	*473
14	J130952.89+011950.6	PSF	···	···	···	···	···	···	16.61	3.9
15	J140025.53−012957.0	Sersic	0.31	27.43	6.32	0.71	22.48	21.01	18.12	1.7
16	J141946.37+463424.3	PSF	···	···	···	···	···	···	18.91	1.8
17	J142649.24+032517.7	PSF	···	···	···	···	···	···	18.00	1.9
18	J142927.28+523849.5	Sersic	1.48	14.34	3.33	0.53	-30.63	21.40	16.25	*216
19	J161425.17+375210.7	PSF	···	···	···	···	···	···	15.77	*583
20	J170010.82+395545.8	Sersic	0.74	30.15	6.91	0.60	-15.30	20.13	19.36	1.9
21	J170341.82+383944.7	PSF	···	···	···	···	···	···	18.38	*141
22	J204333.20−001104.2	Sersic	0.55	15.38	3.43	0.98	-84.66	23.16	17.00	*567

Notes.−Col. (1): Object number in the sample. Col. (2): Official SDSS designation. Col. (3): Components to the fitted model: PSF = only PSF + sky; Sersic = PSF + sky + Sersic profile. Col. (4): Sersic index. Cols. (5) and (6): Half-light radius of the Sersic component in pixels and in kpc, respectively. Col. (7): Axis ratio (minor/major) of the Sersic component. Col. (8): Position angle of major axis of the Sersic component, in degrees East of North. (9): Apparent F475W (SDSS g') magnitude of the Sersic component, in AB magnitudes, not corrected for Galactic or host extinction. Col. (10): Apparent F475W (SDSS g') magnitude of the PSF component, in AB magnitudes. Col. (11): Reduced χ^2. Square brackets indicate that the parameter was kept fixed. A star (*) indicates unphysical parameter.

Table 3.3: WFC3/F125W: GALFIT results

#	SDSS Object ID	Model	n	r_e		b/a	PA	m_n	m_{PSF}	χ^2
				(pixels)	(kpc)		(deg)	(AB mag)	(AB mag)	
(1)	(2)	(3)	(4)	(5)	(6)	(7)	(8)	(9)	(10)	(11)
01	J023102.49−083141.2	Sersic	9.10	5.41	2.52	0.63	64.19	18.21	19.35	2.0
		deVac	[4.00]	6.45	3.00	[0.85]	63.55	18.53	18.97	2.1
		Exp	[1.00]	9.60	4.47	[0.85]	61.23	18.98	18.67	2.3
02	J023153.64−093333.6	Sersic	8.33	10.20	4.71	0.81	-20.04	18.50	18.93	1.2
		deVac	[4.00]	8.78	4.06	0.82	-18.41	18.81	18.79	1.2
		Exp	[1.00]	9.22	4.26	0.82	-15.04	19.29	18.64	1.4
03	J025026.66+000903.3	Sersic	1.56	12.22	5.49	0.58	47.34	18.23	18.13	1.7
		deVac	[4.00]	11.93	5.36	0.58	47.19	17.93	18.30	1.9
		Exp	[1.00]	12.59	5.66	0.58	47.54	18.35	18.09	1.7
04	J083525.98+435211.3	Sersic	5.95	0.87	0.40	0.87	73.15	17.50	18.60	2.7
		deVac	[4.00]	0.96	0.44	0.81	78.11	17.46	18.77	2.8
		Exp	[1.00]	1.27	0.58	0.72	76.29	17.47	18.89	3.2
05	J085053.12+445122.4	Sersic	9.53	1.09	0.48	0.87	-51.73	16.84	18.83	3.6
		deVac	[4.00]	1.72	0.76	0.95	52.27	17.09	18.24	4.2
		Exp	[1.00]	5.45	2.42	0.98	-53.13	17.95	17.31	6.1
06	J085215.65+492040.8	Sersic	1.14	11.10	5.04	0.62	54.35	19.65	17.90	1.6
		deVac	[4.00]	14.42	6.55	0.61	55.14	19.19	17.94	1.6
		Exp	[1.00]	10.89	4.95	0.62	54.33	19.68	17.90	1.6
07	J085357.88+463350.6	Sersic	6.48	6.17	2.76	0.57	-45.65	17.47	17.65	2.4
		deVac	[4.00]	7.01	3.14	0.58	-45.91	17.67	17.53	2.5
		Exp	[1.00]	9.14	4.09	0.59	-46.70	18.16	17.35	3.8
08	J101151.95+542942.6	Sersic	2.45	7.59	3.35	0.84	-44.29	18.46	18.99	2.9
		deVac	[4.00]	7.09	3.13	0.83	-41.26	18.28	19.18	2.9
		Exp	[1.00]	7.69	3.40	0.84	-40.75	18.72	18.83	3.1
09	J102802.33+592906.7	Sersic	2.15	7.95	3.51	0.85	56.45	19.57	18.21	1.4
		deVac	[4.00]	7.03	3.10	0.85	56.14	19.34	18.26	1.4
		Exp	[1.00]	8.69	3.83	0.86	57.00	19.82	18.18	1.4
10	J105102.78+525049.8	Sersic	7.97	2.50	1.11	0.60	-41.94	17.73	19.80	1.7
		deVac	[4.00]	4.29	1.91	0.62	-42.14	18.06	18.87	1.8
		Exp	[1.00]	8.15	3.62	0.60	-41.15	18.60	18.30	2.1
11	J105404.72+042939.3	Sersic	7.01	5.09	2.34	0.74	-56.50	18.15	19.98	1.5
	Companion	deVac	[4.00]	10.15	4.66	0.66	-3.69	20.61		
		deVac	[4.00]	2.57	1.18	0.70	-49.53	18.28	20.83	1.6
	Companion	deVac	[4.00]	28.03	12.96	0.89	-30.19	19.40		
		Exp	[1.00]	4.50	2.06	0.71	-48.84	18.89	19.22	2.0
	Companion	deVac	[4.00]	37.44	17.18	0.87	-29.72	19.02		

Continues

Notes.−Col. (1): Object number in the sample. Col. (2): Official SDSS designation. Col. (4): Sersic index. Cols. (5) and (6): Half-light radius of the Sersic component in pixels and in kpc, respectively. Col. (7): Axis ratio (minor/major) of the Sersic component. Col. (8): Position angle of major axis of the Sersic component, in degrees East of North. (9): Apparent F125W (J) magnitude of the Sersic component, in AB magnitudes. Average error in magnitude is 0.3 mag. Col. (10): Apparent F125W (J) magnitude of the PSF component, in AB magnitudes, not corrected for Galactic or host extinction. Col. (11): Reduced χ^2.Square brackets indicate that the parameter was kept fixed. A star (*) indicates unphysical parameter.

Table 3.3: −Continued

#	SDSS Object ID	Model	n	r_e		b/a	PA	m_n	m_{PSF}	χ^2
				(pixels)	(kpc)		(deg)	(AB mag)	(AB mag)	
(1)	(2)	(3)	(4)	(5)	(6)	(7)	(8)	(9)	(10)	(11)
12	J112822.42+482310.1	Sersic	*20.00*	9.18	4.05	0.61	-52.56	16.85	17.02	5.6
		deVac	[4.00]	8.91	3.93	0.64	-52.28	17.50	16.83	6.7
		Exp	[1.00]	16.66	7.35	0.64	-53.49	17.96	16.67	8.0
13	J114043.62+532438.9	Sersic	7.47	2.87	1.26	0.64	86.68	17.65	18.31	2.2
		deVac	[4.00]	3.79	1.66	0.66	86.40	17.88	18.07	2.4
		Exp	[1.00]	7.27	3.19	0.66	85.02	18.49	17.73	3.6
14	J130952.89+011950.6	Sersic	1.80	15.05	6.72	0.99	13.92	18.07	16.86	3.1
		deVac	[4.00]	17.57	7.84	1.00	-78.23	17.77	16.89	3.2
		Exp	[1.00]	14.59	6.51	0.99	7.25	18.25	16.84	3.2
15	J140025.53−012957.0	Sersic	0.69	12.51	5.77	0.79	22.91	18.85	17.75	1.9
		deVac	[4.00]	11.22	5.17	0.88	31.43	18.39	17.84	2.2
		Exp	[1.00]	12.11	5.58	0.81	23.58	18.77	17.76	2.0
16	J141946.37+463424.3	Sersic	7.10	27.35	12.20	0.83	-41.67	17.86	18.97	1.1
	Companion	Sersic	9.45	0.67	0.30	0.52	-33.28	20.25		
		deVac	[4.00]	19.57	8.73	0.84	-37.90	18.11	18.82	1.1
	Companion	Sersic	3.64	0.67	0.30	0.60	-36.24	20.42		
		Exp	[1.00]	13.13	5.85	0.86	-36.37	18.71	18.66	1.5
	Companion	Sersic	*18.04*	0.81	0.36	0.53	-20.56	20.06		
17	J142649.24+032517.7	Sersic	2.58	11.25	4.94	0.90	-62.87	17.83	17.60	1.8
		deVac	[4.00]	10.98	4.82	0.90	-64.63	17.68	17.66	1.8
		Exp	[1.00]	11.67	5.12	0.89	-57.72	18.14	17.51	2.2
18	J142927.28+523849.5	Sersic	0.70	*0.21*	0.10	*0.05*	19.91	17.63	16.81	7.5
		deVac	[4.00]	10.48	4.87	0.15	-44.78	21.95	16.39	7.8
		Exp	[1.00]	*0.29*	0.13	0.83	1.71	17.49	16.87	7.5
19	J161425.17+375210.7	Sersic	*19.27*	0.74	0.33	0.87	-87.13	16.40	16.76	6.0
		deVac	[4.00]	5.34	2.40	0.86	-85.77	17.36	16.26	6.3
		Exp	[1.00]	9.66	4.34	0.84	-88.54	17.95	16.17	7.0
20	J170010.82+395545.8	Sersic	0.89	12.70	5.82	0.76	-9.38	18.07	19.25	3.3
		deVac	[4.00]	13.34	6.12	0.67	-0.64	17.72	19.99	4.2
		Exp	[1.00]	12.65	5.80	0.75	-8.53	18.05	19.28	3.3
21	J170341.82+383944.7	Sersic	2.68	15.19	6.82	0.86	-58.79	18.34	17.18	2.5
		deVac	[4.00]	15.37	6.90	0.85	-60.40	18.20	17.21	2.6
		Exp	[1.00]	15.61	7.01	0.88	-54.93	18.66	17.14	2.7
22	J204333.20−001104.2	Sersic	5.52	6.10	2.72	0.45	-82.25	18.23	17.35	2.2
		deVac	[4.00]	7.25	3.23	0.46	-82.05	18.37	17.31	2.2
		Exp	[1.00]	10.56	4.70	0.48	-81.86	18.90	17.21	2.4

Notes.−Col. (1): Object number in the sample. Col. (2): Official SDSS designation. Col. (4): Sersic index. Cols. (5) and (6): Half-light radius of the Sersic component in pixels and in kpc, respectively. Col. (7): Axis ratio (minor/major) of the Sersic component. Col. (8): Position angle of major axis of the Sersic component, in degrees East of North. (9): Apparent F125W (J) magnitude of the Sersic component, in AB magnitudes. Col. (10): Apparent F125W (J) magnitude of the PSF component, in AB magnitudes, not corrected for Galactic or host extinction. Col. (11): Reduced χ^2.Square brackets indicate that the parameter was kept fixed. A star (*) indicates unphysical parameter.

Table 3.4: Summary of the F125W Morphologies.

#	Object ID	Visual features		Sersic index	Morphological class	Interaction class	Comments
		Companion	Tidal tail				
(1)	(2)	(3)	(4)	(5)	(6)	(7)	(8)
1	J0231−0831	Yes, ∼1″N	Two arches	9.1	Bulge*	Merger	Shell-like half- and quarter-circle tails
2	J0231−0933	···	···	8.3	Bulge*	Non merger	Relaxed system; no tidal features
3	J0250+0009	···	Two: 7″NW, 6″S	1.6	Disk	Merger	Two huge tidal tails; pseudobulge
4	J0835+4352	···	···	6.0	···	Non merger	Unresolved host, r_e ∼1 pixel; no tidal features
5	J0850+4451	···	···	9.5	···	Non merger	Unresolved host; Triangular isophotes (contour map)
6	J0852+4920	Yes, ∼1″S	···	1.1	Disk	Merger	Small companion discovered after modeling the host
7	J0853+4633	···	Curved	6.5	Bulge*	Merger	Huge curved tidal tail
8	J1011+5429	Yes,∼1.″3W	···	2.5	Bulge	Merger	Interacting companion
9	J1028+5929	···	···	2.2	Bulge	Non merger	Pseudobulge; no tidal features
10	J1051+5250	···	···	8.0	Bulge*	Non merger	Compact spiral arm structure; compact host, no tidal features
11	J1054+0429	Yes,∼ 1″SW	Faint, 6″E	7.0	Bulge*	Merger	Interacting companion
12	J1128+4823	···	Faint, 6″S	20.0	Bulge*	Merger	Extended faint tidal tail
13	J1140+5324	···	···	7.5	Bulge*	Non merger	Significant residuals; West-extending isophotes (contour map)
14	J1309+0119	···	···	1.8	Bulge	Non merger	Quarter-circle arc to the NE (lens?); pseudobulge; Boxy isophotes (contour)
15	J1400−0129	···	···	0.7	Disk	Non merger	Arm-like structure near center; bright knot ∼1″S; Off-center peak
16	J1419+4634	Yes,∼ 0.″9S	Two: 7″NW; 1.″3SE	7.1	Bulge*	Merger	
17	J1426+0325	Yes,∼ 2″N	···	2.6	Bulge	Merger	Shell-like structure; bridge extending N to the second nucleus
18	J1429+5238	···	···	[4.0]	Bulge	Non merger	No tidal features
19	J1614+3752	···	Faint, 7″S	19.3	Bulge*	Merger	
20	J1700+3955	Possible,<1″E	Arms or Tails?	0.9	Disk	Merger	Clumpy; Possible second nucleus
21	J1703+3839	···	Faint, 6″N	2.7	Bulge	Merger	
22	J2043−0011	···	···	5.5	Bulge*	Merger	Elongated nucleus; boxy isophotes (contour map); resembles M82

Notes.−Col. (1): Object number in the sample. Col. (2): Truncated SDSS designation. Col (3): Presence of interacting companion, distance of companion from central source, and direction in WCS. Col. (4): Presence of tidal tail, approximate length in arc-seconds, and orientation in WCS. Col. (5): Sersic index of the best-fitting one-component model. Col. (6): Morphological class according to the best-fitting Sersic index: B = bulge-dominated (n-free>2), Disk = disk-dominated (n-free<2); * indicates n-free>4. Col. (7) Interaction class: Pre-merger = two nuclei and signs of tidal disturbance; Merger = one nucleus and unambiguous signs of tidal interaction; No merger = no unmistakable signs of tidal interaction.

Table 3.5: F125W Absolute Magnitudes and Luminosities, and Black Hole Masses Estimated from SDSS Spectra.

#	Object ID	D_L	E(B-V)	A_V	M_{total}	M_{QSO}	M_{HOST}	L_{total}	L_{QSO}	L_{HOST}	I_{QSO}/I_{HOST}	M_{BH}	V_{max}
		(Mpc)	(Galactic)	(QSO)	(AB mag)			(Log($L/L_\odot$))				(Log(M/$M_\odot$))	(km s^{-1})
(1)	(2)	(3)	(4)	(5)	(6)	(7)	(8)	(9)	(10)	(11)	(12)	(13)	(14)
1	J0231−0831	3494.8	0.04	···	-24.80	-23.33	-24.47	11.35	10.77	11.22	0.35	8.48	4662.
2	J0231−0933	3430.4	0.03	···	-24.71	-23.72	-24.15	11.32	10.92	11.09	0.67	9.01	2129.
3	J0250+0009	3126.5	0.07	1.03	-24.99	-24.28	-24.18	11.43	11.15	11.11	1.10	8.59	3533.
4	J0835+4352	3295.3	0.03	0.00	-25.40	-23.96	-25.06	11.59	11.02	11.46	0.36	8.95	28968.
5	J0850+4451	3105.6	0.03	0.14	-25.75	-23.60	-25.59	11.74	10.88	11.67	0.16	9.32	5191.
6	J0852+4920	3281.2	0.02	0.41	-24.86	-24.66	-22.91	11.38	11.30	10.60	5.01	9.00	2283.
7	J0853+4633	3168.5	0.02	0.53	-25.68	-24.84	-25.02	11.71	11.37	11.44	0.85	8.81	4523.
8	J1011+5429	3070.7	0.01	0.52	-24.49	-23.44	-23.97	11.23	10.81	11.02	0.61	8.52	3203.
9	J1028+5929	3063.8	0.01	0.00	-24.49	-24.21	-22.85	11.23	11.12	10.58	3.50	8.49	2682.
10	J1051+5250	3119.5	0.01	0.50	-24.88	-22.66	-24.73	11.39	10.50	11.33	0.15	8.91	2583.
11	J1054+0429	3366.3	0.04	0.51	-24.63	-22.62	-24.45	11.29	10.48	11.21	0.19	8.68	1803.
12	J1128+4823	3119.5	0.02	0.61	-26.27	-25.43	-25.60	11.94	11.61	11.68	0.86	9.25	4496.
13	J1140+5324	3029.0	0.01	0.00	-25.22	-24.09	-24.75	11.52	11.07	11.33	0.54	9.04	3665.
14	J1309+0119	3147.5	0.04	0.14	-25.90	-25.59	-24.38	11.80	11.67	11.19	3.05	···	1869.
15	J1400−0129	3409.0	0.05	0.69	-25.20	-24.87	-23.77	11.52	11.38	10.94	2.75	8.55	28993.
16	J1419+4634	3140.5	0.01	0.48	-24.95	-23.51	-24.62	11.41	10.84	11.28	0.36	8.04	4712.
17	J1426+0325	3029.0	0.04	0.44	-25.41	-24.77	-24.54	11.60	11.34	11.25	1.24	8.60	4800.
18	J1429+5238	3480.5	0.01	0.28	-26.32	-26.31	-20.75	11.96	11.96	9.73	167.49	8.51	5981.
19	J1614+3752	3189.6	0.02	0.10	-26.69	-25.74	-26.10	12.11	11.73	11.87	0.72	8.85	6789.
20	J1700+3955	3359.2	0.02	0.42	-24.86	-23.36	-24.54	11.38	10.78	11.25	0.34	7.82	5677.
21	J1703+3839	3196.6	0.04	0.83	-25.63	-25.31	-24.15	11.69	11.56	11.09	2.91	8.74	7611.
22	J2043−0011	3133.5	0.06	0.28	-25.48	-25.08	-24.20	11.62	11.47	11.11	2.25	8.54	8354.

Notes.−Col. (1): Object number in the sample. Col. (2) SDSS designation. Cols. (6), (7), and (8): Absolute magnitudes corrected for Galactic extinction, but not corrected for host extinction.

Table 3.6: F475W Absolute Magnitudes and Luminosities

#	Object ID	M_{total}	M_{QSO}	M_{HOST}	L_{total}	L_{QSO}	L_{HOST}	I_{QSO}/I_{HOST}	M_{total}^{F475W}-M_{total}^{F125W}	L_{bol}^{QSO}	L_{bol}/L_{Edd}
		(AB mag)			(Log($L/L_\odot$))					(Log($L/L_\odot$))	
(1)	(2)	(3)	(4)	(5)	(6)	(7)	(8)	(9)	(10)	(11)	(12)
1	J0231-0831	-24.23	-24.23	···	11.54	11.54	···	0.35	0.57	···	···
2	J0231-0933	-23.74	-23.74	···	11.35	11.35	···	0.67	0.97	···	···
3	J0250+0009	-22.64	-22.37	-21.00	10.91	10.80	10.25	1.10	2.34	12.33	0.35
4	J0835+4352	-26.12	-26.12	···	12.30	12.30	···	0.36	-0.72	12.23	0.12
5	J0850+4451	-25.82	-25.82	···	12.18	12.18	···	0.16	-0.07	12.30	0.06
6	J0852+4920	-24.23	-24.23	···	11.54	11.54	···	5.01	0.63	11.91	0.05
7	J0853+4633	-25.71	-25.71	···	12.14	12.14	···	0.85	-0.03	12.19	0.15
8	J1011+5429	-23.41	-23.22	-21.46	11.22	11.14	10.43	0.61	1.07	11.84	0.13
9	J1028+5929	-24.86	-24.86	···	11.80	11.80	···	3.50	-0.38	11.71	0.10
10	J1051+5250	-24.09	-24.09	···	11.49	11.49	···	0.15	0.79	11.91	0.06
11	J1054+0429	-23.26	-23.26	···	11.15	11.15	···	0.19	1.38	11.89	0.10
12	J1128+4823	-26.04	-26.04	···	12.27	12.27	···	0.86	0.23	12.58	0.14
13	J1140+5324	-25.72	-25.72	···	12.14	12.14	···	0.54	-0.50	12.12	0.08
14	J1309+0119	-25.72	-25.72	···	12.14	12.14	···	3.05	0.18	12.40	···
15	J1400-0129	-24.42	-24.34	-21.45	11.62	11.59	10.43	2.75	0.79	12.23	0.30
16	J1419+4634	-23.53	-23.53	···	11.27	11.27	···	0.36	1.41	11.64	0.25
17	J1426+0325	-24.25	-24.25	···	11.55	11.55	···	1.24	1.17	12.20	0.25
18	J1429+5238	-26.43	-26.42	-21.27	12.42	12.42	10.36	167.49	-0.11	12.54	0.67
19	J1614+3752	-26.67	-26.67	···	12.52	12.52	···	0.72	0.02	12.63	0.38
20	J1700+3955	-23.63	-23.19	-22.42	11.30	11.13	10.82	0.34	1.23	11.98	0.92
21	J1703+3839	-23.98	-23.98	···	11.44	11.44	···	2.91	1.65	12.24	0.20
22	J2043-0011	-25.24	-25.24	-19.08	11.95	11.95	9.48	2.25	0.23	12.27	0.34

Notes.−Col. (1): Object number in the sample. Col. (2) SDSS designation. Cols. (3), (4), and (5): Absolute magnitudes corrected for Galactic extinction, but not corrected for host extinction.

Table 3.7: Total host magnitudes, integrated after subtracting the PSF model.

#	Object ID	m_{F125W}	m_{F475W}	$m_{F475W} - m_{F125W}$
(1)	(2)	(3)	(4)	(5)
1	J0231-0831	18.44	22.08	3.64
2	J0231-0933	18.91	23.47	4.56
3	J0250+0009	18.29	21.53	3.23
4	J0835+4352	17.54	···	···
5	J0850+4451	16.93	19.92	2.99
6	J0852+4920	19.74	22.38	2.63
7	J0853+4633	17.57	22.49	4.92
8	J1011+5429	18.46	20.78	2.32
9	J1028+5929	19.69	···	···
10	J1051+5250	17.86	22.83	4.97
11	J1054+0429	18.17	22.47	4.30
12	J1128+4823	17.21	···	···
13	J1140+5324	17.74	22.35	4.61
14	J1309+0119	18.42	21.26	2.84
15	J1400-0129	18.85	21.16	2.32
16	J1419+4634	18.29	22.83	4.54
17	J1426+0325	17.89	22.04	4.15
18	J1429+5238	19.99	20.55	0.56
19	J1614+3752	16.61	···	···
20	J1700+3955	18.05	20.20	2.15
21	J1703+3839	18.59	22.67	4.09
22	J2043-0011	18.28	···	···
24	J1614+3752	17.72	18.81	1.09

Notes.−Col. (1): Object number in the sample. Col. (2) SDSS designation. Col. (3) and (4): Total magnitudes, not corrected for extinctions (neither Galactic nor host).

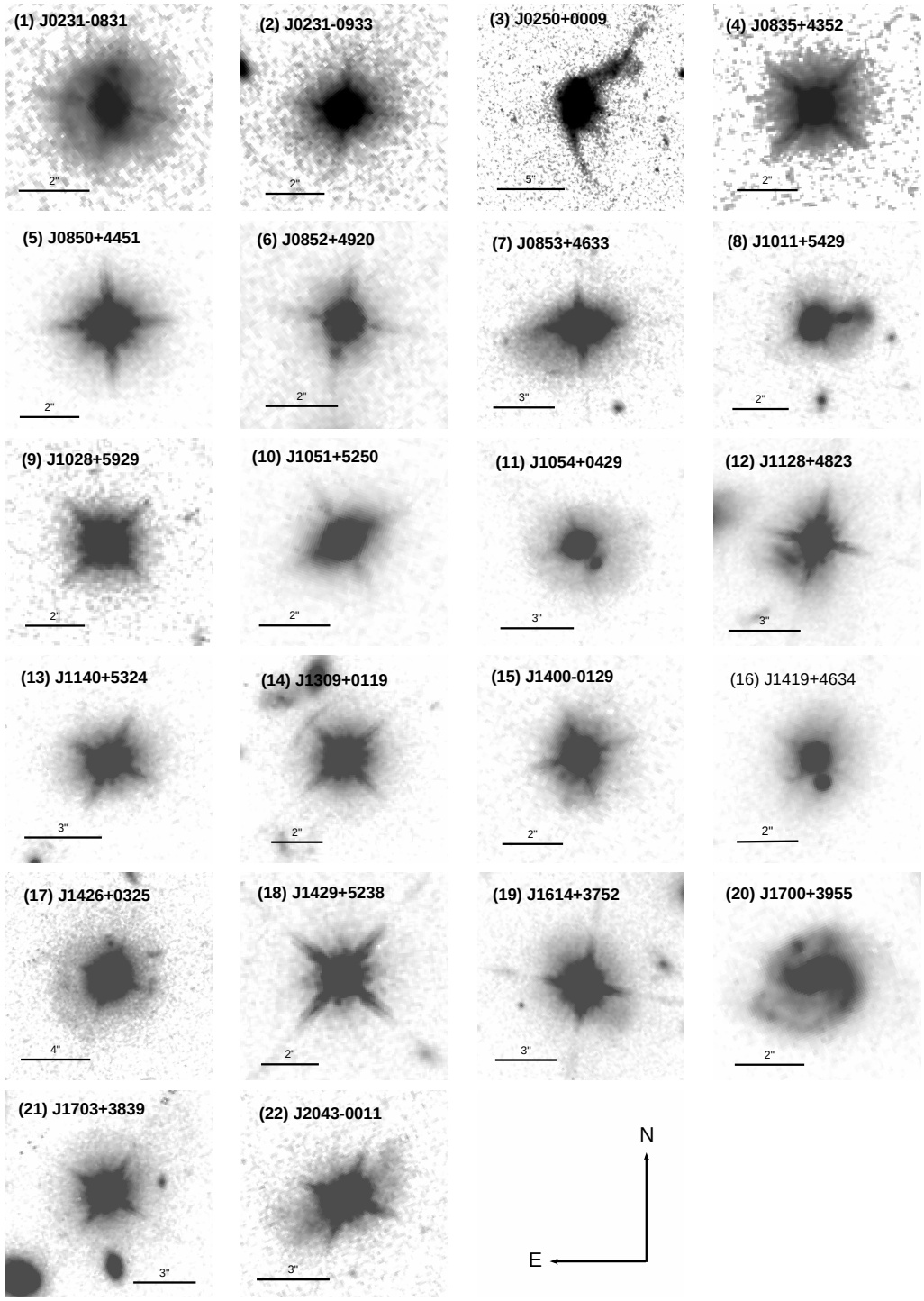

Figure 3.1: Postage stamp HST/WFC3 F125W images of the 22 LoBALs. The arcsecond scale is noted with a bar on each image. At the median redshift of the samplem z = 0.55, the physical scale is 6.4 kpc arcsec^{-1}. North is up; East is to the left.

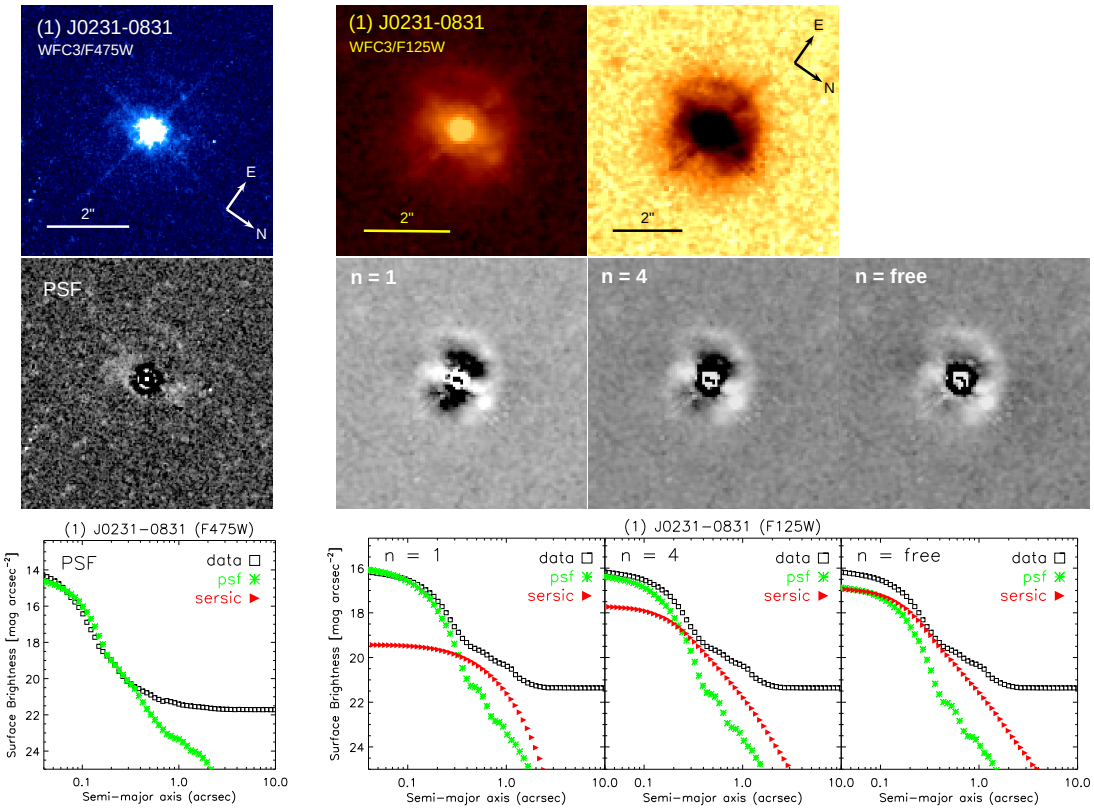

Figure 3.2: HST/WFC3 F475W (in blue, top left) and F125W (in red, top right) images of SDSS J0231-0831. In gray on the second row we show the residual image after subtracting the best fit GAFIT model. The particular model is indicated at the right top corner of the residual image: n = 1 is an exponential disk, n = 4 is a de Vaucouleur profile, and n = free indicates unconstrained Sersic index. On the third row we show radial surface brightness profiles of each component in the particular model, indicated again in the right top corner of each plot.

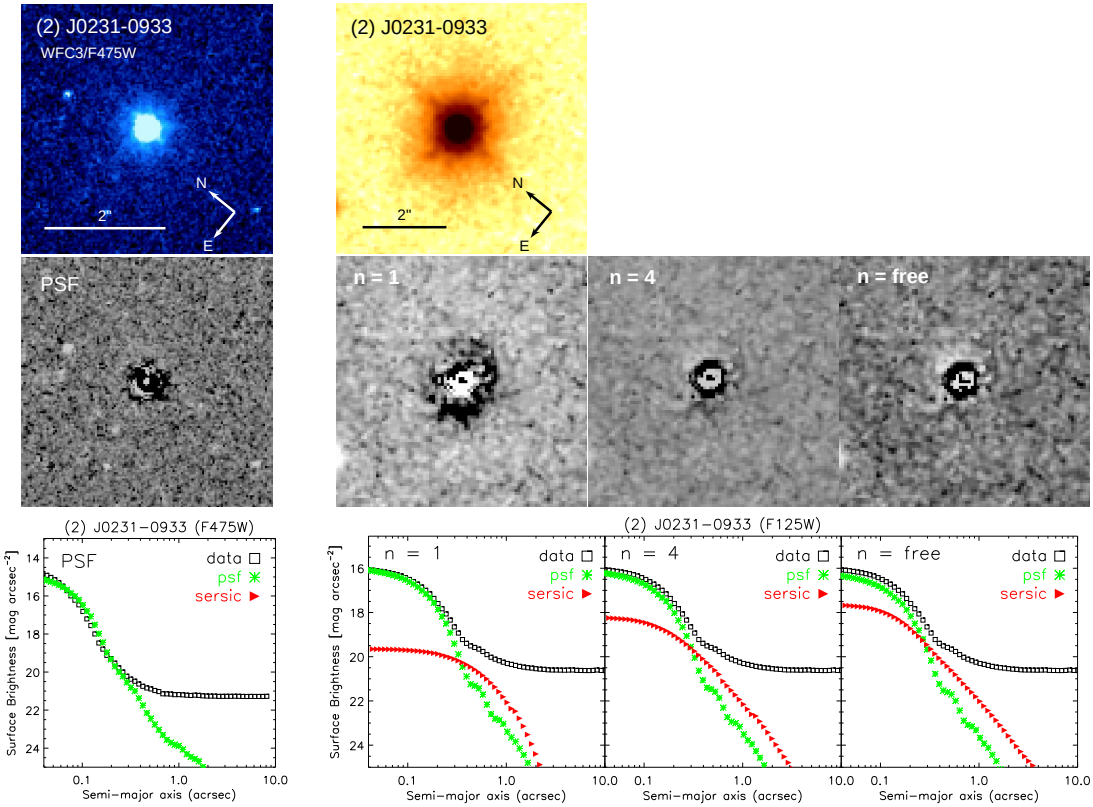

Figure 3.3: HST/WFC3 F475W (in blue, top left) and F125W (in red, top right) images of SDSS J0231-0933. In gray on the second row we show the residual image after subtracting the best fit GAFIT model. The particular model is indicated at the right top corner of the residual image: n = 1 is an exponential disk, n = 4 is a de Vaucouleur profile, and n = free indicates unconstrained Sersic index. On the third row we show radial surface brightness profiles of each component in the particular model, indicated again in the right top corner of each plot.

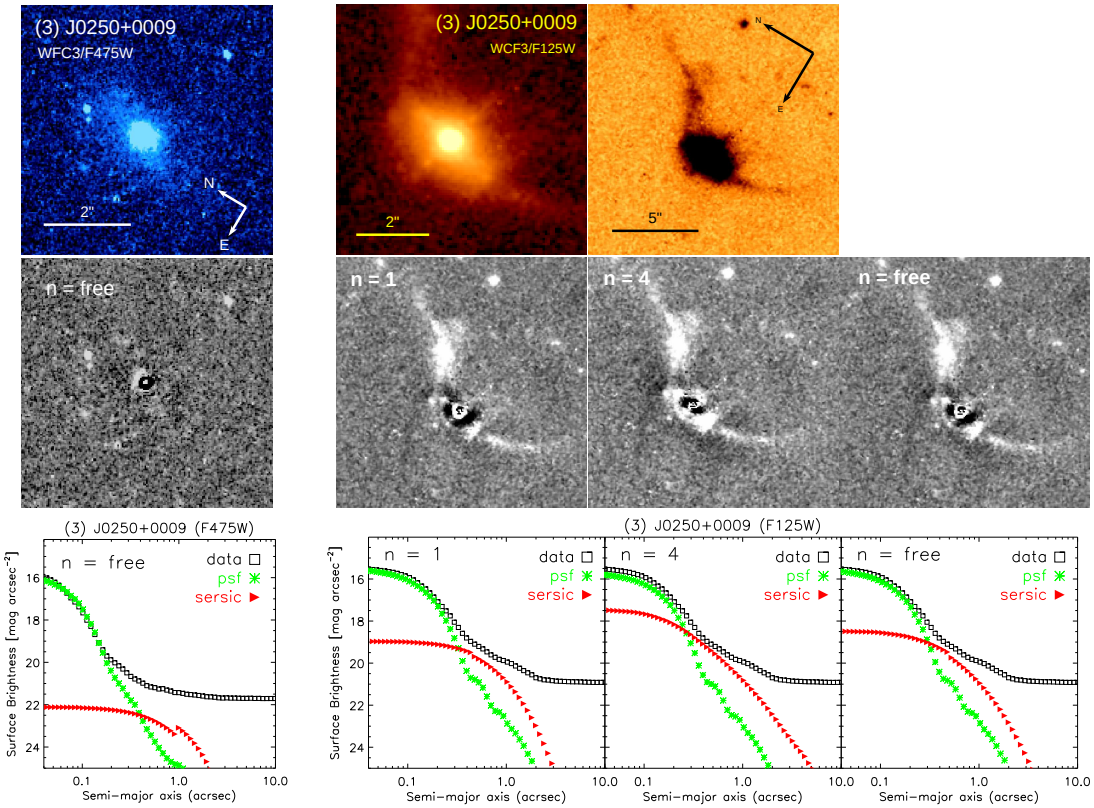

Figure 3.4: HST/WFC3 F475W (in blue, top left) and F125W (in red, top right) images of SDSS J0250+0009. In gray on the second row we show the residual image after subtracting the best fit GAFIT model. The particular model is indicated at the right top corner of the residual image: n = 1 is an exponential disk, n = 4 is a de Vaucouleur profile, and n = free indicates unconstrained Sersic index. On the third row we show radial surface brightness profiles of each component in the particular model, indicated again in the right top corner of each plot.

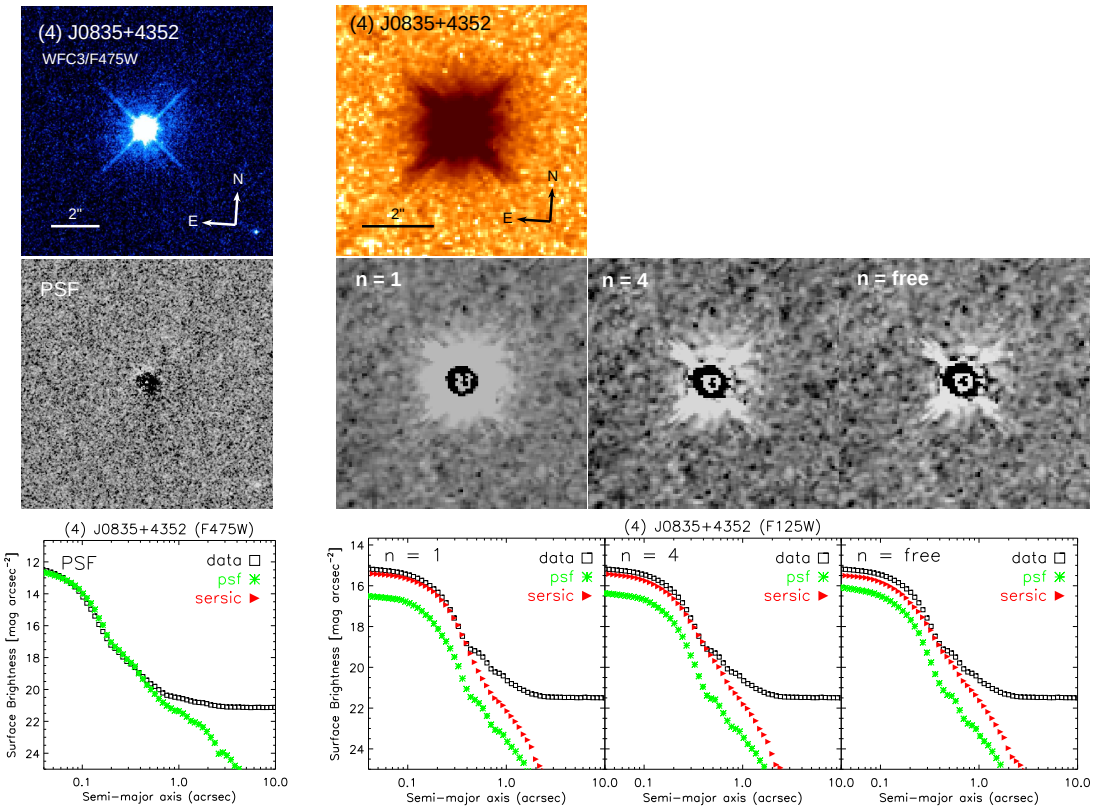

Figure 3.5: HST/WFC3 F475W (in blue, top left) and F125W (in red, top right) images of SDSS J0835+4352. In gray on the second row we show the residual image after subtracting the best fit GAFIT model. The particular model is indicated at the right top corner of the residual image: n = 1 is an exponential disk, n = 4 is a de Vaucouleur profile, and n = free indicates unconstrained Sersic index. On the third row we show radial surface brightness profiles of each component in the particular model, indicated again in the right top corner of each plot.

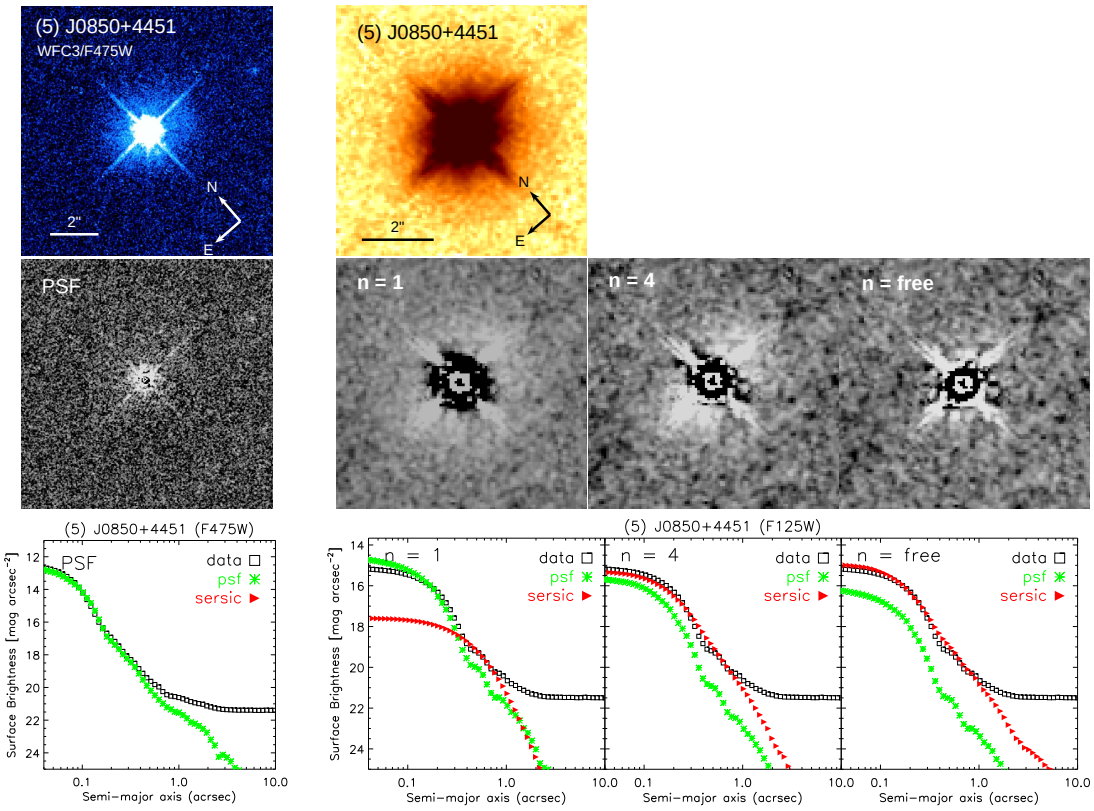

Figure 3.6: HST/WFC3 F475W (in blue, top left) and F125W (in red, top right) images of SDSS J0850+4451. In gray on the second row we show the residual image after subtracting the best fit GAFIT model. The particular model is indicated at the right top corner of the residual image: n = 1 is an exponential disk, n = 4 is a de Vaucouleur profile, and n = free indicates unconstrained Sersic index. On the third row we show radial surface brightness profiles of each component in the particular model, indicated again in the right top corner of each plot.

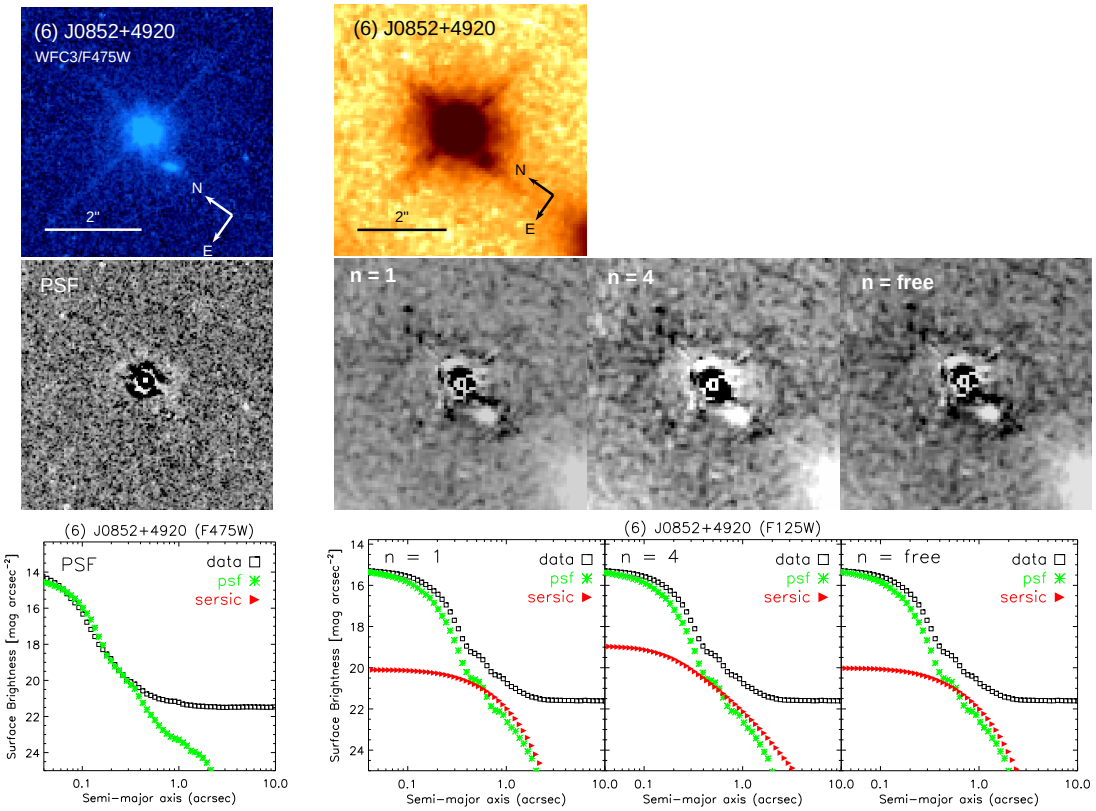

Figure 3.7: HST/WFC3 F475W (in blue, top left) and F125W (in red, top right) images of SDSS J0852+4920. In gray on the second row we show the residual image after subtracting the best fit GAFIT model. The particular model is indicated at the right top corner of the residual image: n = 1 is an exponential disk, n = 4 is a de Vaucouleur profile, and n = free indicates unconstrained Sersic index. On the third row we show radial surface brightness profiles of each component in the particular model, indicated again in the right top corner of each plot.

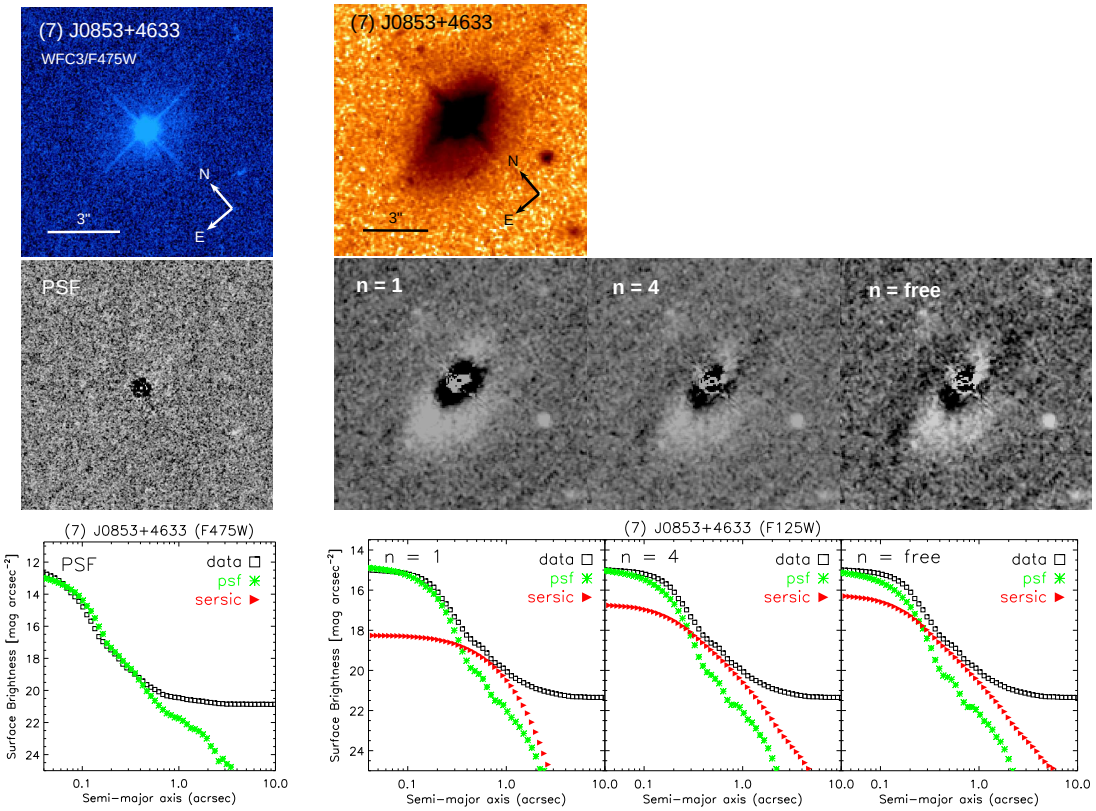

Figure 3.8: HST/WFC3 F475W (in blue, top left) and F125W (in red, top right) images of SDSS J0853+4633. In gray on the second row we show the residual image after subtracting the best fit GAFIT model. The particular model is indicated at the right top corner of the residual image: n = 1 is an exponential disk, n = 4 is a de Vaucouleur profile, and n = free indicates unconstrained Sersic index. On the third row we show radial surface brightness profiles of each component in the particular model, indicated again in the right top corner of each plot.

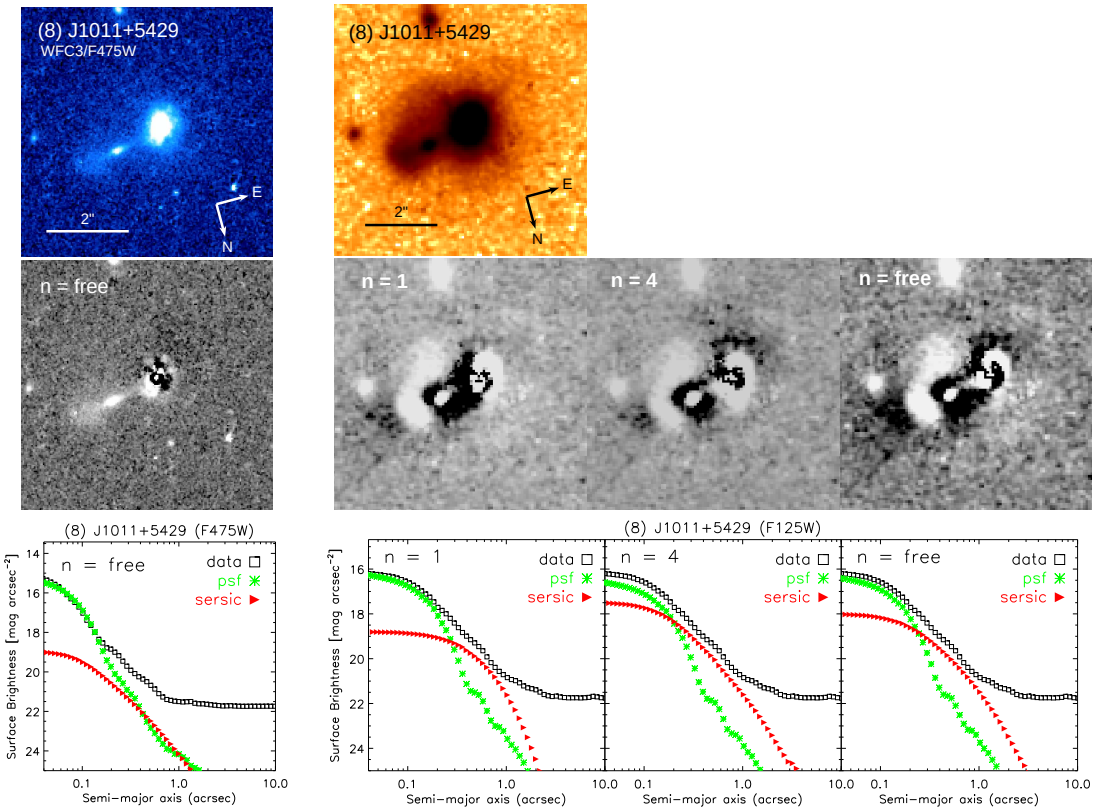

Figure 3.9: HST/WFC3 F475W (in blue, top left) and F125W (in red, top right) images of SDSS J1011+5429. In gray on the second row we show the residual image after subtracting the best fit GAFIT model. The particular model is indicated at the right top corner of the residual image: n = 1 is an exponential disk, n = 4 is a de Vaucouleur profile, and n = free indicates unconstrained Sersic index. On the third row we show radial surface brightness profiles of each component in the particular model, indicated again in the right top corner of each plot.

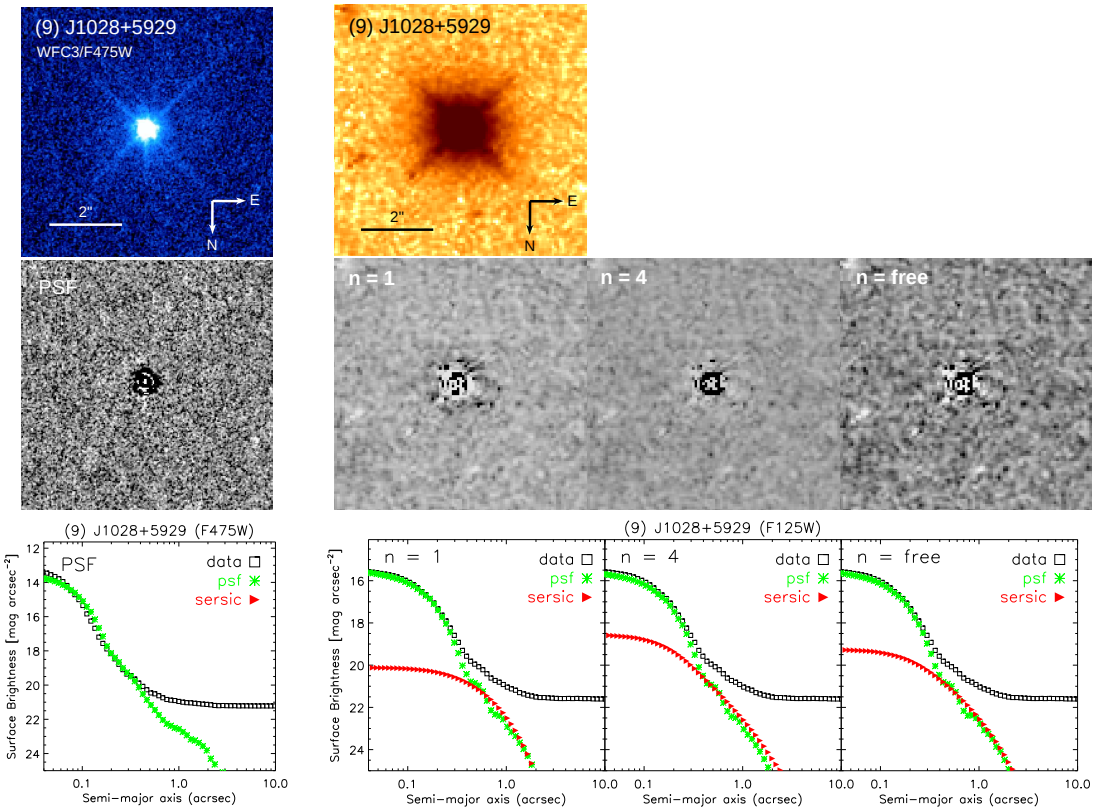

Figure 3.10: HST/WFC3 F475W (in blue, top left) and F125W (in red, top right) images of SDSS J1028+5929. In gray on the second row we show the residual image after subtracting the best fit GAFIT model. The particular model is indicated at the right top corner of the residual image: n = 1 is an exponential disk, n = 4 is a de Vaucouleur profile, and n = free indicates unconstrained Sersic index. On the third row we show radial surface brightness profiles of each component in the particular model, indicated again in the right top corner of each plot.

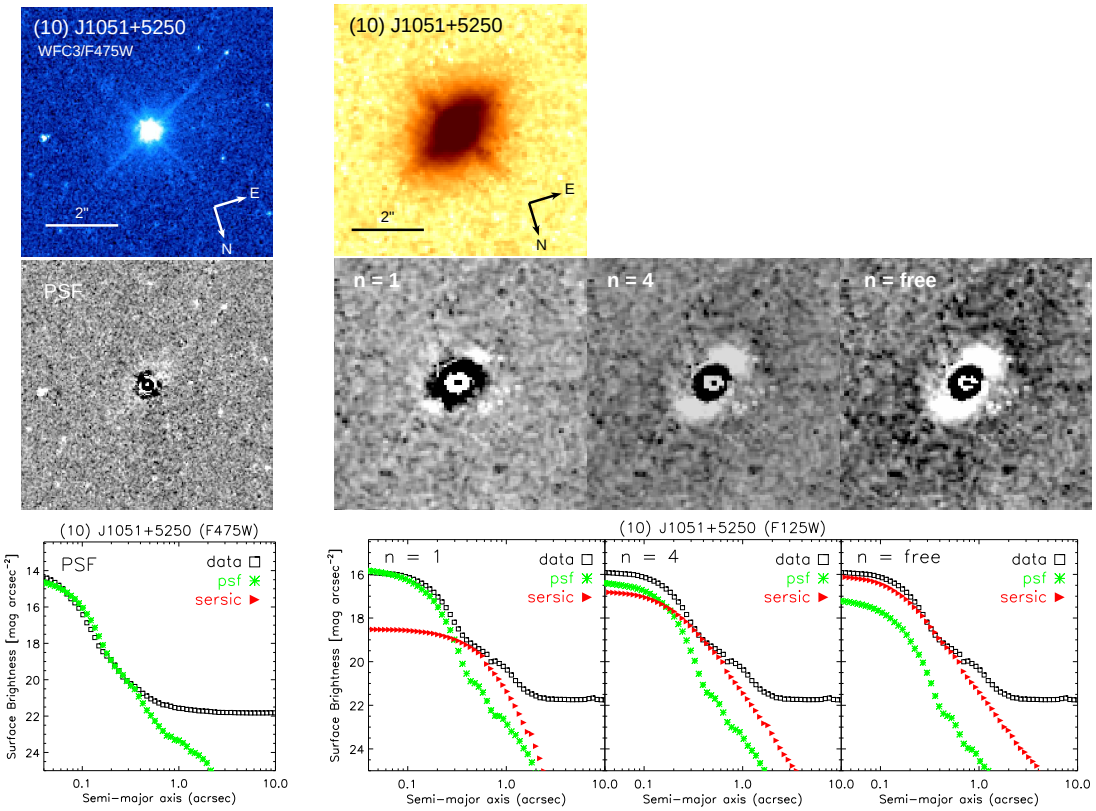

Figure 3.11: HST/WFC3 F475W (in blue, top left) and F125W (in red, top right) images of SDSS J1051+5250. In gray on the second row we show the residual image after subtracting the best fit GAFIT model. The particular model is indicated at the right top corner of the residual image: n = 1 is an exponential disk, n = 4 is a de Vaucouleur profile, and n = free indicates unconstrained Sersic index. On the third row we show radial surface brightness profiles of each component in the particular model, indicated again in the right top corner of each plot.

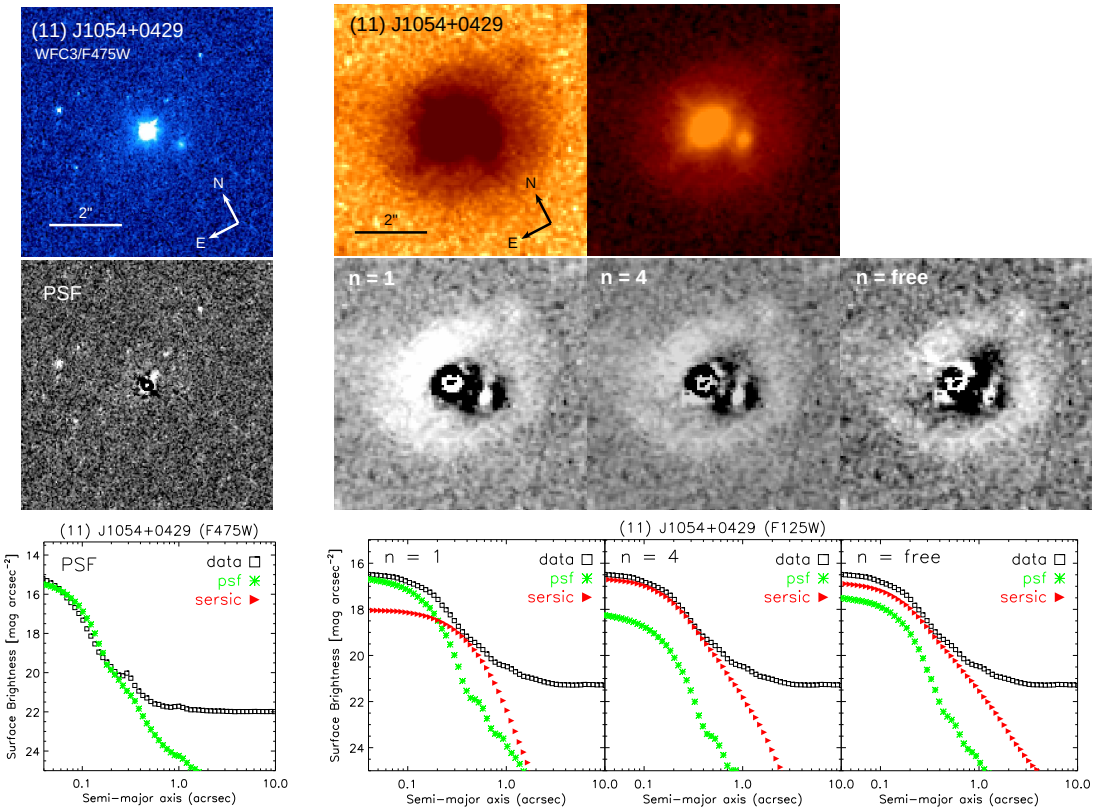

Figure 3.12: HST/WFC3 F475W (in blue, top left) and F125W (in red, top right) images of SDSS J1054+0429. In gray on the second row we show the residual image after subtracting the best fit GAFIT model. The particular model is indicated at the right top corner of the residual image: n = 1 is an exponential disk, n = 4 is a de Vaucouleur profile, and n = free indicates unconstrained Sersic index. On the third row we show radial surface brightness profiles of each component in the particular model, indicated again in the right top corner of each plot.

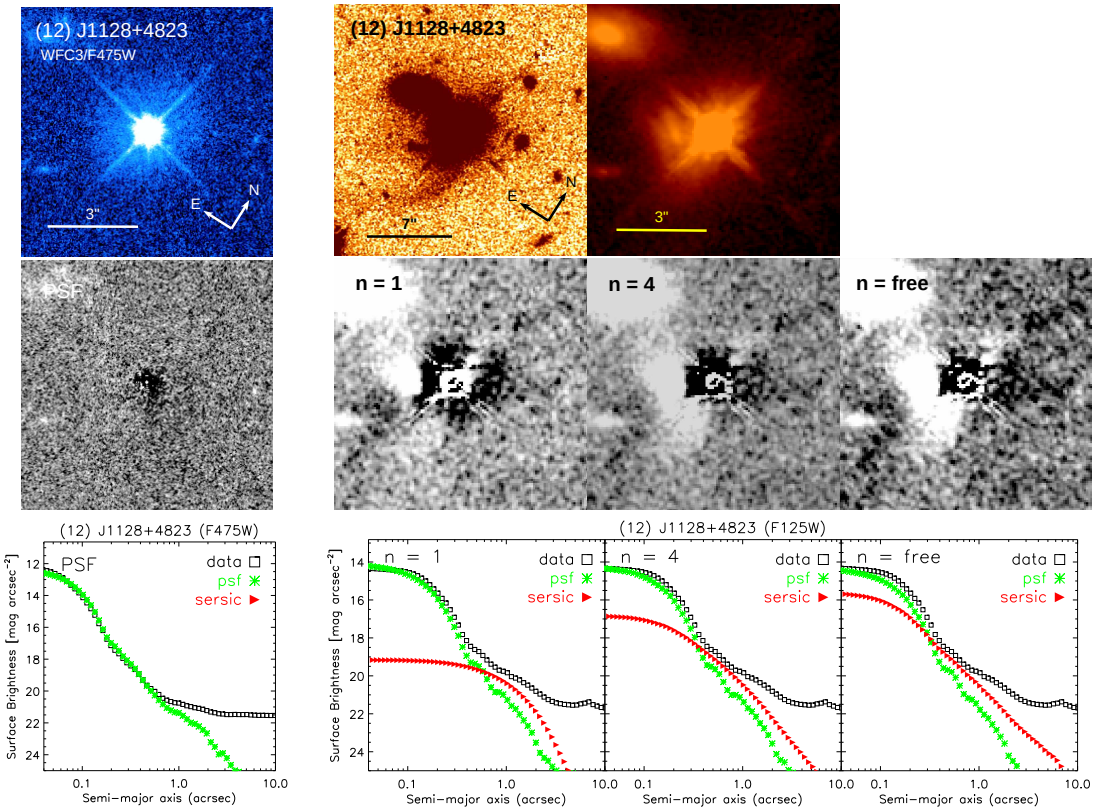

Figure 3.13: HST/WFC3 F475W (in blue, top left) and F125W (in red, top right) images of SDSS J1128+4823. In gray on the second row we show the residual image after subtracting the best fit GAFIT model. The particular model is indicated at the right top corner of the residual image: n = 1 is an exponential disk, n = 4 is a de Vaucouleur profile, and n = free indicates unconstrained Sersic index. On the third row we show radial surface brightness profiles of each component in the particular model, indicated again in the right top corner of each plot.

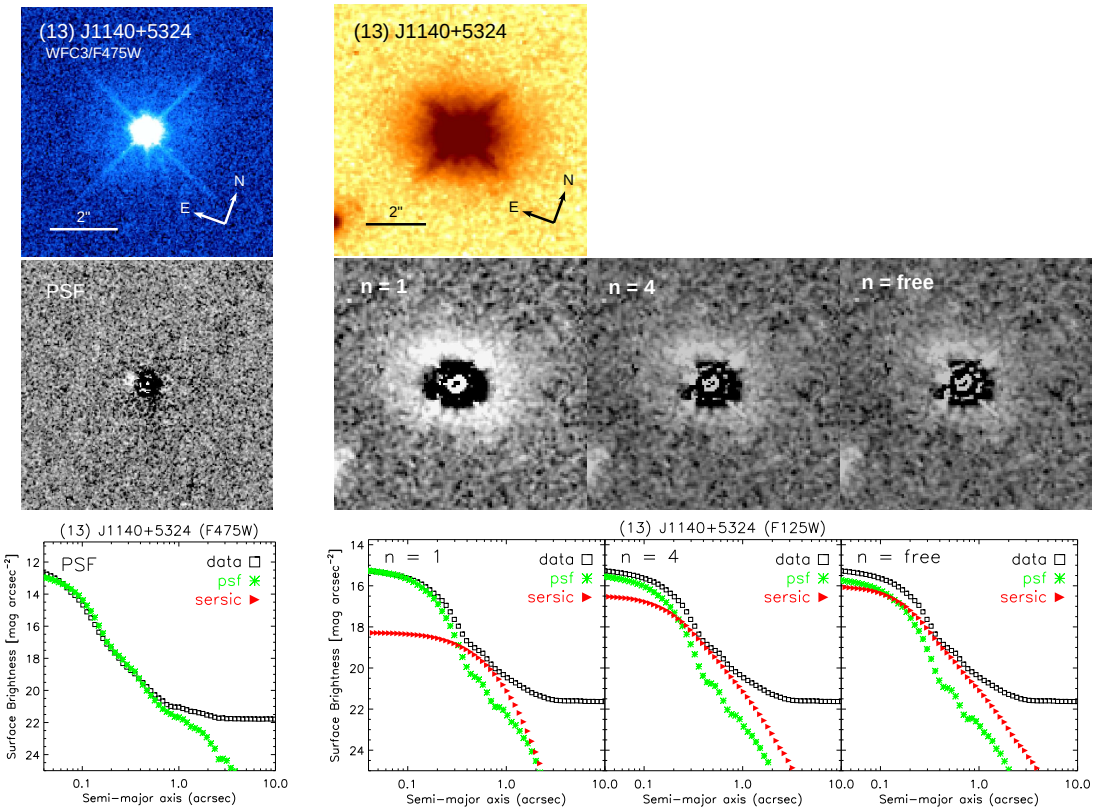

Figure 3.14: HST/WFC3 F475W (in blue, top left) and F125W (in red, top right) images of SDSS J1140+5324. In gray on the second row we show the residual image after subtracting the best fit GAFIT model. The particular model is indicated at the right top corner of the residual image: n = 1 is an exponential disk, n = 4 is a de Vaucouleur profile, and n = free indicates unconstrained Sersic index. On the third row we show radial surface brightness profiles of each component in the particular model, indicated again in the right top corner of each plot.

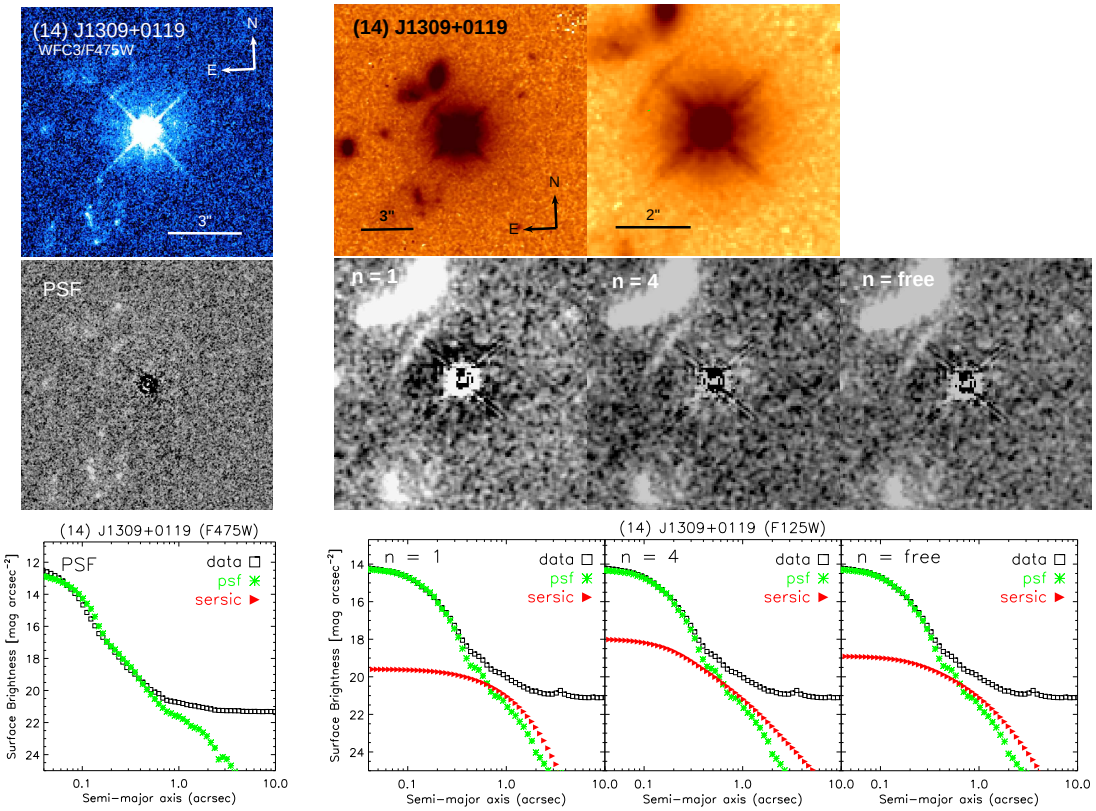

Figure 3.15: HST/WFC3 F475W (in blue, top left) and F125W (in red, top right) images of SDSS J1309+0119. In gray on the second row we show the residual image after subtracting the best fit GAFIT model. The particular model is indicated at the right top corner of the residual image: n = 1 is an exponential disk, n = 4 is a de Vaucouleur profile, and n = free indicates unconstrained Sersic index. On the third row we show radial surface brightness profiles of each component in the particular model, indicated again in the right top corner of each plot.

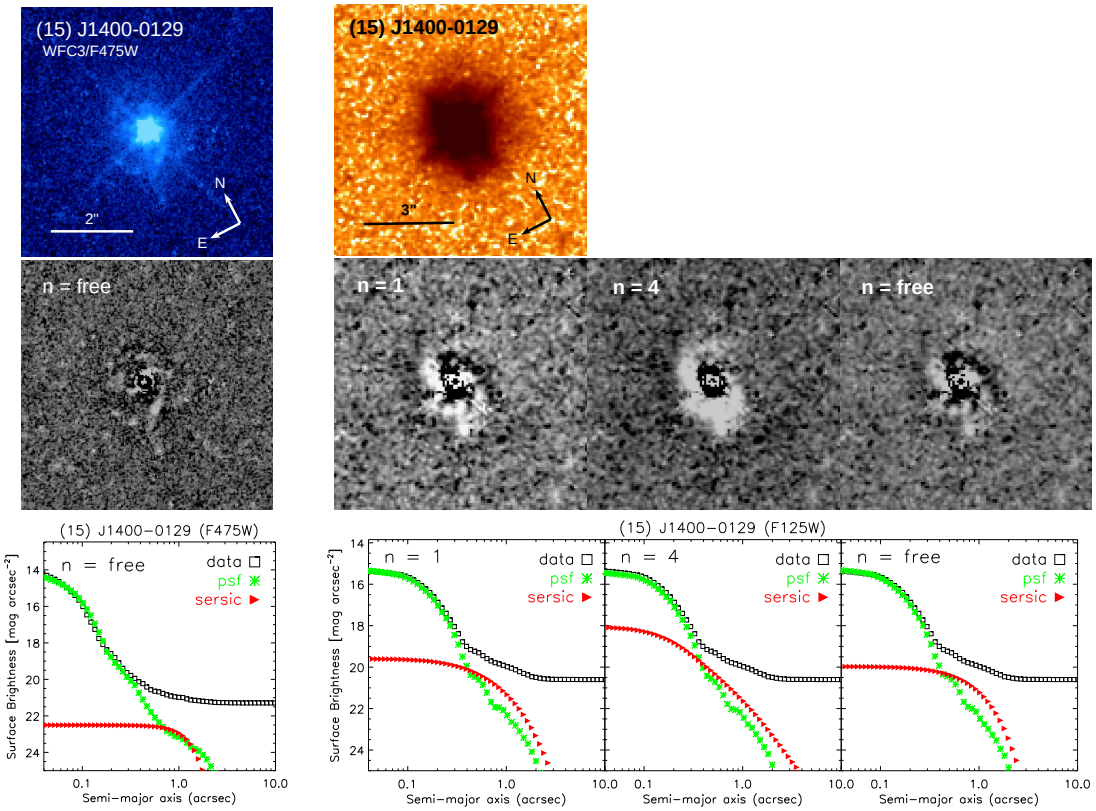

Figure 3.16: HST/WFC3 F475W (in blue, top left) and F125W (in red, top right) images of SDSS J1400-0129. In gray on the second row we show the residual image after subtracting the best fit GAFIT model. The particular model is indicated at the right top corner of the residual image: n = 1 is an exponential disk, n = 4 is a de Vaucouleur profile, and n = free indicates unconstrained Sersic index. On the third row we show radial surface brightness profiles of each component in the particular model, indicated again in the right top corner of each plot.

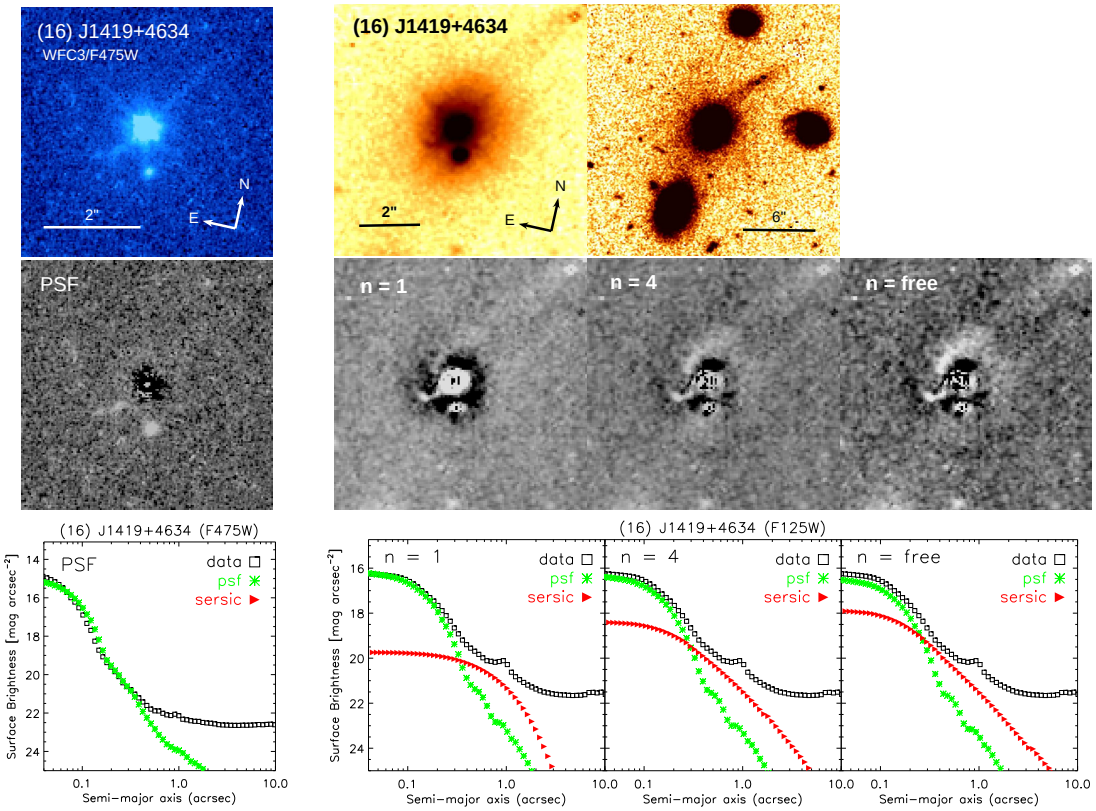

Figure 3.17: HST/WFC3 F475W (in blue, top left) and F125W (in red, top right) images of SDSS J1419+4634. In gray on the second row we show the residual image after subtracting the best fit GAFIT model. The particular model is indicated at the right top corner of the residual image: n = 1 is an exponential disk, n = 4 is a de Vaucouleur profile, and n = free indicates unconstrained Sersic index. On the third row we show radial surface brightness profiles of each component in the particular model, indicated again in the right top corner of each plot.

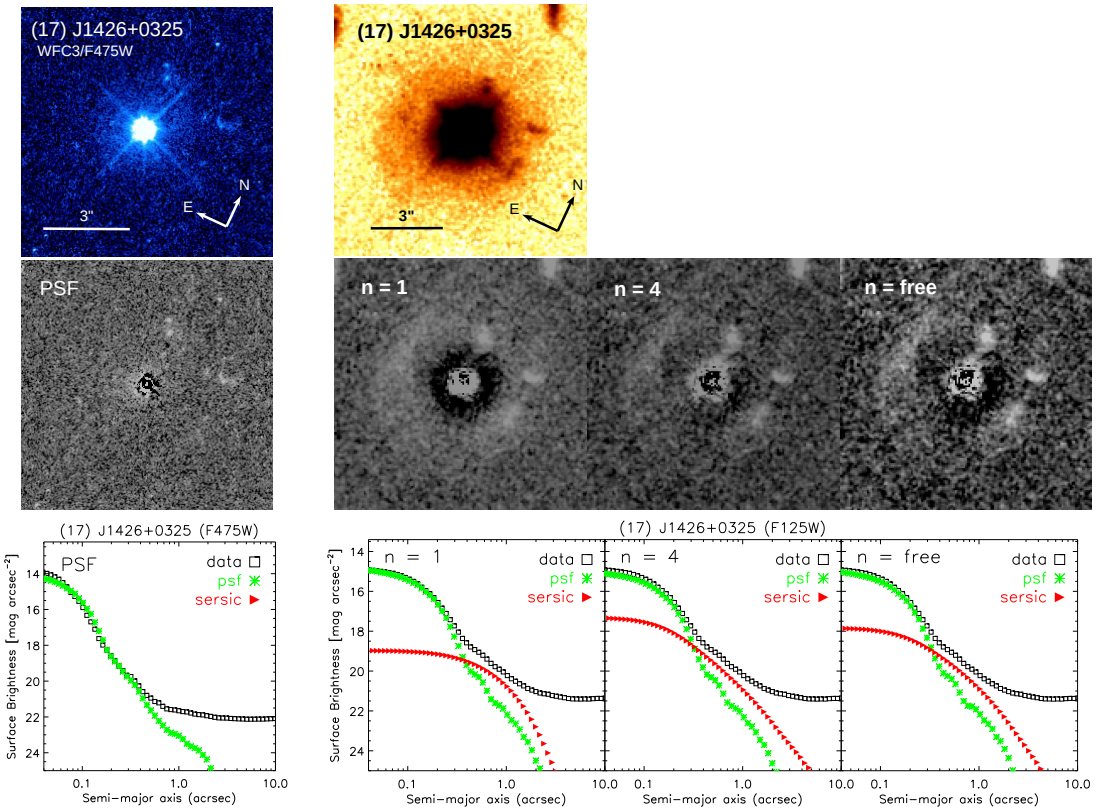

Figure 3.18: HST/WFC3 F475W (in blue, top left) and F125W (in red, top right) images of SDSS J1426+0325. In gray on the second row we show the residual image after subtracting the best fit GAFIT model. The particular model is indicated at the right top corner of the residual image: n = 1 is an exponential disk, n = 4 is a de Vaucouleur profile, and n = free indicates unconstrained Sersic index. On the third row we show radial surface brightness profiles of each component in the particular model, indicated again in the right top corner of each plot.

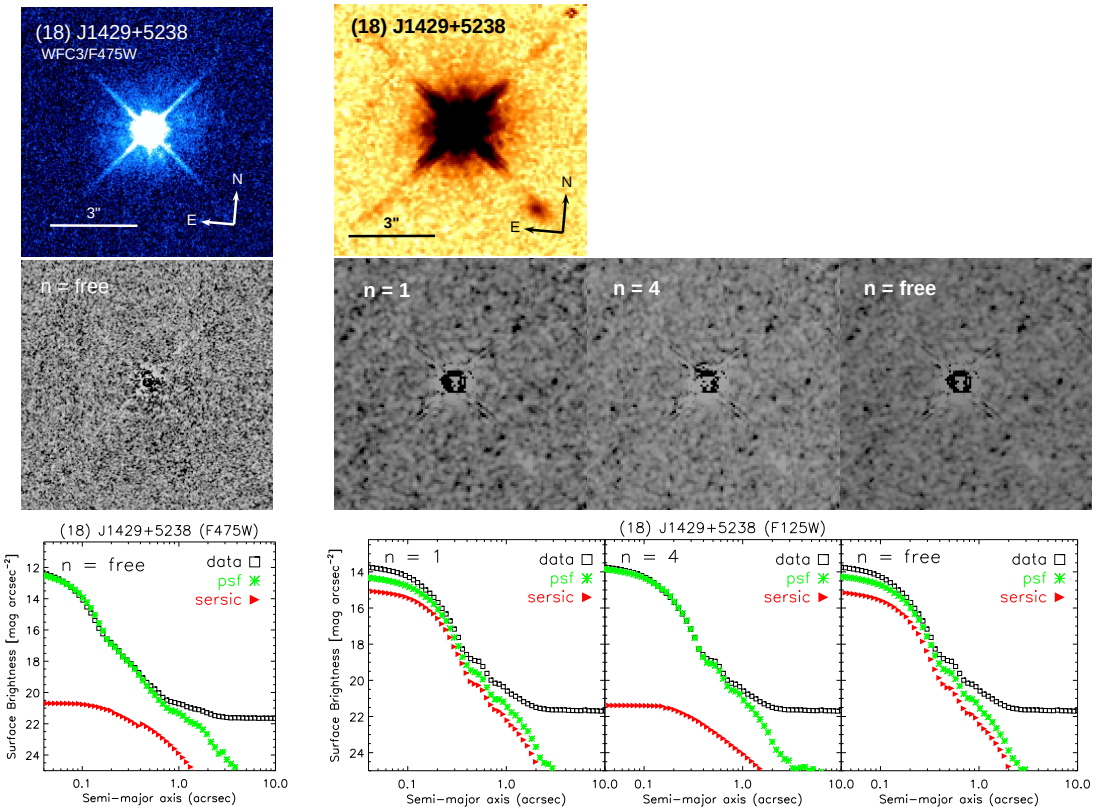

Figure 3.19: HST/WFC3 F475W (in blue, top left) and F125W (in red, top right) images of SDSS J1429+5238. In gray on the second row we show the residual image after subtracting the best fit GAFIT model. The particular model is indicated at the right top corner of the residual image: n = 1 is an exponential disk, n = 4 is a de Vaucouleur profile, and n = free indicates unconstrained Sersic index. On the third row we show radial surface brightness profiles of each component in the particular model, indicated again in the right top corner of each plot.

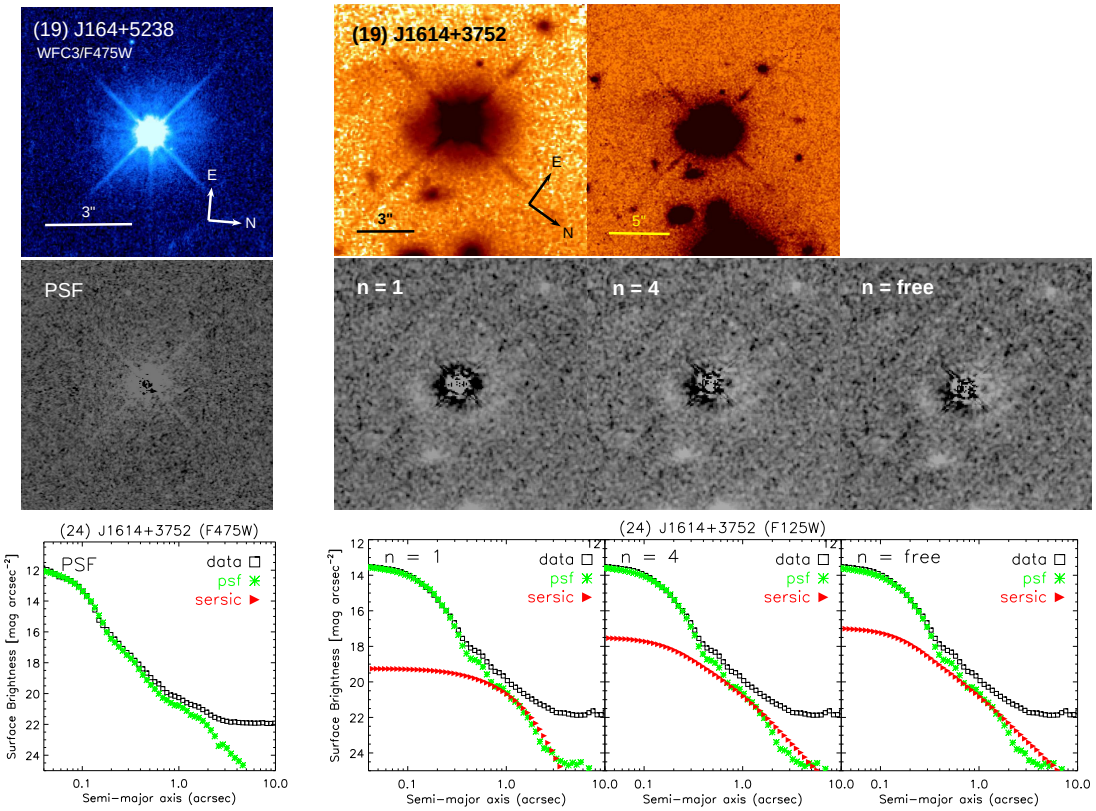

Figure 3.20: HST/WFC3 F475W (in blue, top left) and F125W (in red, top right) images of SDSS J1614+5238. In gray on the second row we show the residual image after subtracting the best fit GAFIT model. The particular model is indicated at the right top corner of the residual image: n = 1 is an exponential disk, n = 4 is a de Vaucouleur profile, and n = free indicates unconstrained Sersic index. On the third row we show radial surface brightness profiles of each component in the particular model, indicated again in the right top corner of each plot.

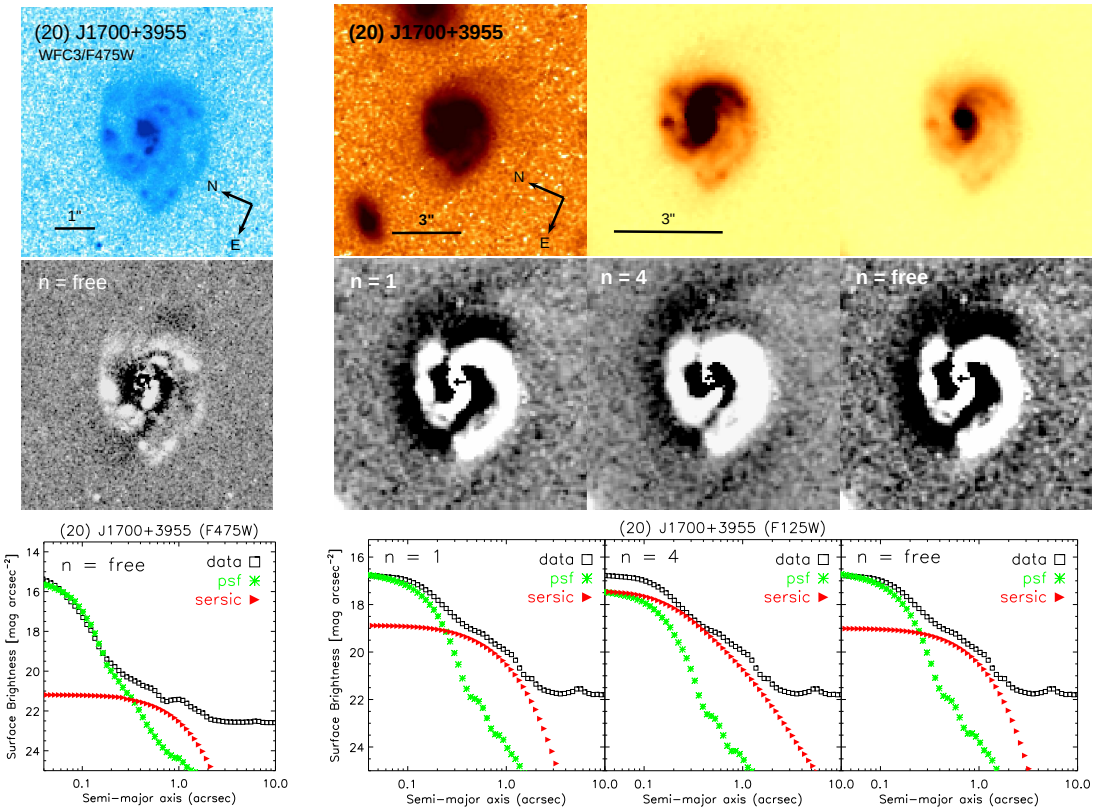

Figure 3.21: HST/WFC3 F475W (in blue, top left) and F125W (in red, top right) images of SDSS J1700+3955. In gray on the second row we show the residual image after subtracting the best fit GAFIT model. The particular model is indicated at the right top corner of the residual image: n = 1 is an exponential disk, n = 4 is a de Vaucouleur profile, and n = free indicates unconstrained Sersic index. On the third row we show radial surface brightness profiles of each component in the particular model, indicated again in the right top corner of each plot.

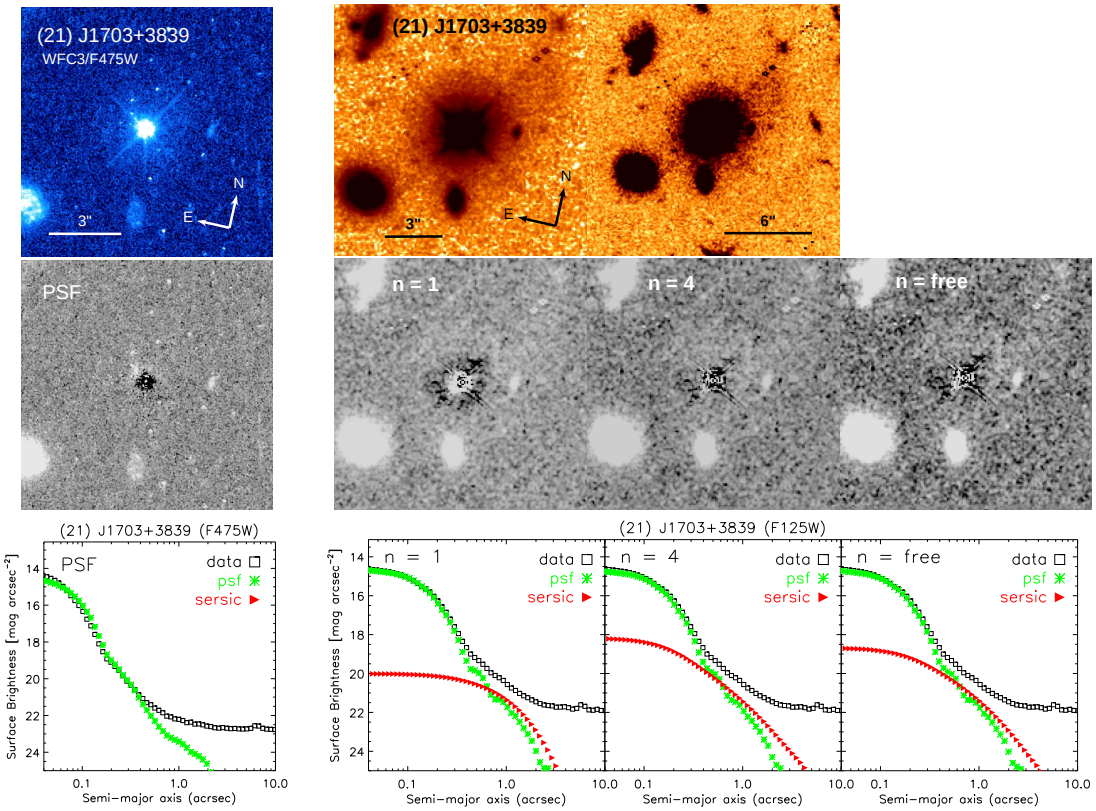

Figure 3.22: HST/WFC3 F475W (in blue, top left) and F125W (in red, top right) images of SDSS J1703+3839. In gray on the second row we show the residual image after subtracting the best fit GAFIT model. The particular model is indicated at the right top corner of the residual image: n = 1 is an exponential disk, n = 4 is a de Vaucouleur profile, and n = free indicates unconstrained Sersic index. On the third row we show radial surface brightness profiles of each component in the particular model, indicated again in the right top corner of each plot.

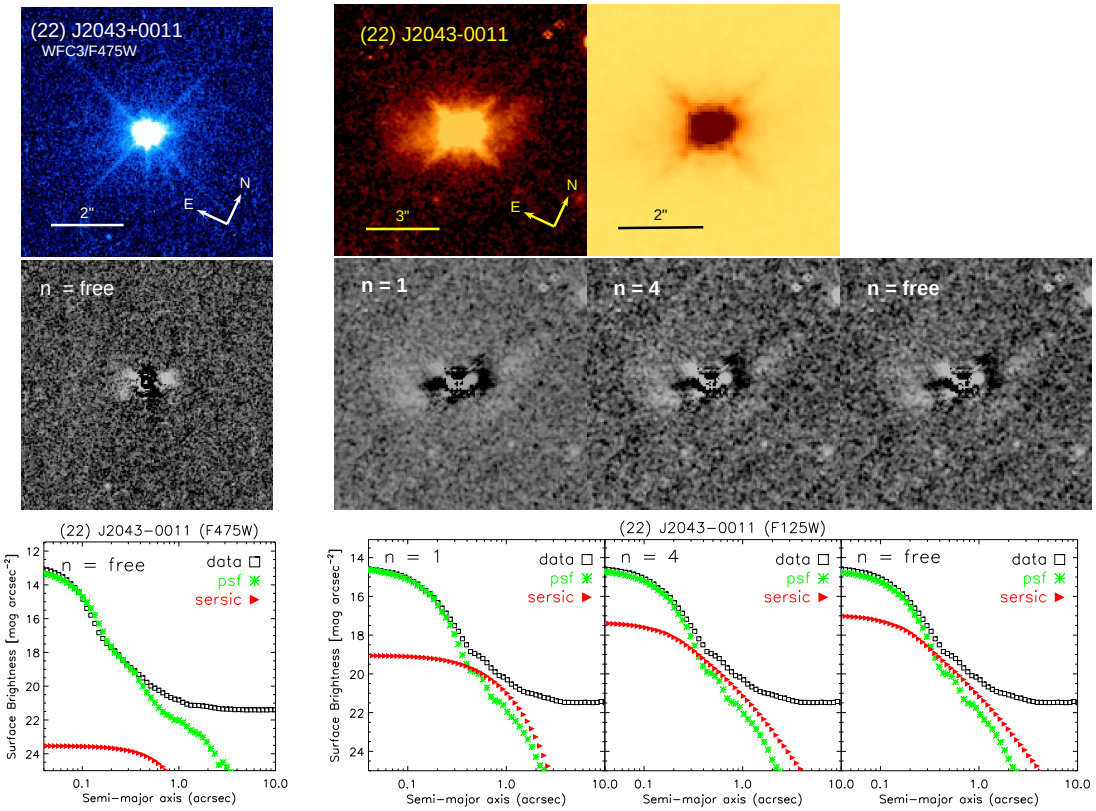

Figure 3.23: HST/WFC3 F475W (in blue, top left) and F125W (in red, top right) images of SDSS J2043+0011. In gray on the second row we show the residual image after subtracting the best fit GAFIT model. The particular model is indicated at the right top corner of the residual image: n = 1 is an exponential disk, n = 4 is a de Vaucouleur profile, and n = free indicates unconstrained Sersic index. On the third row we show radial surface brightness profiles of each component in the particular model, indicated again in the right top corner of each plot.

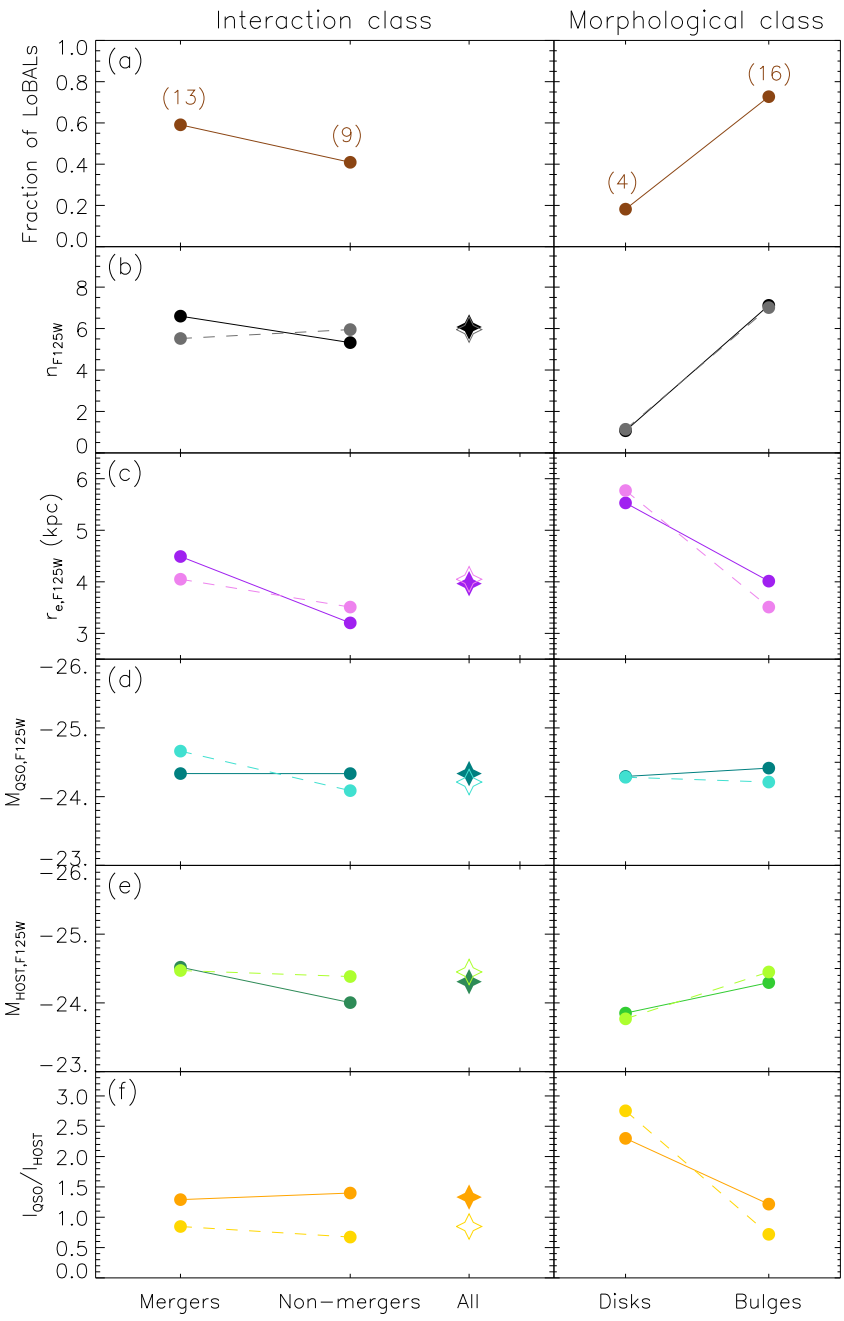

Figure 3.24: Average (darker circles, connected with solid line) and median (paler circles, connected with dashed line) quantities from the morphological study of this sample of LoBALs, divided into subsamples by interactions class (left column) and morphological class (right columns). With a star, we show the average (solid) and median (open) value for the entire sample of LoBALs. For definitions of the classes, see Sections 3.4.2 and 3.4.1. (a) Fraction of LoBALs in each class. (b) Sersic index of the best-fitting GALFIT model. (c) Half-light radius (in kpc) of the surface brightness profile. (d) Absolute magnitude of the PSF in the WFC3/IR F125W channel corrected for Galactic extinctions. (e) Absolute magnitude of the host galaxy in the WFC3/IR F125W channel corrected for Galactic extinction. (f) PSF to host component intensity ratio.

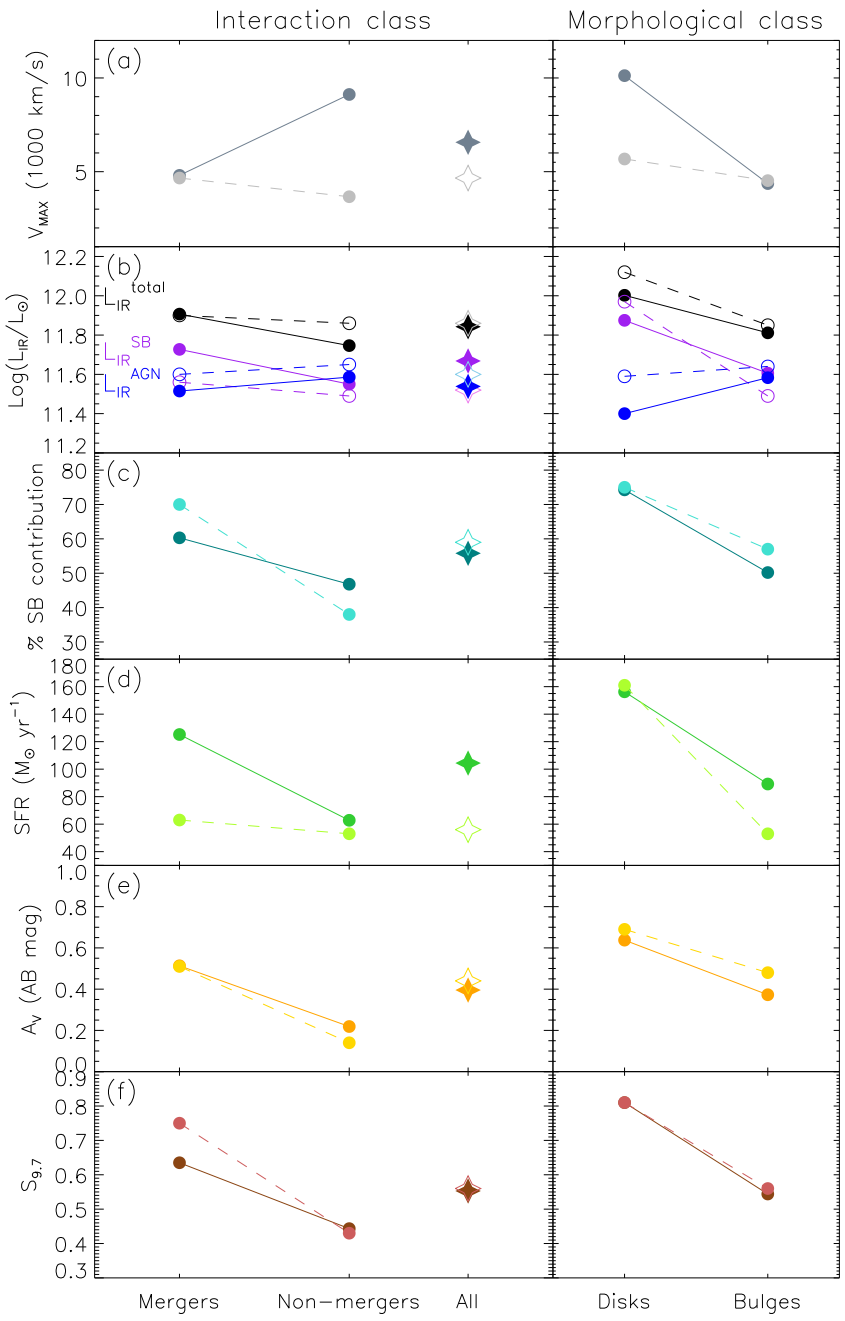

Figure 3.25: Average (darker circles, connected with solid line) and median (paler circles, connected with dashed line) quantities from the infrared SED study of this sample of LoBALs, divided into subsamples by interactions class (left column) and morphological class (right columns). With a star we show the average (solid) and median (open) value for the entire sample of LoBALs. For definitions of the classes, see Sections 3.4.2 and 3.4.1. (a) Maximum velocity of the Mg II 2800Å broad absorption line from Trump et al. (2006). (b) Total, starburst, and AGN infrared luminosities from the SED fitting. (c) Percentage starburst contribution to the total infrared luminosity. (d) Star formation rates from the SED fitting. (e) Absolute extinction in V, assuming SMC extinction law for the QSO + host system. (f) Silicate 9.7μm emission strength.

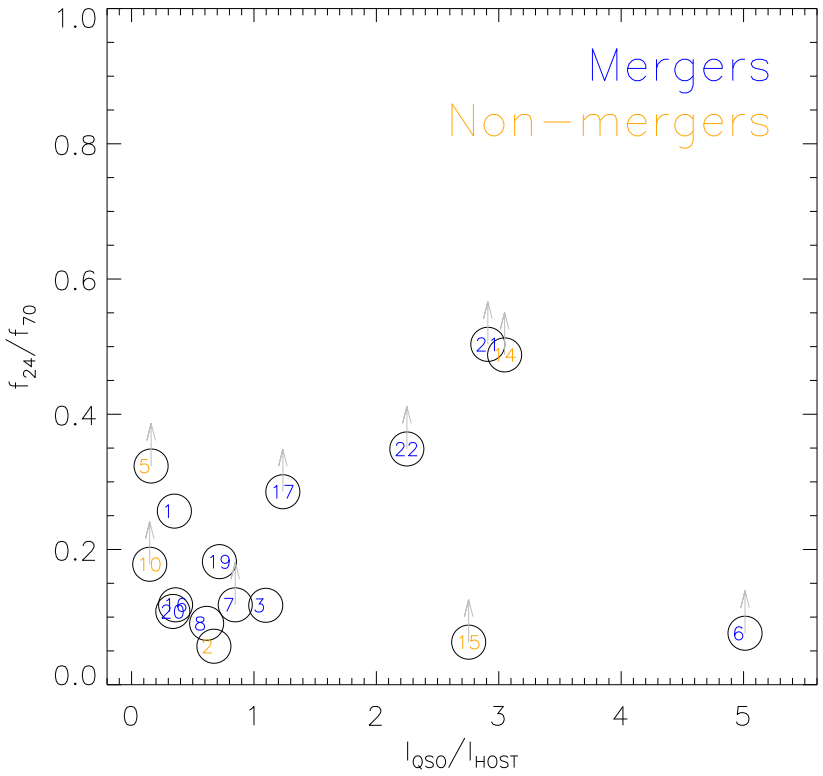

Figure 3.26: MIPS 24 to 70 μm colors as a function of the PSF to host intensity ratio. The object number is inscribed inside the plotting symbol, color coded according to interaction class (see legend). Gray arrows indicate upper limits on the far-infrared MIPS photometry. Seven objects front he sample do not have available FIR MIPS photometry.

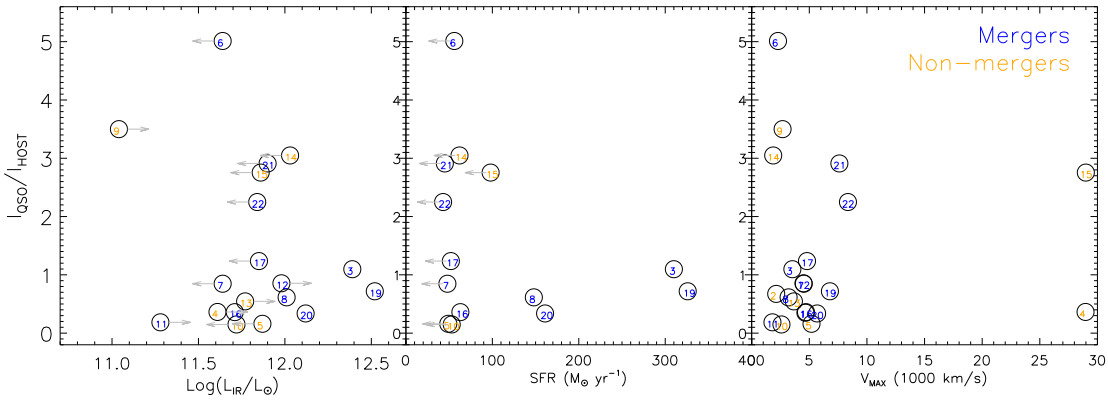

Figure 3.27: WFC3/IR F125W PSF to host component intensity ratio as a function of total infrared luminosity (left panel), star formation rate (middle panel), and maximum outflow velocity (right panel). The object number is inscribed inside the plotting symbol, color coded according to interaction class (see legend). Gray arrows indicate upper limits on the far-infrared MIPS photometry.

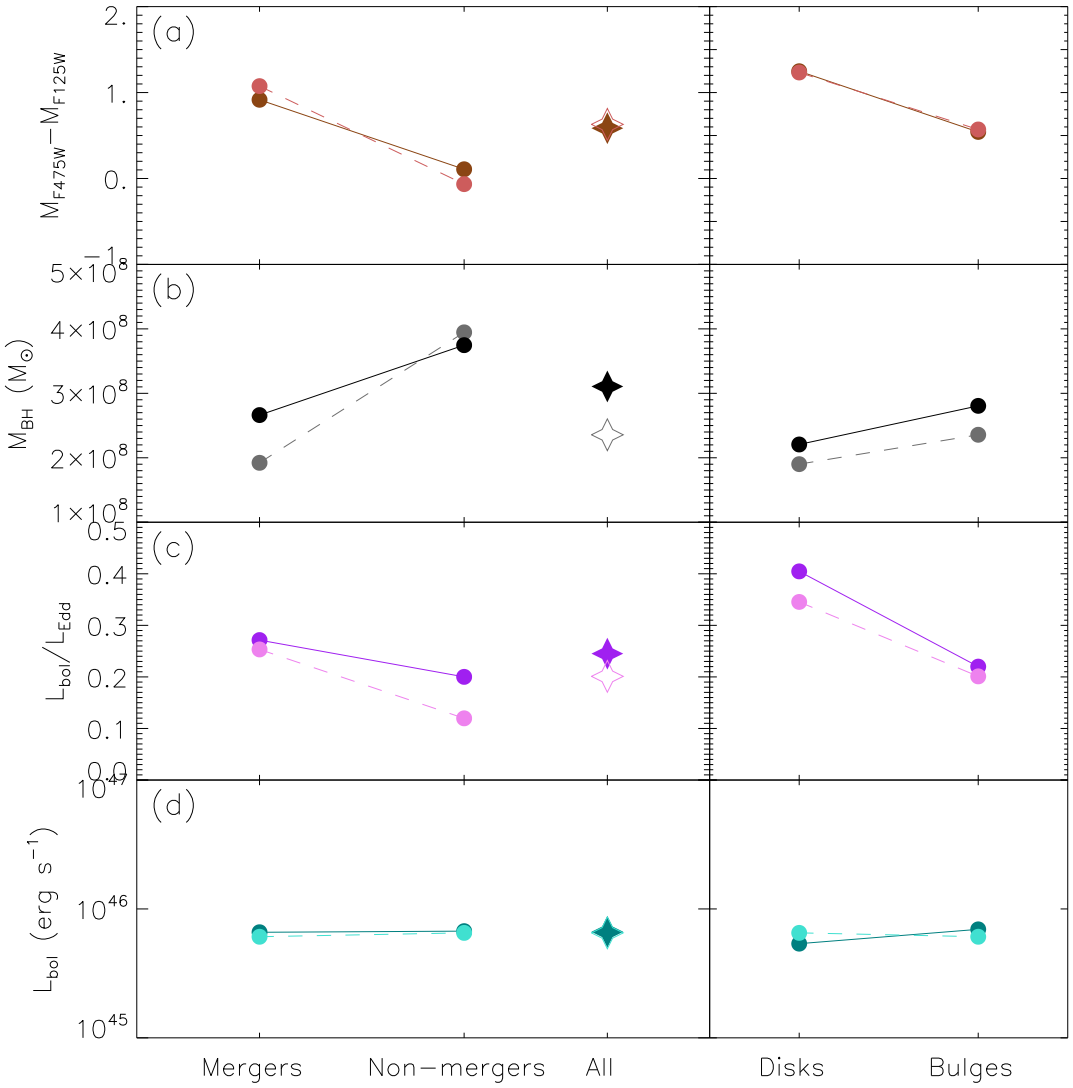

Figure 3.28: Average (darker circles, connected with solid line) and median (paler circles, connected with dashed line) quantities divided into subsamples by interactions class (left column) and morphological class (right columns). With a star we show the average (solid) and median (open) value for the entire sample of LoBALs. (a) F475W - F125W colors. (b) Black hole masses estimated with the single epoch virial black hole mass relation by citedPark2012 using the SDSS spectra of the LoBALs. (c) Eddington ratio. (d) QSO bolometric luminosity integrated from the optical through FIR SEDs.

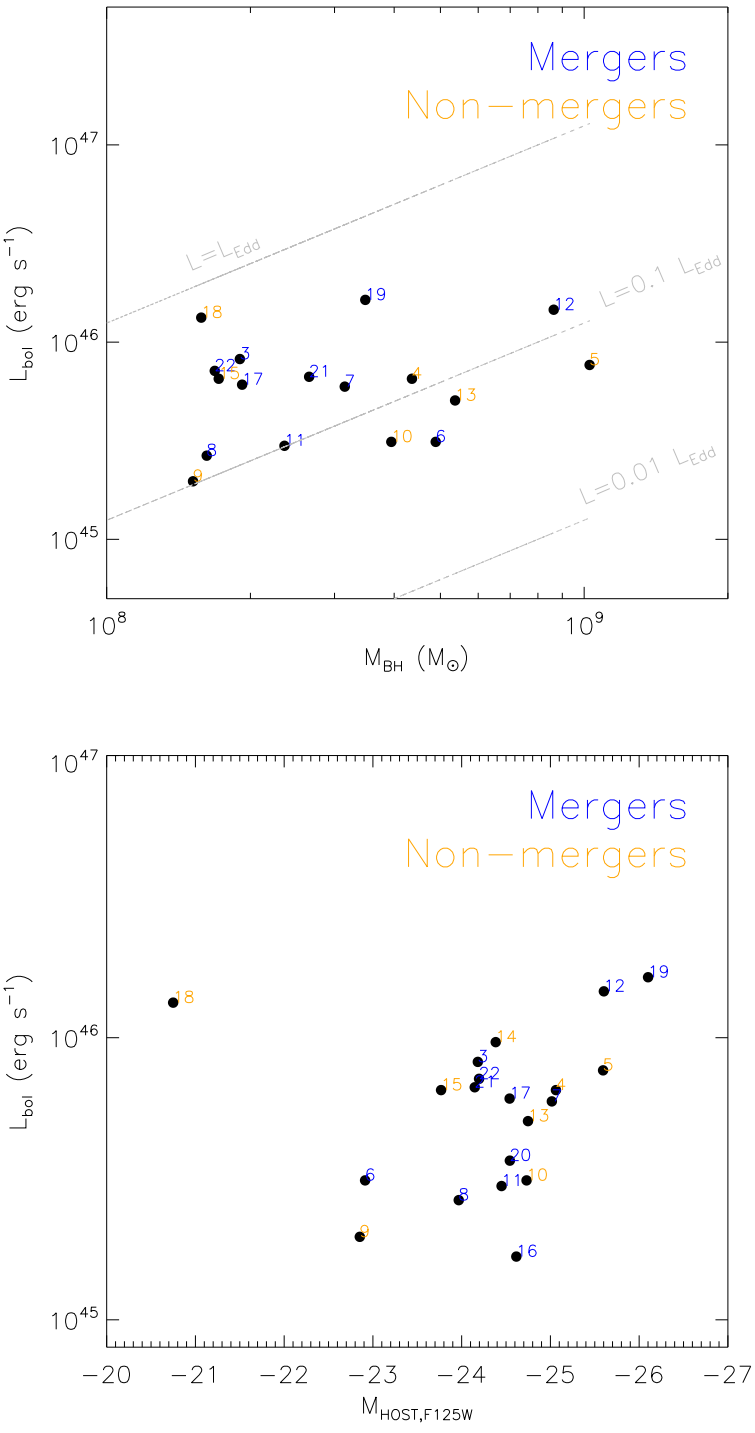

Figure 3.29: Top: Bolometric AGN luminosity integrated from the optical through FIR SEDs vs. black hole mass estimated from the FWHM of H_β and the 5100Å luminosity. Bottom: Bolometric AGN luminosity vs. the host absolute magnitude in WFC3 IR/F125W.

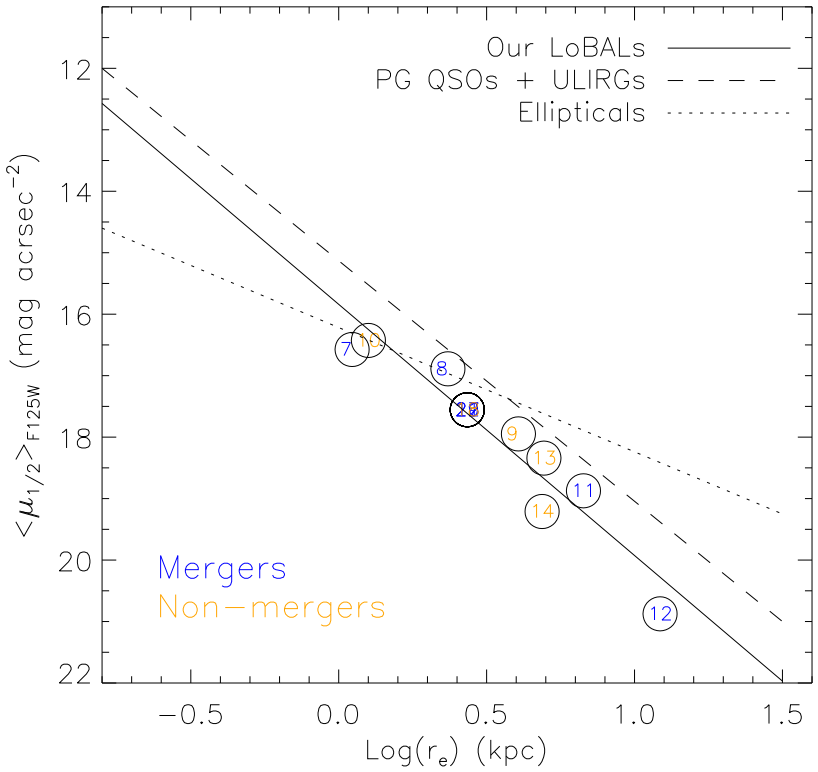

Figure 3.30: The Kormendy relation for LoBALs (solid line): average surface brightness at the effective radius (r_e) vs. r_e. The magnitudes are corrected for Galactic and host extinction, but are not k-corrected. The solid line is a linear fit to the data for this sample of LoBALs. The dashed line is the relationship found for the QUEST sample of $z < 0.3$ late-stage gas-rich mergers of PG QSOs and ULIRGs (H-band: Veilleux et al., 2006). The dotted line is for a larger sample of nearby elliptical galaxies from Pahre (1999) (K-band).

Chapter 4

Conclusion

The goal of this study is to establish the relationship between LoBAL QSOs, systems characterized by outflows of low-ionization gas at thousands of km s^{-1}, and the general population of unobscured type-1 QSOs. The SEDs and morphologies presented here attempts to answer the question of whether or not we see observational evidence suggesting that LoBALs are young QSOs caught in a short transition from merger-induced dust-enshrouded QSO towards unobscured optically-luminous QSOs. This link has been suggested by anecdotal observations of few LoBALs at $z < 0.4$ (Canalizo & Stockton, 2002) and further supported by finding anomalously larger fractions of LoBALs in radio and infrared selected samples of heavily dust-reddened type-1 QSOs (Urrutia et al., 2009; Glikman et al., 2012)

While the *Spitzer* observations suggest that LoBALs are very similar to non-LoBALs in terms of their mid-infrared spectral properties and far-infrared luminosities, which may in principle be consistent with the orientation model, the results from the *HST*

imaging give strong support for the evolutionary model. The two-dimensional GALFIT analysis of their host galaxies indicates that the majority of LoBALs represent early-type (i.e., bulge) morphology and about 60% show signs of tidal interaction, such as interacting companions, extended tidal tails, plumes, debris, significant residuals, and asymmetries. The morphologically disturbed systems represent various stages of the merger process: from two separate nuclei to relaxed bulges with extremely low surface brightness tidal tails.

The LoBALs in this sample are preferentially found in mergers, but the correct interpretation of this result requires that we investigate the properties of a well-matched sample of non-BAL unobscured QSOs of comparable luminosity in the same redshift range. Such a study is planned as a necessary extension of this work, but for now, the LoBAL morphologies can be interpreted in comparison to existing studies of low-redshift QSO hosts. It should be noted that some of those samples may possibly contain 1-4% LoBALs because the broad Mg II λ2800 absorption line can be detected only via UV spectroscopy for $z < 0.5$.

A compelling case can be made that LoBALs represent a stage of QSO evolution preceding the unobscured QSO phase. While we find at least 60% of the LoBALs to show signs of interaction, samples of RQ QSO hosts show at most 30% of the objects to be interacting, even though in most cases those observations were much deeper than ours. Previous studies of the morphologies of QSOs at low redshifts find that their host galaxies are mostly quiescent ellipticals with little or no signs of tidal interaction (Disney et al., 1995; Bahcall et al., 1997; Hamilton et al., 2002; Dunlop et al., 2003; Floyd et al., 2004). Those studies argue against the evolutionary model for QSOs. However, any study of QSO hosts

is extremely challenging due to the high contrast between nuclear and host galaxy light. Many of these observations do not reach considerable depth to recover faint relics of past tidal interaction. Deep observations (2 orbits with HST) by Floyd et al. (2004) of luminous QSOs at $z \sim 0.4$ find evidence for interaction in only one RQ QSO, with 70% of their sample being dominated by elliptical hosts with central black holes accreting at much higher rates than our LoBALs (RQ: $L/L_{Edd} = 0.3$-1; one object at 0.05). Guyon et al. (2006) studied a sample of PG QSOs at $z < 0.3$ and found mostly disks systems with signs of interaction in only 30% of the hosts (ellipticals: 36%; disks: 39%; undetermined: 25%). The 13 RQ QSOs in the Dunlop et al. (2003) sample of luminous QSOs at $z \sim 0.2$ were claimed to be dominated by undisturbed ellipticals (11/13) similar to the massive ellipticals in bright cluster galaxies. A major insight into the host galaxies of QSOs was the discovery of very faint shells in deep HST observations (5 orbits) of five of those QSOs previously classified by Dunlop et al. (2003) as featureless ellipticals (Canalizo et al., 2007; Bennert et al., 2008). This highlights the necessity of long exposures to detect the low surface brightness features possibly present in all elliptical QSO hosts.

Hence, the dominance of disturbed morphologies in LoBALs provides strong support for the idea that LoBALs are young QSOs. This is especially true if we consider a simple model for the co-evolution of galaxies and QSOs at low redshift assuming that black hole activity is only fueled by major mergers which result in the formation of elliptical galaxies (e.g., Kauffmann & Haehnelt, 2000). This model may seem an oversimplification of reality but merits attention at least at the highest AGN luminosities. In this framework of elliptical formation, finding that more than 70% of the LoBAL hosts are bulge-dominated

systems may provide further supports for the fueling of the QSO activity in LoBALs via mergers. On the other hand, since we find LoBALs to reside in galaxies at various stages of interaction (and non-interactions, at least at the limit of the current study) and since only modest amount of gas supply $\sim$ 1 $M_{\odot}$ yr^{-1} is sufficient to fuel AGN accretion, it is possible that some other mechanism (e.g., minor mergers or companion interaction) is responsible for the fueling of the QSO activity at least in some QSOs. In fact, all but one of the bulge-dominated LoBALs that show no tidal disturbance have potential companion sources within 80 kpc projected distance.

Our results are consistent with LoBALs being a key link between mergers and QSOs representing the later phase of the blowout phase when the central QSO has already cleared the gas and dust enshrouding it and quenched star formation on galaxy scales. Finally, we note that these LoBALs were drawn from a sample of optically selected QSOs. It is possible that the optically selected LoBALs represent the very last stage of the blowout phase. More dust-obscured LoBALs may represent the early outflow stages, however, those would normally be missed in optical-selections because their luminosities would not classify them as QSOs.

Bibliography

Abazajian, K., et al. 2005, AJ, 129, 1755

Allain, T., Leach, S., & Sedlmayr, E. 1996, A&A, 305, 602

Allen, J. T., Hewett, P. C., Maddox, N., Richards, G. T., & Belokurov, V. 2011, MNRAS, 410, 860

Antonucci, R. 1993, ARA&A, 31, 473

Armus, L., Heckman, T., & Miley, G. 1987, AJ, 94, 831

Bahcall, J. N., Kirhakos, S., Saxe, D. H., & Schneider, D. P. 1997, ApJ, 479, 642

Bautista, M. A., Dunn, J. P., Arav, N., Korista, K. T., Moe, M., & Benn, C. 2010, ApJ, 713, 25

Becker, R. H., Gregg, M. D., Hook, I. M., McMahon, R. G., White, R. L., & Helfand, D. J. 1997, ApJ, 479, L93+

Becker, R. H., White, R. L., Gregg, M. D., Brotherton, M. S., Laurent-Muehleisen, S. A., & Arav, N. 2000, ApJ, 538, 72

Becker, R. H., et al. 2001, ApJS, 135, 227

Bennert, N., Canalizo, G., Jungwiert, B., Stockton, A., Schweizer, F., Peng, C. Y., & Lacy, M. 2008, ApJ, 677, 846

Boroson, T. A., & Green, R. F. 1992, ApJS, 80, 109

Bouchet, P., Lequeux, J., Maurice, E., Prevot, L., & Prevot-Burnichon, M. L. 1985, A&A, 149, 330

Bouwman, J., Meeus, G., de Koter, A., Hony, S., Dominik, C., & Waters, L. B. F. M. 2001, A&A, 375, 950

Brotherton, M. S., De Breuck, C., & Schaefer, J. J. 2006, Monthly Notices of the Royal Astronomical Society: Letters, 372, L58

Brotherton, M. S., van Breugel, W., Smith, R. J., Boyle, B. J., Shanks, T., Croom, S. M., Miller, L., & Becker, R. H. 1998, ApJ, 505, L7+

Canalizo, G., Bennert, N., Jungwiert, B., Stockton, A., Schweizer, F., Lacy, M., & Peng, C. 2007, ApJ, 669, 801

Canalizo, G., & Stockton, A. 2001, ApJ, 555, 719

Canalizo, G., & Stockton, A. 2002, in Astronomical Society of the Pacific Conference Series, Vol. 255, Mass Outflow in Active Galactic Nuclei: New Perspectives, ed. D. M. Crenshaw, S. B. Kraemer, & I. M. George, 195–+

Chung, A., Yun, M. S., Naraynan, G., Heyer, M., & Erickson, N. R. 2011, ApJ, 732, L15+

Clavel, J., et al. 2000, A&A, 357, 839

Cleary, K., Lawrence, C. R., Marshall, J. A., Hao, L., & Meier, D. 2007, ApJ, 660, 117

Cutri, R. M., Rieke, G. H., Tokunaga, A. T., Willner, S. P., & Rudy, R. J. 1984, ApJ, 280, 521

Cutri, R. M., et al. 2003, VizieR Online Data Catalog, 2246, 0

Dai, X., Shankar, F., & Sivakoff, G. R. 2010, ArXiv e-prints

Dale, D. A., & Helou, G. 2002, ApJ, 576, 159

Dasyra, K. M., et al. 2006, ApJ, 651, 835

Debuhr, J., Quataert, E., & Ma, C.-P. 2011, MNRAS, 412, 1341

Devereux, N. A., & Eales, S. A. 1989, ApJ, 340, 708

Devereux, N. A., & Hameed, S. 1997, AJ, 113, 599

Devereux, N. A., & Young, J. S. 1990, ApJ, 350, L25

Di Matteo, T., Springel, V., & Hernquist, L. 2005, Nature, 433, 604

DiPompeo, M. A., Brotherton, M. S., Becker, R. H., Tran, H. D., Gregg, M. D., White, R. L., & Laurent-Muehleisen, S. A. 2010, ApJS, 189, 83

DiPompeo, M. A., Brotherton, M. S., & De Breuck, C. 2012, ApJ, 752, 6

Disney, M. J., et al. 1995, Nature, 376, 150

Duley, W. W., Williams, D. A., & Moorhouse, A. 1991, MNRAS, 253, 505

Dunlop, J. S., McLure, R. J., Kukula, M. J., Baum, S. A., O'Dea, C. P., & Hughes, D. H. 2003, Monthly Notices of the Royal Astronomical Society, 340, 1095

Dunn, J. P., et al. 2010, ApJ, 709, 611

E. Le Floc'h, I. F. Mirabel, O. Laurent, V. Charmandaris, P. Gallais, M. Sauvage, L. Vigroux, & C. Cesarsky. 2001, A&A, 367, 487

Elvis, M. 2000, ApJ, 545, 63

Evans, A. S., Solomon, P. M., Tacconi, L. J., Vavilkin, T., & Downes, D. 2006, AJ, 132, 2398

Fabian, A. C. 2012, ArXiv e-prints

Farrah, D., Lacy, M., Priddey, R., Borys, C., & Afonso, J. 2007, ApJ, 662, L59

Farrah, D., Surace, J. A., Veilleux, S., Sanders, D. B., & Vacca, W. D. 2005, ApJ, 626, 70

Farrah, D., et al. 2010, ApJ, 717, 868

Feigelson, E. D., & Nelson, P. I. 1985, ApJ, 293, 192

Ferrarese, L., & Merritt, D. 2000, The Astrophysical Journal Letters, 539, L9

Fisher, D. B., & Drory, N. 2008, in Astronomical Society of the Pacific Conference Series, Vol. 396, Formation and Evolution of Galaxy Disks, ed. J. G. Funes & E. M. Corsini, 309

Floyd, D. J. E., Kukula, M. J., Dunlop, J. S., McLure, R. J., Miller, L., Percival, W. J., Baum, S. A., & O'Dea, C. P. 2004, Monthly Notices of the Royal Astronomical Society, 355, 196

Foltz, C., Wilkes, B., Weymann, R., & Turnshek, D. 1983, PASP, 95, 341

Frayer, D. T., et al. 2006, AJ, 131, 250

Fukugita, M., Ichikawa, T., Gunn, J. E., Doi, M., Shimasaku, K., & Schneider, D. P. 1996, AJ, 111, 1748

Gallagher, S. C., Everett, J. E., Keating, S. K., Hill, A. R., & Deo, R. P. 2012, ArXiv e-prints

Gallagher, S. C., Hines, D. C., Blaylock, M., Priddey, R. S., Brandt, W. N., & Egami, E. E. 2007, ApJ, 665, 157

Gebhardt, K., et al. 2000, ApJ, 539, L13

Genzel, R., et al. 1998, ApJ, 498, 579

Gibson, R. R., et al. 2009, ApJ, 692, 758

Gillett, F. C., Forrest, W. J., & Merrill, K. M. 1973, ApJ, 183, 87

Glikman, E., et al. 2012, ArXiv e-prints

Gregg, M. D., Becker, R. H., Brotherton, M. S., Laurent-Muehleisen, S. A., Lacy, M., & White, R. L. 2000, ApJ, 544, 142

Guyon, O., Sanders, D. B., & Stockton, A. 2006, ApJS, 166, 89

Haas, M., Klaas, U., & Bianchi, S. 2002, A&A, 385, L23

Haas, M., Siebenmorgen, R., Schulz, B., Krügel, E., & Chini, R. 2005, A&A, 442, L39

Haas, M., et al. 2003, A&A, 402, 87

Hall, P. B. 2007, AJ, 133, 1271

Hall, P. B., et al. 2002, ApJS, 141, 267

Hamilton, T. S., Casertano, S., & Turnshek, D. A. 2002, ApJ, 576, 61

Hao, C. N., Xia, X. Y., Mao, S., Wu, H., & Deng, Z. G. 2005a, ApJ, 625, 78

Hao, L., Weedman, D. W., Spoon, H. W. W., Marshall, J. A., Levenson, N. A., Elitzur, M., & Houck, J. R. 2007, ApJ, 655, L77

Hao, L., et al. 2005b, ApJ, 625, L75

Hazard, C., McMahon, R. G., Webb, J. K., & Morton, D. C. 1987, ApJ, 323, 263

Hazard, C., Morton, D. C., Terlevich, R., & McMahon, R. 1984, ApJ, 282, 33

Hewett, P. C., & Foltz, C. B. 2003, AJ, 125, 1784

Hibbard, J. E., & Yun, M. S. 1999, AJ, 118, 162

Hiner, K. D., Canalizo, G., Lacy, M., Sajina, A., Armus, L., Ridgway, S., & Storrie-Lombardi, L. 2009, ApJ, 706, 508

Hopkins, P. F., Bundy, K., Hernquist, L., & Ellis, R. S. 2007, ApJ, 659, 976

Hopkins, P. F., Cox, T. J., Kereš, D., & Hernquist, L. 2008a, ApJS, 175, 390

Hopkins, P. F., Hernquist, L., Cox, T. J., & Kereš, D. 2008b, ApJS, 175, 356

Hopkins, P. F., Hernquist, L., Cox, T. J., Matteo, T. D., Robertson, B., & Springel, V. 2006, The Astrophysical Journal Supplement Series, 163, 1

Houck, J. R., et al. 2004, ApJS, 154, 18

Hunt, L. K., Thuan, T. X., Izotov, Y. I., & Sauvage, M. 2010, ApJ, 712, 164

Ji, T., Wang, T.-G., Zhou, H.-Y., & Wang, H.-Y. 2012, Research in Astronomy and Astrophysics, 12, 369

Kauffmann, G., & Haehnelt, M. 2000, MNRAS, 311, 576

Kemper, F., Vriend, W. J., & Tielens, A. G. G. M. 2004, ApJ, 609, 826

Kennicutt, R. C. 1998, Annual Review of Astronomy and Astrophysics, 36, 189

Kewley, L. J., Geller, M. J., Jansen, R. A., & Dopita, M. A. 2002, AJ, 124, 3135

Knacke, R. F., & Thomson, R. K. 1973, PASP, 85, 341

Knapp, G. R., Gunn, J. E., & Wynn-Williams, C. G. 1992, ApJ, 399, 76

Kocevski, D. D., et al. 2012, ApJ, 744, 148

Kormendy, J., & Gebhardt, K. 2001, in American Institute of Physics Conference Series, Vol. 586, 20th Texas Symposium on relativistic astrophysics, ed. J. C. Wheeler & H. Martel, 363–381

Kormendy, J., & Richstone, D. 1995, ARA&A, 33, 581

Lacy, M., Sajina, A., Petric, A. O., Seymour, N., Canalizo, G., Ridgway, S. E., Armus, L., & Storrie-Lombardi, L. J. 2007, ApJ, 669, L61

Landt, H., Buchanan, C. L., & Barmby, P. 2010, Monthly Notices of the Royal Astronomical Society, 408, 1982

Laor, A. 1998, The Astrophysical Journal Letters, 505, L83

Laor, A., & Draine, B. T. 1993, ApJ, 402, 441

Laurent, O., Mirabel, I. F., Charmandaris, V., Gallais, P., Madden, S. C., Sauvage, M., Vigroux, L., & Cesarsky, C. 2000, A&A, 359, 887

Leger, A., & Puget, J. L. 1984, A&A, 137, L5

Lipari, S., Colina, L., & Macchetto, F. 1994, ApJ, 427, 174

Lonsdale, C. J., et al. 2003, PASP, 115, 897

Magorrian, J., et al. 1998, The Astronomical Journal, 115, 2285

Maiolino, R., Marconi, A., & Oliva, E. 2001, A&A, 365, 37

Makovoz, D., & Marleau, F. R. 2005, PASP, 117, 1113

Mann, R. G., et al. 2002, Monthly Notices of the Royal Astronomical Society, 332, 549

Mazzei, P., & de Zotti, G. 1994, ApJ, 426, 97

McLeod, K. K., & McLeod, B. A. 2001, ApJ, 546, 782

McLure, R. J., & Dunlop, J. S. 2002, MNRAS, 331, 795

Menou, K., et al. 2001, ApJ, 561, 645

Moe, M., Arav, N., Bautista, M. A., & Korista, K. T. 2009, ApJ, 706, 525

Montenegro-Montes, F. M., Mack, K.-H., Vigotti, M., Benn, C. R., Carballo, R., Gonzlez-Serrano, J. I., Holt, J., & Jimnez-Lujn, F. 2008, Monthly Notices of the Royal Astronomical Society, 388, 1853

Murphy, Jr., T. W., Armus, L., Matthews, K., Soifer, B. T., Mazzarella, J. M., Shupe, D. L., Strauss, M. A., & Neugebauer, G. 1996, AJ, 111, 1025

Murray, N., & Chiang, J. 1998, ApJ, 494, 125

Murray, N., Chiang, J., Grossman, S. A., & Voit, G. M. 1995, ApJ, 451, 498

Nenkova, M., Ivezić, Ž., & Elitzur, M. 2002, ApJ, 570, L9

Nenkova, M., Sirocky, M. M., Ivezić, Ž., & Elitzur, M. 2008a, ApJ, 685, 147

Nenkova, M., Sirocky, M. M., Nikutta, R., Ivezić, Ž., & Elitzur, M. 2008b, ApJ, 685, 160

Netzer, H., et al. 2007, ApJ, 666, 806

Nikutta, R., Elitzur, M., & Lacy, M. 2009, ApJ, 707, 1550

O'Dowd, M. J., et al. 2009, ApJ, 705, 885

Pahre, M. A. 1999, ApJS, 124, 127

Park, D., et al. 2012, ApJ, 747, 30

Peng, C. Y., Ho, L. C., Impey, C. D., & Rix, H.-W. 2002, AJ, 124, 266

—. 2010, AJ, 139, 2097

Pier, E. A., & Krolik, J. H. 1993, ApJ, 418, 673

Popescu, C. C., Misiriotis, A., Kylafis, N. D., Tuffs, R. J., & Fischera, J. 2000, A&A, 362, 138

Prevot, M. L., Lequeux, J., Prevot, L., Maurice, E., & Rocca-Volmerange, B. 1984, A&A, 132, 389

Proga, D., Stone, J. M., & Kallman, T. R. 2000, ApJ, 543, 686

Puget, J. L., & Leger, A. 1989, ARA&A, 27, 161

Reichard, T. A., et al. 2003a, AJ, 125, 1711

—. 2003b, AJ, 126, 2594

Richards, G. T., Vanden Berk, D. E., Reichard, T. A., Hall, P. B., Schneider, D. P., SubbaRao, M., Thakar, A. R., & York, D. G. 2002, AJ, 124, 1

Richards, G. T., et al. 2003, AJ, 126, 1131

—. 2006, ApJS, 166, 470

Rieke, G. H., Alonso-Herrero, A., Weiner, B. J., Pérez-González, P. G., Blaylock, M., Donley, J. L., & Marcillac, D. 2009, ApJ, 692, 556

Rieke, G. H., et al. 2004, ApJS, 154, 25

Roche, P. F., Aitken, D. K., Smith, C. H., & Ward, M. J. 1991, MNRAS, 248, 606

Roussel, H., Vigroux, L., Sauvage, M., Bosma, A., & Bonoli, C. 2000, in Astronomical Society of the Pacific Conference Series, Vol. 197, Dynamics of Galaxies: from the Early Universe to the Present, ed. F. Combes, G. A. Mamon, & V. Charmandaris, 71–+

Rowan-Robinson, M., & Crawford, J. 1989, MNRAS, 238, 523

Rupke, D. S. N., & Veilleux, S. 2011, ApJ, 729, L27+

Sajina, A., Scott, D., Dennefeld, M., Dole, H., Lacy, M., & Lagache, G. 2006, Monthly Notices of the Royal Astronomical Society, 369, 939

Sajina, A., et al. 2008, ApJ, 683, 659

Sanders, D. B., & Mirabel, I. F. 1996, ARA&A, 34, 749

Sanders, D. B., Soifer, B. T., Elias, J. H., Madore, B. F., Matthews, K., Neugebauer, G., & Scoville, N. Z. 1988, ApJ, 325, 74

Schawinski, K., Simmons, B. D., Urry, C. M., Treister, E., & Glikman, E. 2012, MNRAS, L488

Schlegel, D. J., Finkbeiner, D. P., & Davis, M. 1998, ApJ, 500, 525

Schneider, D. P., et al. 2005, AJ, 130, 367

—. 2010, AJ, 139, 2360

Schweitzer, M., et al. 2006, ApJ, 649, 79

—. 2008, ApJ, 679, 101

Shi, Y., et al. 2007, ApJ, 669, 841

Siebenmorgen, R., Haas, M., Krügel, E., & Schulz, B. 2005, A&A, 436, L5

Skrutskie, M. F., et al. 2006, AJ, 131, 1163

Smith, J. D. T., et al. 2007, ApJ, 656, 770

Spoon, H. W. W., Marshall, J. A., Houck, J. R., Elitzur, M., Hao, L., Armus, L., Brandl, B. R., & Charmandaris, V. 2007, ApJ, 654, L49

Sprayberry, D., & Foltz, C. B. 1992, ApJ, 390, 39

Stocke, J. T., Foltz, C. B., Weymann, R. J., & Christiansen, W. A. 1984, ApJ, 280, 476

Stocke, J. T., Morris, S. L., Weymann, R. J., & Foltz, C. B. 1992, ApJ, 396, 487

Sturm, E., et al. 2005, ApJ, 629, L21

—. 2011, ApJ, 733, L16+

Teplitz, H. I., et al. 2006, ApJ, 638, L1

Tolea, A., Krolik, J. H., & Tsvetanov, Z. 2002, ApJ, 578, L31

Toomre, A., & Toomre, J. 1972, ApJ, 178, 623

Tremaine, S., et al. 2002, ApJ, 574, 740

Tremonti, C. A., Moustakas, J., & Diamond-Stanic, A. M. 2007, ApJ, 663, L77

Trump, J. R., et al. 2006, ApJS, 165, 1

Urrutia, T., Becker, R. H., White, R. L., Glikman, E., Lacy, M., Hodge, J., & Gregg, M. D. 2009, The Astrophysical Journal, 698, 1095

Van Wassenhove, S., Volonteri, M., Mayer, L., Dotti, M., Bellovary, J., & Callegari, S. 2012, ApJ, 748, L7

Vanden Berk, D. E., et al. 2001, AJ, 122, 549

Veilleux, S., Kim, D.-C., & Sanders, D. B. 2002, ApJS, 143, 315

Veilleux, S., et al. 2006, ApJ, 643, 707

—. 2009, ApJ, 701, 587

Verstraete, L., Puget, J. L., Falgarone, E., Drapatz, S., Wright, C. M., & Timmermann, R. 1996, A&A, 315, L337

Voit, G. M. 1992, MNRAS, 258, 841

Voit, G. M., Weymann, R. J., & Korista, K. T. 1993, ApJ, 413, 95

Weedman, D. W., et al. 2005, ApJ, 633, 706

Weymann, R. J., Morris, S. L., Foltz, C. B., & Hewett, P. C. 1991, ApJ, 373, 23

Willott, C. J., Rawlings, S., & Grimes, J. A. 2003, ApJ, 598, 909

York, D. G., et al. 2000, AJ, 120, 1579

Zakamska, N. L., Gómez, L., Strauss, M. A., & Krolik, J. H. 2008, AJ, 136, 1607

Appendix A

APPENDIX: SDSS spectra of the 22 LoBALs

Figure A.1 shows the SDSS spectra of the 22 LoBALs in the sample and details on the Mg II line to assure the reader that the sample comprises of bona fide LoBALs. We adopt the more inclusive definition by Trump et al. (2006) requiring the troughs to span a velocity width of at least 1000 km s^{-1} blue-ward of Mg II λ2800. Eight of the 22 LoBALs here have blue-shifted Mg II absorption line widths between 1000 and 2000 km s^{-1}, which would classify them as mini-BALs according to the traditional definition by Weymann et al. (1991) requiring widths greater than 2000 km s^{-1}.

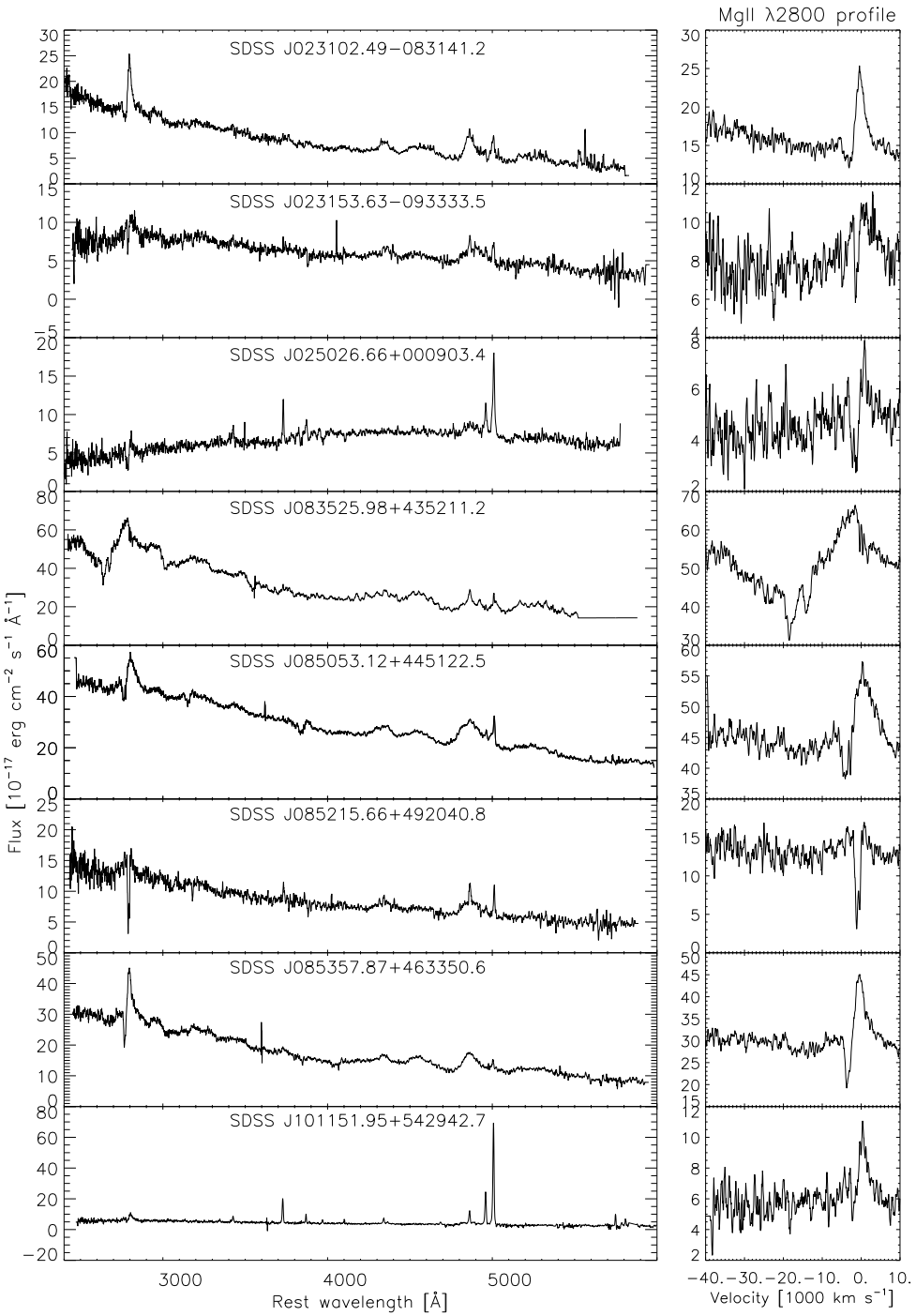

Figure A.1: Left: SDSS spectra of the 22 LoBALs. Right: Velocity profile of the Mg II λ2800 line.

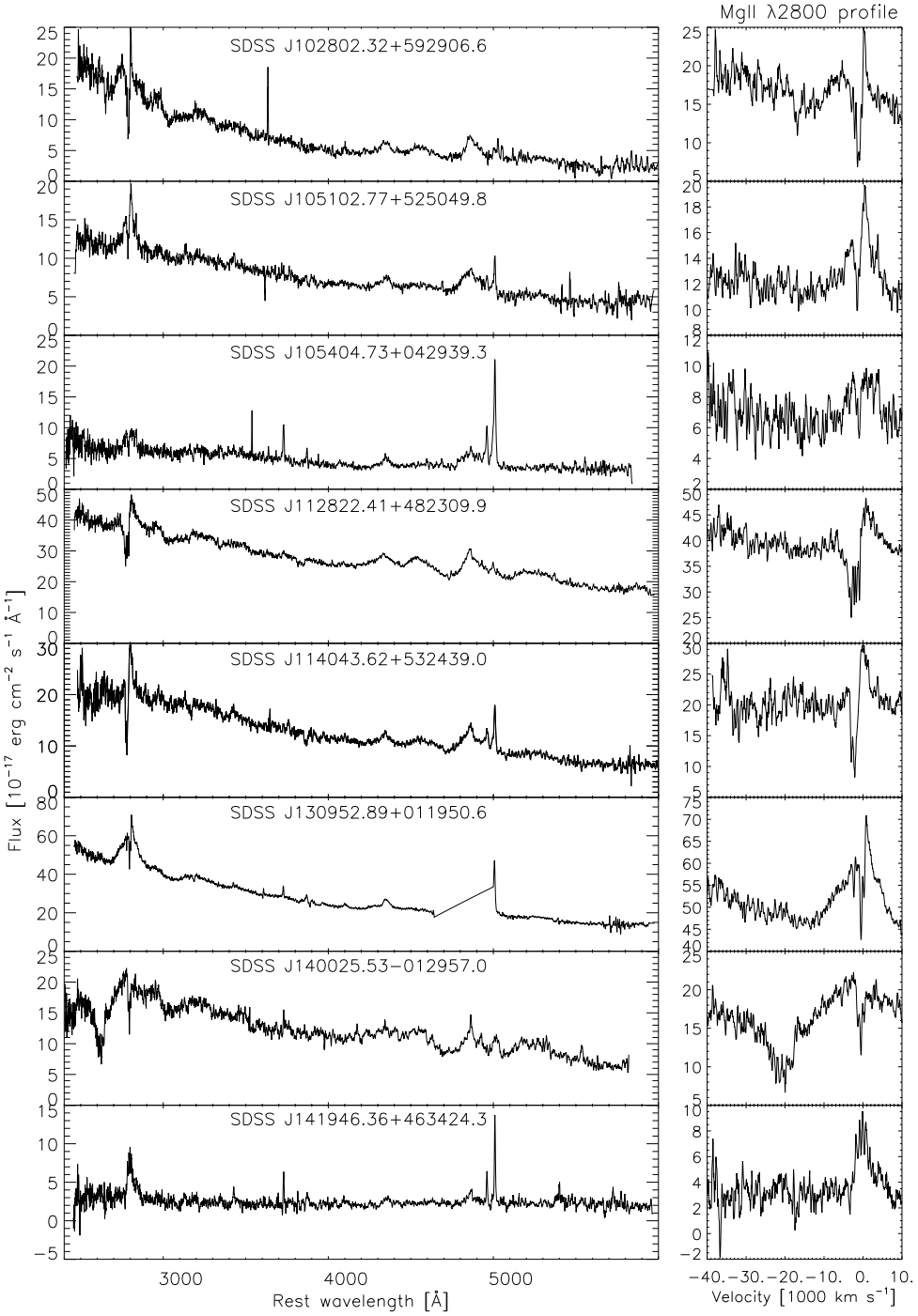

Figure A.1: Continued.

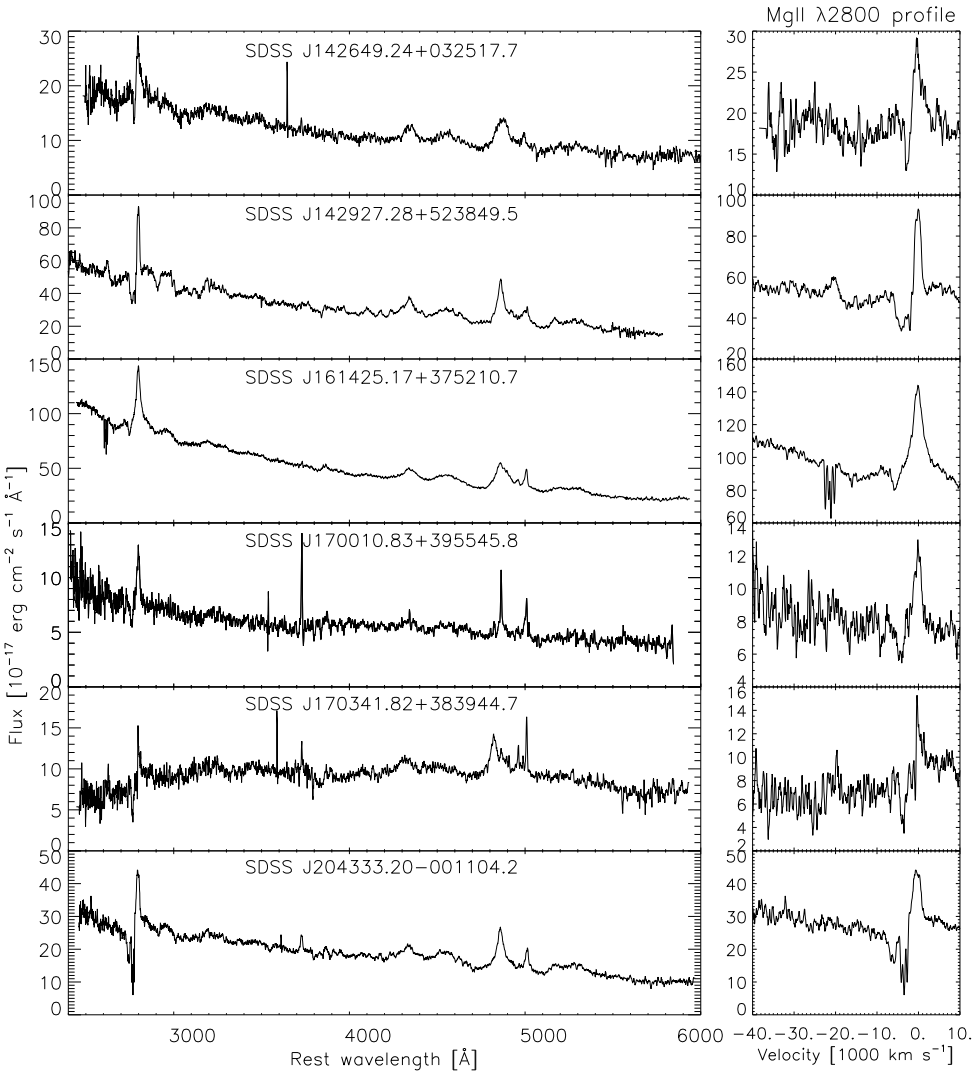

Figure A.1: Continued.